Quantitative Methods in Magnetization Transfer and Chemical Exchange Saturation Transfer at 7 T

By

Nicolas Geades

Thesis submitted to the University of Nottingham
for the degree of Doctor of Philosophy

July 2017

Contents

Abstract

Ultra-High field (7T) MRI provides high sensitivity which allows for new qualitative and quantitative methodologies to be developed, that provide clinically useful information. The work presented in this thesis is focussed on developing a quick and reliable quantitative MT and CEST methodology, taking account of the difficulties encountered at high field. The method developed here has been tested on various studies, in both healthy and diseased brain, in an effort to aid the understanding of myelination in the human brain.

The work in this thesis uses the quantitative measure of MT as a marker for myelination, and it shows strong correlations between MT-based myelination and functional connectivity, as well as very strong correlation between MT and NOE. These findings showcase the potential of NOE as a myelin marker as well, as long as the MT vs. NOE relationship remains the same in pathology. Myelination is investigated (via MT and NOE) in Multiple Sclerosis (MS) and Glioma, showing a strong coupling between the two exists even in pathology.

Amide Proton Transfer (APT) is also investigated in Glioma, showing similar trends to MT and NOE. High resolution anatomical images can provide valuable information on the extend of the pathology, but quantitative information of the NMR properties of tissue (like MT, NOE and APT) has the potential to detect earlier abnormalities, and give a quantitative measure of healing or degeneration caused by pathology.

Acknowledgements

I would like to take this opportunity to thank all the people who have helped me during my studies and made this a thoroughly enjoyable experience. First I would like to thank my excellent supervisors Penny Gowland and Olivier Mougin for their invaluable knowledge and guidance, and for often believing in my work more than I did! I would also like to thank the Marie Curie Actions, Lesley Martin and Penny Gowland again for organizing the ITN group, which provided a unique and truly excellent environment for research and collaboration at 7T.

Thank you to all the colleagues at the SPMIC and the Marie Curie ITN group for aiding my understanding of MR physics through various social and academic meetings here in Nottingham and around the globe. The list of people to thank is too long, but I have to give special thanks to a group of close friends in Nottingham including Carolina Fernandes, Elena Boto, Clementine Lesbats, Andy Hale, Olivier Mougin, Simon Shah, Ben Tendler and Ben Hunt for all the great memories we share together, from climbing trees to enjoying beers at the JA and of course the relaxing drives/rides to the countryside after work. I would also like to thank Dennis Klomp, Janie Wijnen, Matthew Restivo and Vitaly Khlebnikov for making sure I felt at home in Utrecht during the four months I spent there, and everyone else in the ITN group for the countless humorous adventures and meetings throughout Europe, Canada and Singapore.

Last, but not least, I would like to thank my family, friends and Isidora for always supporting me, being next to me throughout the journey and making

sure I didn't lose touch with the outside (real) world during stressful times. This would have been impossible without your support.

Introduction

Magnetic Resonance Imaging (MRI) is now a well-established diagnostic imaging tool because of its unrivalled ability to produce high contrast images of soft tissue like the brain, liver and kidneys. This allows the study of pathological tissue in great detail, without any ionizing radiation. Magnetic Resonance (MR) is a very versatile technique, offering a vast range of applications from high resolution anatomical imaging, spectroscopy, diffusion, functional and molecular imaging. Ultra-high field MRI (7T) offers increased signal-to-noise ratio (SNR) which makes imaging at a sub-millimetre scale possible within a reasonable amount of time, and it also provides new contrast mechanisms like Magnetization Transfer (MT) and Chemical Exchange Saturation Transfer (CEST) imaging. High field MRI has considerable advantages over 1.5T and 3T but it comes with drawbacks too, like size, cost and B_1 field inhomogeneity. The effects of B_1 inhomogeneity is one of the main issues this study is attempting to correct for.

MRI is a very powerful tool for creating high resolution and high contrast images of soft tissue but the information it gives is usually qualitative, in the form of hyper or hypo-intensity of the signal in a region compared to another similar region. Diagnosis is then subject to radiographer and radiologist skill and experience. The aim of quantitative imaging is to reduce any bias from the radiographer and acquisition phase, and to enable comparison of objective measures between different scans and even different subjects. The aim of this study is to use the high sensitivity available in high field MRI to study new contrast mechanisms and develop methods for quantitative imaging, specifically quantitative MT and CEST imaging.

The first chapter of this thesis provides a brief theoretical overview on the source of the Nuclear Magnetic Resonance (NMR) signal, describing the basic quantum theory and classical description underlying the NMR signal. Signal acquisition techniques, the Free Induction Decay (FID) experiment and echoes are introduced and discussed, together with mechanisms that provide contrast in the human brain - more specifically relaxation times. This first chapter also includes an introduction to imaging techniques and the advantages and challenges of imaging at high field.

Chapter 2 introduces z-spectroscopy and the effects of MT and CEST as new contrast mechanisms. The source of the signal is investigated and various quantification methods are discussed.

Chapter 3 focuses on the MT signal in z-spectroscopy and the macromolecules seen in NMR spectroscopy. The relationship between myelin and MT is explored and the MT lineshape is examined. A study of the brain macromolecules using 2D Chemical Shift Imaging (CSI) is also presented. Throughout this thesis, and in literature, MT is linked to macromolecules in the bound pool, so this chapter evaluates the spectral, relaxation and spatial properties of macromolecules in the brain. The macromolecules are studied at very short TE times, not possible in Single Voxel Spectroscopy, where the macromolecule signal compared to brain metabolites is higher.

Chapter 4 focuses on a novel fully-quantitative method for estimating proton pool concentrations in z-spectroscopy. The model, its advantages, limitations and the more general challenges of quantification at 7T are discussed. The fitting procedure as well as the robustness of the quantification process is then evaluated and validated via Monte-Carlo simulations and a repeatability study.

Chapter 5 shows various applications of the newly developed fully quantitative method in the diseased brain, like tracking myelination in Multiple Sclerosis (MS) lesions with MT and NOE, and APT CEST imaging in Glioma. Chapter 5 also shows applications of the methodology to the healthy brain, with a study showing the relationship between cortical myeloarchitecture and electrophysiological networks, and finally a comparison between the MT and NOE signal in a large cohort of healthy volunteers.

Chapter 1

NMR Signal and Imaging Principles

This chapter describes the basic principles of Nuclear Magnetic Resonance (NMR) found in literature[4,7,14]. The quantum theory and classical description underlying the NMR signal are introduced and signal acquisition based on Free Induction Decay (FID) and echoes are discussed. Relaxation processes are described as a source for contrast and a brief introduction is given in ways of imaging the human body using NMR, termed Magnetic Resonance Imaging (MRI). Finally the concept of field mapping is discussed.

1.1 Quantum theory and the classical description

NMR studies the interaction between the angular momentum (or spin) of a nucleus, which is a quantum property, and an externally applied magnetic field. In quantum theory, the spin of a nucleus can hold two discrete values, parallel or anti-parallel with the external magnetic field B_0 (or spin up and spin down), which helps understand the interaction between the nucleus and external magnetic field. When it comes to interaction with an applied magnetic field, B_1, the classical model is easier to understand as it allows for all orientations of the spin. This section will explain the quantum theory and classical description of the NMR effect.

1.1.1 Angular momentum, spin and nuclei

The concept of NMR describes the interaction between a nucleus and an external magnetic field. While an atom consists of a positively charged nucleus and negatively charged orbiting electrons, most of its mass comes from the nucleus. The nucleus consists of protons and neutrons, both having similar mass. All elementary particles (electrons, protons and neutrons) have various properties like mass, charge, angular momentum and intrinsic angular momentum, also known as spin. Both protons and neutrons possess intrinsic spin (termed the quantum number, $\mathbf{I}$) and this number can only take integer or half integer values. Spins within the same nucleus can cancel each other out, so only nuclei with an odd number of protons and/or neutrons have a net spin that is not zero. This net spin gives rise to an angular momentum $\mathbf{J}$ which points along the spin axis and is related to $\mathbf{I}$ by

$$\mathbf{J} = \hbar\sqrt{\mathbf{I}(\mathbf{I}+1)} \tag{1.1}$$

where $\hbar$ is Planck's constant divided by 2π. Many nuclei possess non-zero spin but the Hydrogen nucleus is most commonly used in NMR experiments because of its natural abundance and high sensitivity. Table 1.1 shows a list of nuclei with non-zero spin commonly used in NMR, their relative sensitivity, natural abundance and gyromagnetic ratio γ.

The gyromagnetic ratio, γ, is a nucleus-dependent constant that describes the frequency of the spins' precession at a given external magnetic field B_0. Since

Table 1.1: Commonly used atomic nuclei and their properties.

Nucleus	**Spin**	**Natural abundance (%)**	**Relative sensitivity**	**Gyromagnetic ratio, $\gamma/2\pi$ (MHz/T)**
^{1}H	1/2	99.98	1	42.58
^{13}C	1/2	1.11	0.016	10.71
^{19}F	1/2	100	0.83	40.05
^{23}Na	3/2	100	0.093	11.26
^{31}P	1/2	100	0.066	17.23

the spinning particle, in this case the proton, has an electric charge, a magnetic field is generated by the motion of the charge. This magnetic field, also known as the magnetic dipole moment, μ, is related to $\mathbf{J}$ by

$$\mu = \gamma \mathbf{J} \tag{1.2}$$

The behaviour of this magnetic dipole moment in a magnetic field is the basis of the NMR phenomenon. As mentioned before, hydrogen (or proton) NMR is most common due to, in part, its high sensitivity, and this high sensitivity is directly linked to the gyromagnetic ratio, γ. Magnetic moment, Boltzmann spin population factor and detection frequency all depend on γ and all contribute to SNR, so NMR sensitivity is proportional to γ.

1.1.2 Interaction with B_0

The magnetic dipole moment of the proton (nucleus in the case of the hydrogen atom) causes it to behave like a dipole bar magnet which in turn interacts with any external magnetic fields. In the quantum model the magnetic dipole moment can only have (2**I**+1) orientations corresponding to (2**I**+1) energy levels. In the case of proton NMR, where $\mathbf{I} = \frac{1}{2}$, these two orientations are parallel to the external magnetic field B_0 (low energy state) and anti-parallel to B_0 (high energy state).

When no external magnetization is present, each of the magnetic moments of nuclei in a sample (let's assume a drop of water) will point in different directions, producing a zero net magnetization. Once an external magnetic field is applied and the nuclei have time to settle to a thermal equilibrium, they will align either parallel or anti-parallel to the field. This effect is illustrated in Figure 1.1.

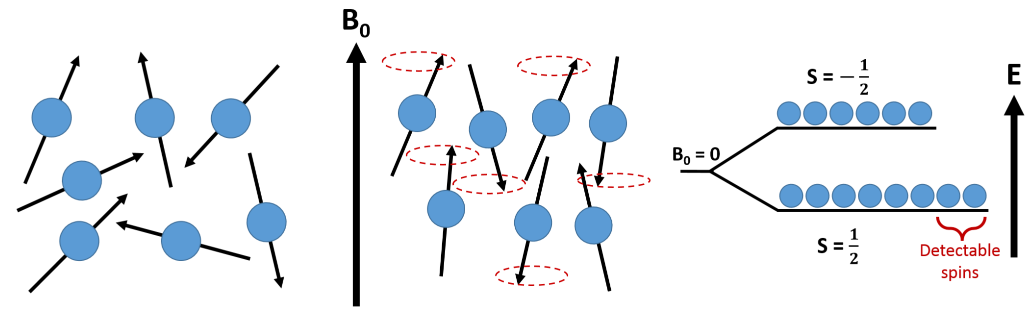

(a) No external magnetic field (b) In external magnetic field (c) Population difference

Figure 1.1: Net magnetizations of spins when (a) no external magnetic field is applied and (b) in thermal equilibrium in an externally applied magnetic field. (c) shows the population difference (greatly exaggerated) between the two spin states. Part (c) also shows that the NMR signal only comes from the small amount of detectable spins, as the rest of the spins cancel each other out.

Figure 1.1(c) shows a greatly exaggerated representation of the population difference between spins that align parallel to the external magnetic field (low energy state) and the spins that align anti-parallel to the external magnetic field (high energy state). The figure shows that only a very small portion of the total number of spins in a sample is actually detectable, as the two populations of parallel and anti-parallel spins are very similar and cancel each other out almost entirely.

This very small population difference is determined by the Boltzmann distribution:

$$\frac{N_\uparrow}{N_\downarrow} = \exp\left(\frac{\Delta E}{k_B T}\right) \tag{1.3}$$

where $N_\uparrow$ and $N_\downarrow$ are the number of spins aligned parallel and anti-parallel to the applied field, k_B is the Boltzmann constant, T is the temperature of the spin system and ΔE is the energy difference between the two spin up and spin down states. ΔE is proportional to the magnitude of the external magnetic field, B_0 and is defined as:

$$\Delta E = \gamma \hbar B_0 \tag{1.4}$$

Equation 1.3 relates to the sensitivity of NMR and shows that sensitivity increases with increasing magnitude of the external magnetic field. Equation 1.3 also shows that the population difference, and hence SNR, can also be increased by lowering the sample temperature, but this is not an option in-vivo.

The difference in the populations consists of only spin up nuclei that all precess about B_0 but are out of phase with each other. This produces a net magnetization, also known as equilibrium magnetization, M_0, which only has a longitudinal component and is defined as

$$M_0 = \frac{\gamma^2 \hbar^2 B_0 N}{4 k_B T} \tag{1.5}$$

where N is the total number of spins in the system.

The spins precess around B_0 at the Larmor frequency, ω, which depends on the gyromagnetic ratio, γ of the nucleus and B_0 field strength

$$\omega = -\gamma B_0 \tag{1.6}$$

Matching this frequency with an applied radio-frequency pulse triggers a transition between the spin up and spin down states, and also brings the precession of all individual spins to align in phase. This phenomenon can also be described with a classical approach where all orientations of the spin in a magnetic field are allowed, and is indeed more intuitive when describing the bulk magnetization.

The classical model helps us to understand the evolution of the magnetization, M, while it transitions between states, and how it can be manipulated. When a magnetic moment, M is placed in an external magnetic field, B, it experiences a torque, L defined as

$$L = M \times B = \frac{d\mathbf{J}}{dt} \tag{1.7}$$

and substituting equation 1.2 into equation 1.7 gives the Bloch equation

$$\frac{dM}{dt} = \gamma M \times B \tag{1.8}$$

This equation, like the Larmor equation, describes the precession of the magnetization, M around the external magnetic field, B at frequency ω. The Bloch equation can also be expanded to fully describe the time evolution of the magnetization by including longitudinal (T_1) and transverse (T_2) relaxation effects (see equation 1.10).

1.1.3 Interaction with B_1

Throughout this thesis, and throughout literature, it is assumed that the external magnetic field defines the z-axis of the Cartesian coordinate system. The net magnetization, M_0 therefore also lies along this z-axis, but because the individual spins making up M_0 are not in phase, M_0 has no transverse component. In order to detect NMR signal, the net magnetization needs to be rotated into the x-y plane where transverse magnetization can be detected.

This can be achieved by applying a time varying magnetic field, B_1, perpendicular to B_0 and matching the Larmor frequency, ω, of the precessing nuclei. This B_1 field is much smaller in amplitude than the external B_0 field, but if it matches the Larmor frequency of the spins it causes the magnetization to spiral down into the x-y plane. This spiralling motion is also called nutation and is shown in Figure 1.2a. To simplify the visualization of the NMR experiment, it is common to consider a reference frame rotating at the Larmor frequency about the z-axis. The new frame of reference is denoted (x', y', z') and is called the rotating frame (Figure 1.2b).

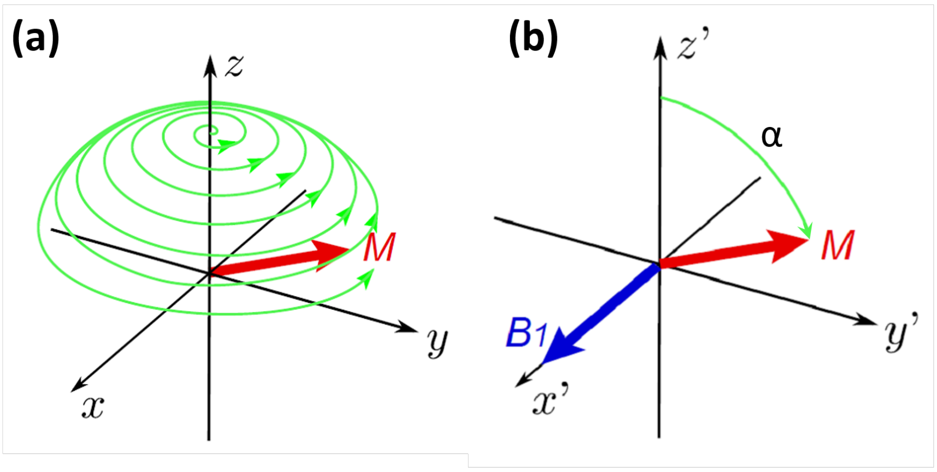

Figure 1.2: The evolution, or nutation of the net magnetization vector, M, when an RF pulse (B_1) is applied, in (a) the laboratory frame and (b) the rotating frame. The flip angle α in part (b) depends on the duration and amplitude of the B_1 pulse.

In the rotating frame, B_1 appears stationary and α gives the angle by which M_0 rotates around B_1, and depends on the amplitude and duration of the B_1 pulse. This is known as the flip angle and is defined as:

$$\alpha = \int_0^\tau \gamma B_1(t) dt \tag{1.9}$$

where τ is the duration of the pulse. Using this notation, a 90° pulse flips the vector M into the x'-y' plane, and a 180° pulse inverts M so that it is parallel to $-z'$.

1.2 Signal Acquisition

As discussed before, the signal in NMR comes from the detectable spins (see Figure 1.1c), and the larger the B_0 field strength, the greater the number of detectable spins and total signal that can be recorded. When a sample is placed into an external field, B_0, all the individual spins in the sample align with the direction of the field and reach thermal equilibrium. In this state the net magnetization cannot produce any detectable signal. The use of an RF pulse (B_1) forces the individual spins to precess in phase, depending on their physical location, tipping the magnetization into the transverse (x'-y') plane where the signal can be recorded.

1.2.1 Free Induction Decay (FID) and echoes

Once the RF pulse has been applied, the net magnetization precesses around the transverse plane, at the nucleus-specific Larmor frequency. After the RF pulse is turned off, a voltage is induced in a separate receive coil, by Faraday induction. The receive coil can detect signal in both the x and y directions, resulting in a signal that is a complex number, with real and imaginary parts.

When the RF pulse is turned off the spins are precessing in phase, but this phase is quickly lost because different groups of spins have slightly different frequencies, resulting in an exponential decay of the acquired signal. The rate of signal decay in the transverse plane, due to dephasing of the spins, is known as the T_2^* of the sample and gives information about the environment of the spins. The first part of Figure 1.3 shows a schematic of this phenomenon, including the RF pulse used to tip the magnetization in the transverse plane and the T_2^* envelope.

While no signal can be acquired once the spins in the x'-y' plane have completely dephased, the magnetization remains in the transverse plane for some time (governed by T_1 relaxation, explained in the next section) and isochromats can be refocussed with a 180° pulse to produce a spin echo. Figure 1.3 shows

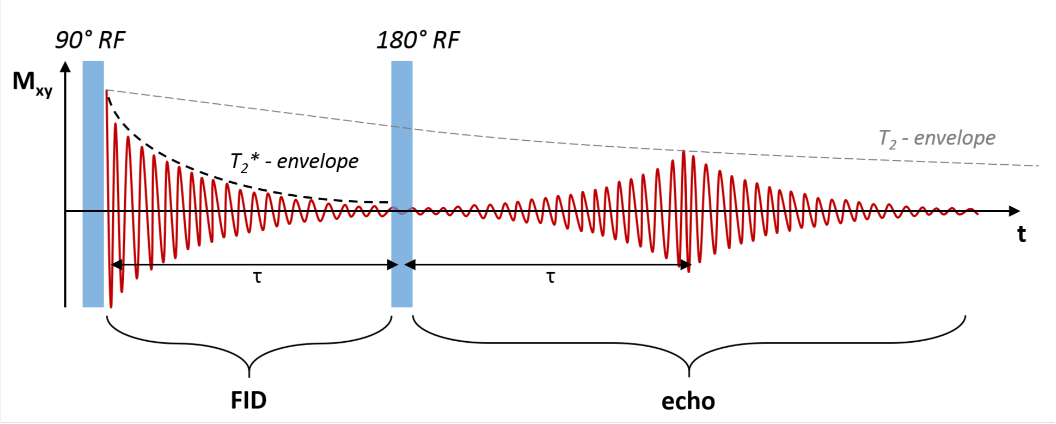

Figure 1.3: Schematic of Free Induction Decay (FID) and the formation of a spin echo.

how the use of a 180° pulse at time τ after the 90° pulse flips the spins around in the transverse plane so that the dephasing process is reversed, and an echo forms at time τ after the 180° pulse, or 2τ after the initial 90° pulse. This time is also called the echo time, or TE. The echo in Figure 1.3 is a SE as a refocussing pulse (180°) was used to form the echo. The amplitude of the echo is lower than the initial amplitude of the FID because not all spins can be refocused, resulting in another relaxation time envelope termed the T_2 time. Alternatively, if a gradient is applied while the spins are dephasing, accelerating the rate at which spins lose phase, a reversed gradient can be applied that will refocus the magnetization to form a gradient echo, which is attenuated by T_2^*. The different relaxation times (T_1 , T_2 and T_2^*) can be used to give contrast between different tissue types and are discussed in the next section of this chapter.

1.3 MRI contrast

So far this report has discussed the source of the signal in NMR, but not how this signal can be manipulated to give contrast in a sample. In traditional NMR, the Fourier transform of the FID or echo gives information on the molecules that the nuclei (protons) belong to, as well as information about the chemical environment of the protons. Because water is found in most human body tissue, and the chemical environment around the detectable proton is different in each tissue, the evolution of the spin is also different between tissues. This makes proton MRI a very powerful non-invasive tool in imaging human tissue, especially soft tissue high in water content, like the brain.

The amount of water, or detectable spins present in a sample defines the amount of signal that can be detected. The water content alone is then a contrast mechanism, termed proton density (PD), but requires a very long scan to remove any relaxation effects. The relaxation effects themselves are the most common contrast mechanisms in MRI, because they offer great flexibility in contrast adjustment and can be acquired much faster than PD scans.

In an NMR experiment, when the RF pulse is switched off the spins start to dephase due to local variations in magnetic field and slowly return to thermal equilibrium under the effect of the external static field B_0. This happens when the spins in the high energy state return to the low energy state, releasing the energy absorbed by the applied RF pulse. The energy released is exchanged between spins (spin-spin) and between spins and their surrounding tissue (spin-lattice). These relaxation mechanisms are respectively known as transverse (T_2) and longitudinal (T_1) relaxation, and the main mechanism for relaxation is dipole-dipole interaction. The evolution of the magnetization can be described by the Bloch equation (1.8) adjusted to include both transverse and longitudinal relaxation mechanisms:

$$\frac{dM}{dt} = \gamma \left(M \times B \right) - \frac{\left(M_z - M_0 \right) \hat{z}}{T_1} - \frac{M_x \hat{x} + M_y \hat{y}}{T_2} \tag{1.10}$$

1.3.1 Longitudinal relaxation, T_1

The term longitudinal relaxation describes the return of the net magnetization to its thermal equilibrium state, M_0, (parallel to B_0 and z) after the B_1 RF pulse has been turned off. The process is not instantaneous and occurs as a result of energy exchange between the spin system and lattice. This recovery is described by the Bloch equation:

$$\frac{dM_z(t)}{dt} = \frac{M_0 - M_z(t)}{T_1} \tag{1.11}$$

The rate of this recovery depends on how closely the spins are coupled to the lattice, and it therefore holds information on the mobility of the water molecules. Water molecules that are bound to other molecules like lipids and large proteins (macromolecules) have a shorter T_1 recovery because of their restricted motion, whereas free moving water molecules have a longer T_1. In the human brain this provides excellent tissue contrast because the Cerebro-Spinal Fluid (CSF) is mostly free water, the white matter has a high concentration of macromolecules and the gray matter is somewhere in between, with a low concentration of macromolecules and higher blood flow.

The signal in each tissue sample can be calculated using the Bloch equation. Immediately after the RF pulse is switched off, at time $t = 0$, the magnetization has a value $M_z(0)$. This value depends on the flip angle of the RF pulse. Equation 1.11 can be solved to give the value of M_z at time t for each tissue type as:

$$M_z(t) = M_0(1 - e^{-t/T_1}) + M_z(0)e^{-t/T_1} \tag{1.12}$$

where t is the time after the initial RF pulse has been applied. In the case of a 90° RF pulse, the magnetization vector M is flipped into the transverse plane where M_z is zero and the system is given the term *saturated.* At $t = 0$ the M_z is zero and then recovers to M_0 with relaxation time T_1. This process is known as saturation recovery and is shown as the blue curve in Figure 1.4a. The red curve in Figure 1.4a shows the process of inversion recovery. This happens when a 180° RF pulse is used and the magnetization vector M is rotated around x by 180 degrees to position $-M_0$.

The longitudinal recovery time T_1 can be measured using an inversion recovery experiment. When a 180° pulse is applied the magnetization is inverted but no phase coherence is induced, and therefore the signal cannot be measured. An RF pulse is then used to flip the magnetization into the transverse plane (and induce phase coherence) after an inversion time (TI). By repeating this for different values of TI, T_1 can be estimated. The T_1 is defined as the time taken for the signal to recover to 63% of M_0.

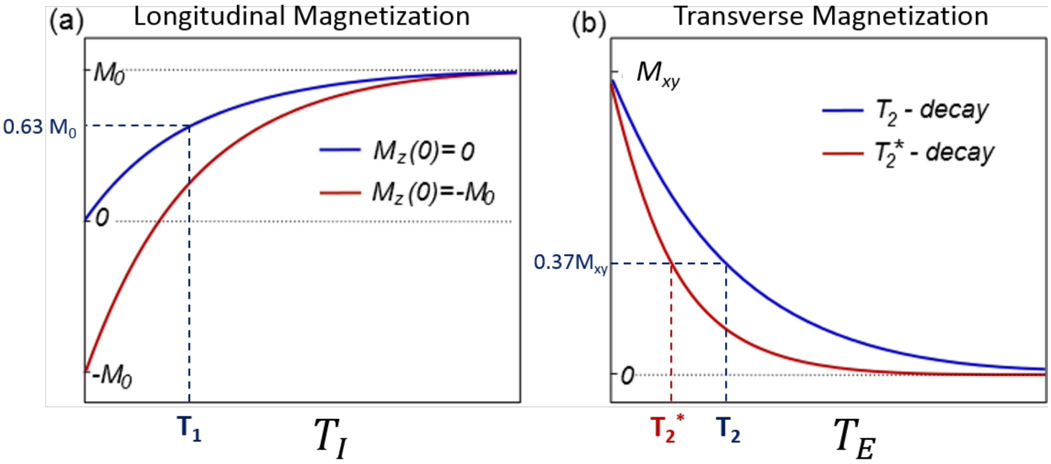

Figure 1.4: (a) Recovery of the longitudinal magnetization $M_z(t)$ for saturation (blue) and inversion (red) recovery. (b) Relaxation of the transverse magnetization $M_{xy}(t)$. T_2 decay is shown in blue and T_2^* decay is shown in red.

1.3.2 Transverse relaxation, T_2

While longitudinal T_1 relaxation is an energy loss phenomenon, transverse relaxation (T_2) is a signal loss phenomenon caused by the randomization of the spin orientations. Transverse relaxation, as the name suggests, happens in the transverse plane, so we will assume that a 90° RF pulse has perfectly tipped the magnetization into the x-y plane. When the RF pulse is turned off the individual spins undergo both longitudinal recovery and transverse dephasing due to local interactions between each other, leading to loss of phase coherence and transverse signal decay. This decay is shown as the blue curve in in Figure 1.4b and can be described by

$$M_{xy}(t) = M_{xy}(0)e^{-TE/T2} \tag{1.13}$$

As described before, the static effects can be forced to rephase and produce an echo of the FID signal with the use of a 180° RF pulse (SE). This refocusing pulse only refocuses spins that have dephased due to static B_0 inhomogeneities, and it gives a true T_2 contrast. By applying multiple 180° inversion pulses spaced 2τ apart, the FID can be refocussed again and again while decaying at a true T_2 rate. This is a common experiment for measuring T_2 and is the basis of the Carr-Purcell-Meiboom-Gill sequence (CPMG) experiment.

1.3.3 T_2^* contrast

In reality the transverse magnetization decays faster than predicted from T_2 decay alone, as shown by the red curve in Figure 1.4b. This is because the T_2 rate only describes the loss of coherence due to the interaction of spins with their neighbouring spins, producing microscopic local magnetic fields that disturb the precession of the spins of interest. In practice, imperfections in the static magnetic field B_0 cause further dephasing because each spin precesses at a slightly different local frequency. This accelerated decay is known as T_2^*, and is given by

$$\frac{1}{T_2^*} = \frac{1}{T_2} + \frac{1}{T_2^{'}} \tag{1.14}$$

where $T_2^{'}$ accounts for the dephasing caused by inhomogeneities in B_0, which are reversible. T_2^* is generally shorter at high field and is related to static dephasing caused by variation in the magnetic susceptibility of the tissue, providing another contrast mechanism known as Susceptibility Weighting Imaging (SWI). Examples of the type of contrast the three relaxation processes provide are shown in Figure 1.5. Contrast can be weighted by T_1 and T_2 by adjusting the TR (repetition time, TI in Figure 1.4) and TE (echo time) values in Figure 1.4. TR time can be adjusted to give more or less T_1 weighting, whereas TE can be adjusted to give more or less T_2 weighting to the image.

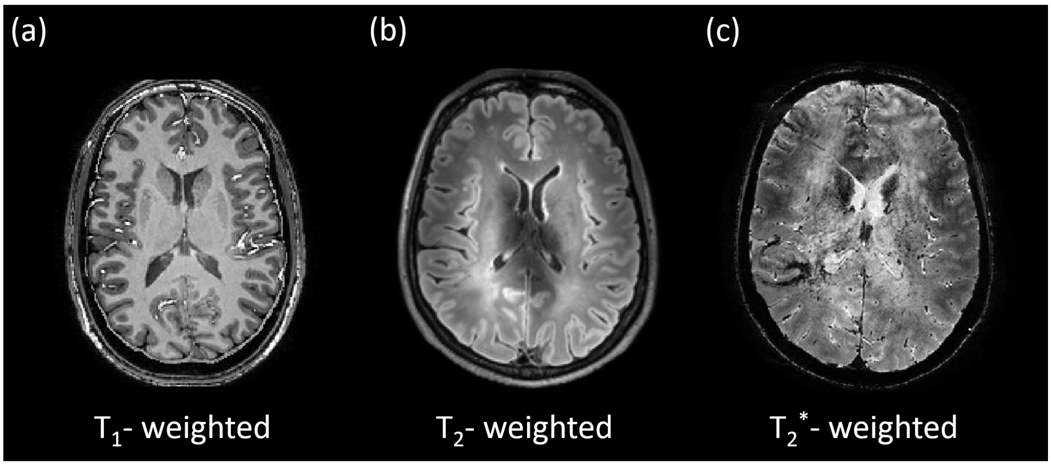

Figure 1.5: Different contrast can be achieved with T_1 weighted images (a), T_2 weighted images (b) and T_2^* weighted images (c). Note the switch of contrast between white matter (WM) and gray matter (GM) from the T_1 weighted image to the T_2 weighted image. Also note the loss of signal in the middle of the brain in the T_2 image; this is caused by the inhomogeneitiy of the transmit RF (B_1) and sub-optimal correction of this inhomogeneity.

1.3.4 Magnetization Transfer Contrast (MTC)

In order to understand the Magnetization Transfer (MT) phenomenon, first we have to understand how water behaves in living tissue. Water can either be moving freely or have its movement restricted by being attached (bound) to a hydration layer on the surface of a biological molecule. The mobility of water molecules depends on their chemical environment. In free moving water, the protons experience randomly fluctuating background magnetic fields caused by neighbouring protons, whereas in bound water the protons experience the magnetic field of the molecule (such as proteins) they are attached to. This results in a change of the local magnetic field, B_L, the proton experiences.

The rate at which B_L changes is related to the rate at which the water molecule is moving (tumbling). The amount of time taken for a water molecule to rotate, or tumble, through a single radian is related to the correlation time, τ_c, and is affected by viscosity and temperature (increases with increasing viscosity and decreases with increasing temperature). The spectral density ($J(w)$) of the sample, describing the frequency distribution of the resulting field components is defined as

$$J(\omega) = \frac{\tau_c}{1 + \omega^2 \tau_c^2} \tag{1.15}$$

Figure 1.6 shows how spectral density changes depending on the mobility of the water molecule and correlation time. The Larmor frequency (ω_0) is also shown on the logarithmic ω x-axis.

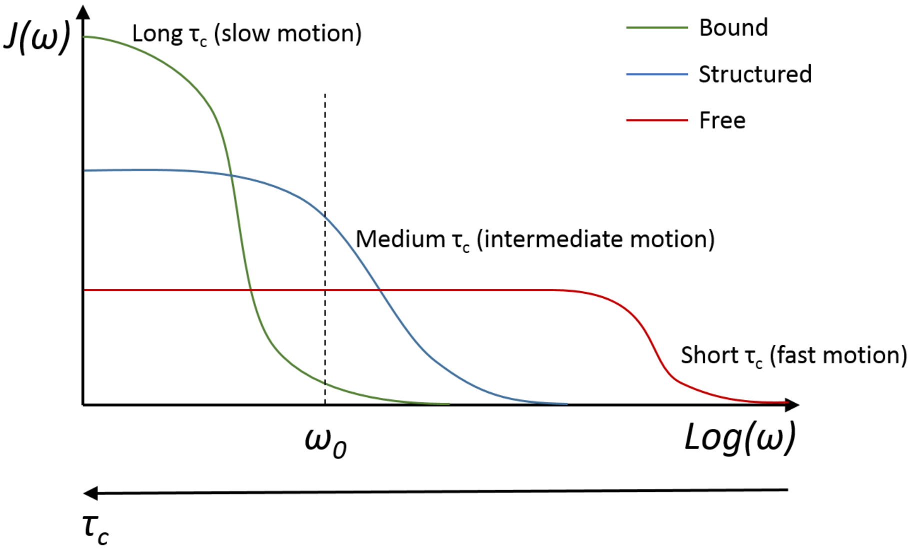

Figure 1.6: Spectral density ($J(\omega)$) as a function of correlation time (τ_c) and spin precession frequency (ω) for three different substances. Note that as τ_c increases, the precession frequency ω decreases.

Bound protons have a very broad resonance. These protons have a very short T_2, of the order of μs, and the signal decays before the receive coil is able to detect it, but MTC imaging allows for the indirect detection of these protons via their interaction with water.

Water is free to move between the different environments (bound, structured and free) and interact with those environments independently. Consider two proton pools (α and β), corresponding to free water and bound water respectively. If the magnetization in the bound pool (α) is saturated by applying an RF pulse off-resonance to water (ω_0), it will saturate the bound pool due to its very broad resonance frequency, but does not saturate the free water pool, β. After a time period during which exchange between the two pools occurs, the free water pool (termed saturated magnetization, M_S) is imaged and compared to an image of the free water pool without pre-saturation (unsaturated magnetization, M_0) of the bound pool. MTR is computed as:

$$MTR = \frac{M_0 - M_S}{M_0} \tag{1.16}$$

and relates to the amount of macromolecules in tissue, as well as multiple other factors explained in the next chapter of this report. An example of an MR image with MTR contrast is shown in Figure 1.7.

Figure 1.7: MTR contrast.

While MTR relates to the interaction between the bound and free water pools only (depending on frequency of applied saturation pulse), MT is a very broad term used to describe any transfer of magnetization, from both molecular and dipolar interactions, and it can be used to probe multiple exchange mechanisms and molecules. Chapter 2 of this report focuses on MT, from modelling the exchange process to designing an experiment to probe and image the exchange.

1.4 Principles of Imaging

The previous section introduced the theory of NMR and discussed where the signal comes from and how it can be detected. This section focuses on ways to localize the signal to produce a meaningful 2D or 3D image. Imaging using NMR was pioneered by Paul Lauterbur in 1973 when he proposed using linear field gradients applied at a range of different angles, together with back projection reconstruction to localize the NMR signal[6].

In the same year, Mansfield and Grannell[10] presented an alternative localization technique and the concept of imaging in k-space, and a year later a paper[3] describing a variety of selective excitation methods, including slice selection as it is used today. A year after that, Ernst's group published the first Fourier imaging method[5], using non-selective excitation and orthogonal linear gradients to generate 2D Fourier encoded images.

This gradient encoding technique led to multiple imaging methods, including Echo Planar Imaging (EPI)[9] by the Mansfield group in 1977, which is commonly used today. This section of the thesis outlines the main aspects of NMR imaging, from signal localization and slice selection, to frequency encoding, phase encoding and the concept of k-space.

1.4.1 Spatial Localization

Creating an image requires spatial knowledge of the NMR signal. This can be achieved by adding a small, spatially varying magnetic field onto the static external B_0 field, which changes the resonance frequency ω_0 of the sample as a function of position. The additional spatially varying magnetic field is produced by three orthogonal linear field gradient coils, G_x, G_y and G_z. The net field in the z-axis then becomes:

$$\mathbf{G} = G_x\hat{\mathbf{x}} + G_y\hat{\mathbf{y}} + G_z\hat{\mathbf{z}} \tag{1.17}$$

In the applied gradient field, the local magnetic field is determined by the amplitude of the z-component of the magnetic field at point $\mathbf{r}$ and is given by

$$B_z(r) = B_0 + \mathbf{G} \cdot \mathbf{r} \tag{1.18}$$

where B_0 is the external magnetic field strength, which leads to the Larmor frequency ω_0 of the spins being dependent upon position.

$$\omega(r) = \gamma(B_0 + xG_x + yG_y + zG_z) \tag{1.19}$$

Changing the frequency of the spin precession depending on physical position allows for three dimensional imaging of samples. This is generally achieved by slice selection along the z-axis, frequency encoding along the x-axis and phase encoding along the y-axis.

Slice Selection

A 90° RF pulse like the one shown in Section 1.2 of this chapter will excite all spins in a sample, as long as their resonance frequency is within the bandwidth of the RF pulse, and is therefore described as a *non-selective* pulse. When the RF pulse is applied in the presence of a field gradient, only spins precessing at a Larmor frequency within the bandwidth of the pulse will be tipped into the x-y plane. This is known as selective excitation and results in a thin 'slice' of excited spins. The thickness (Δz) of the excited slice is determined by the bandwidth of the RF pulse, $\Delta\omega$ and the amplitude of the gradient field, G_z, by

$$\Delta z = \frac{\Delta\omega}{\gamma Gz} \tag{1.20}$$

Applying the RF pulse in the presence of a field gradient results in a reversible phase shift across the slice. This shift can be corrected by applying a reversed slice gradient, at the same amplitude as the slice select gradient, but half the duration. This is shown in Figure 1.8b.

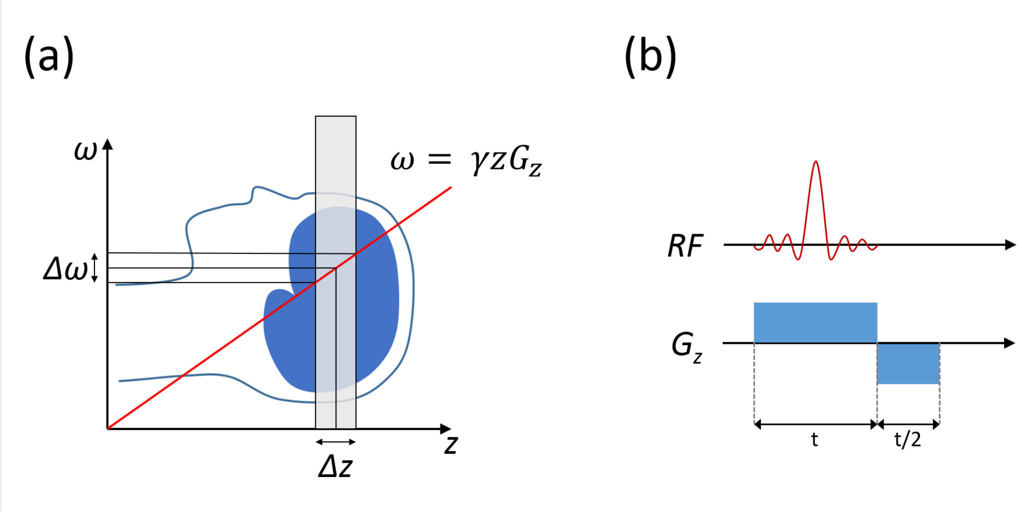

Figure 1.8: Principle of slice selection in MRI. (a) shows how slice selection can be used to excite a thin slice on the z-axis, and how the thickness of the slice depends on the gradient amplitude (G_z) and the bandwidth of the RF pulse ($\Delta\omega$). (b) shows how the RF pulse is applied in the presense of a field gradient, and the negative gradient required to refocus the phase shift created by the slice selective gradient.

The location of the slice on the z-axis can also be adjusted so that different parts of the sample (like the human brain in Figure 1.8a) can be imaged. This can be done by using an RF pulse at a different frequency. Shifting the location (frequency offset) of the RF pulse, $\Delta\omega$ up or down in Figure 1.8a will move the excited slice, Δz right or left along the z-axis.

Frequency Encoding

Frequency encoding works in the same principle as slice selection, but during the readout part of the experiment instead of the excitation part. Once the slice selective pulse has excited a thin slice in the z-axis, the slice can be considered as a 2D area of spins precessing at the same frequency. The signal coming from these spins therefore needs to be encoded, or localized, in the x and y directions too. A field gradient is applied in the x direction. If a positive gradient is applied in the x direction, it causes the spin precession frequency to increase with increasing distance in the x direction (Figure 1.9a).

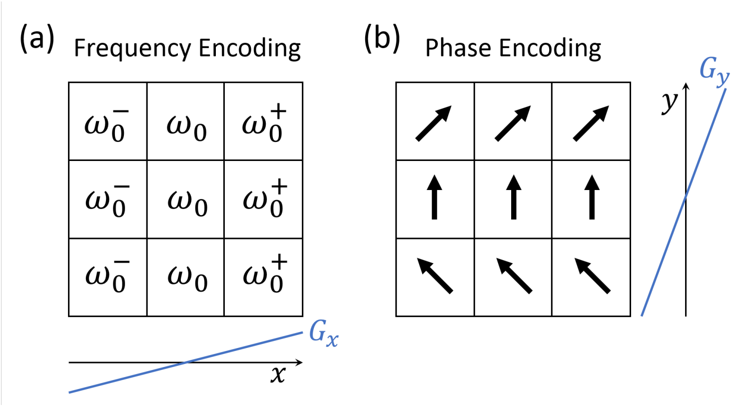

Figure 1.9: Spatial encoding in the x and y directions by frequency (a) and phase (b) encoding.

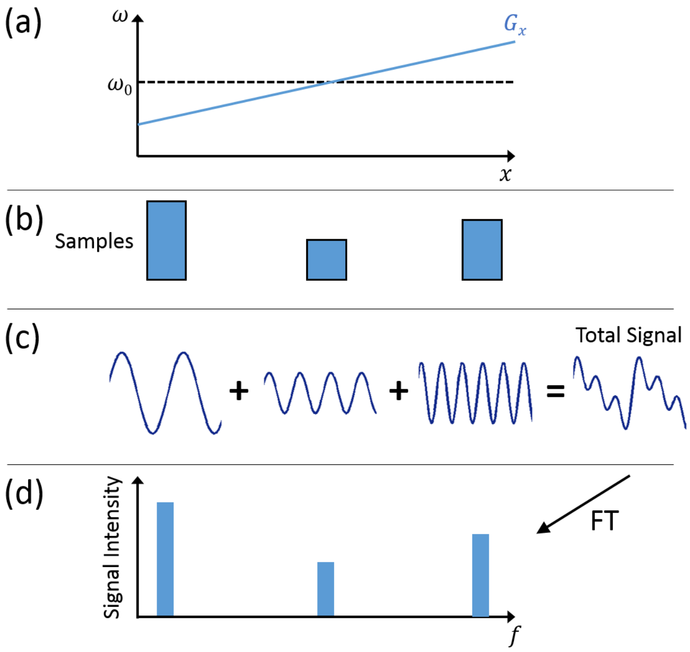

Figure 1.10: Frequency encoding in the x direction. (a) shows the applied G_x gradient. (b) shows the samples in the corresponding positions in the field gradient, precessing at different frequencies and inducing signal in the receive coil at different frequencies shown in (c). The total signal can then be Fourier Transformed to give a frequency histogram (d), where the signal intensity corresponds to the signal amplitude in (c).

Consider an example where three samples of different size are positioned in the x-plane of the magnetic field as shown in Figure 1.10a-b. When the signal in the x direction is read out by the receive coil, it is a mixture (summation) of all the different frequencies found in the x-plane (Figure 1.10c). Once the frequency signal has been sampled and digitised, it can be Fourier Transformed to give the amplitude of the signal for each sampled frequency (i.e. frequency histogram, Figure 1.10d). With knowledge of the external magnetic field, B_0 and gradient strength (given in $\mu T/m$), the frequency histogram can be encoded into position along the direction of the gradient, using further Fourier analysis.

Phase Encoding

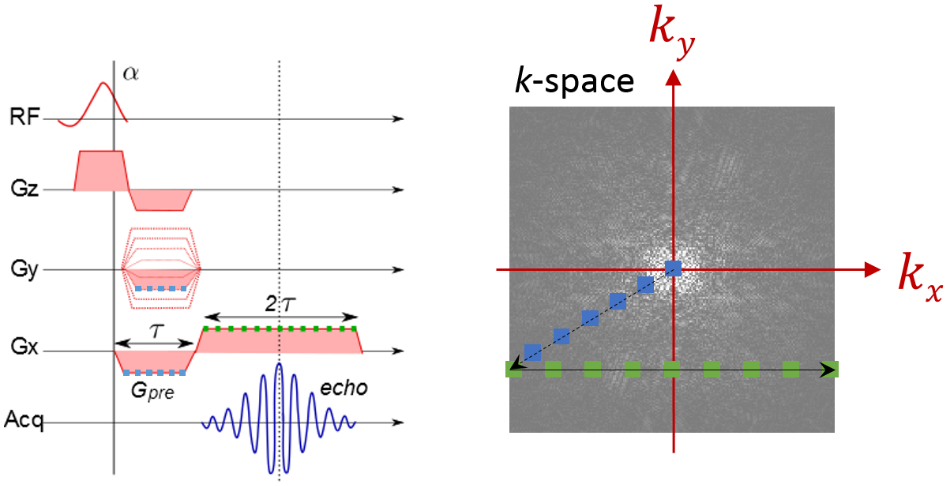

Figure 1.11: The basic gradient echo sequence (left) and the corresponding discrete sampling of one k-space line along k_x.

After slice selection and frequency encoding, the volume (slice) of interest has been excited and encoded in one direction. To produce a two dimensional image, the signal has to be encoded in the y-direction as well. This is achieved by phase encoding which localizes the signal orthogonal to the frequency encoding direction. Phase encoding creates a linear spatial variation of the phase of the magnetization by applying another gradient, G_y (Figure 1.11), after the slice selection pulse has tipped the magnetization in the transverse plane, but before each frequency encoding acquisition. This modifies the phase before each signal acquisition step, and different amounts of linear phase variation can be introduced by varying the strength of the phase encoding gradient G_y between repeats of frequency encoding. The result of this is a two dimensional sample of spins whose columns precess at different frequencies, and rows have different phase increments in each phase encoding step. This is illustrated in Figures 1.9 and 1.11.

The acquired time domain signal can be constructed to form a 2D space representing the frequencies along the x and y directions. This space indicates frequency of precession with respect to spatial position and hence is also known as the *spatial frequency* domain, or k-space[8]. The next section describes the concept of using gradients to create an image in k-space.

1.4.2 k-space

An image can be made up from the summation of thousands of sine and cosine waves of different frequency and orientation. The k-space holds the weighting factor for each of these waves[14]. The coordinates of k-space (k_x and k_y) are called spatial frequencies, and represent a sine or cosine wave across the entire image, describing the intensity of edges in the image. In MRI the signal is first acquired into k-space (or Fourier space, k_x,k_y,k_z) and later transformed into the Cartesian space (x,y,z) via inverse Fourier transformation. Figure 1.12 shows the relationship between k-space and the resulting acquired image.

The centre of k-space, or origin (where k_x and k_y are zero) holds the low frequency information like coarse image structure, while the outer edges of k-space hold the high spatial frequencies and therefore information about edges and fine detail. k-space sampled at only low spatial frequencies will result in a blurry image, and the more samples acquired further away from the origin, the sharper the resulting image becomes.

k-space can also be a useful tool for visualizing the trajectories of the spins phase under the influence of field gradients. Immediately after an RF pulse and slice selection gradient, the sampling position is in the centre of k-space and the position at a time t, after excitation is proportional to the integrated gradient

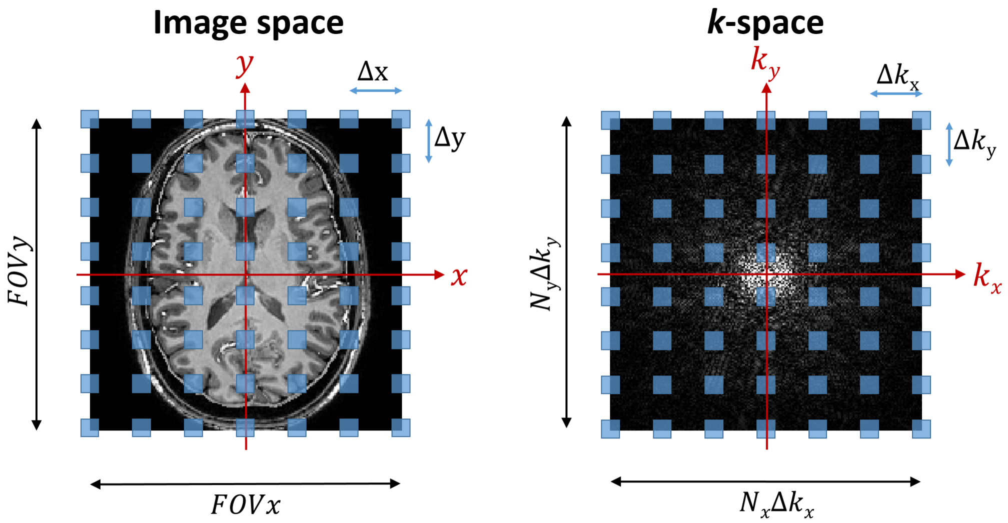

Figure 1.12: The Field of View (FOV) and spatial resolution of the image (left) are both a result of how the k-space (right) is sampled.

at that time. During frequency encoding, under the influence of a constant x-gradient, the signal evolves and k-space is sampled along the k_x direction. In phase encoding the location in k-space is changed without recording any signal, resulting in a jump of the sampling location along the k_y direction. To fully sample an image, all four quadrants of k-space must be covered by the read-out trajectory. An example of how the k-space is sampled is shown in Figure 1.11.

Figure 1.11 shows how the sampling location in k-space can be controlled using gradients along the x and y directions. To position the sampling location at the beginning of a k-space line, both negative G_x and G_y are applied. Signal acquisition then begins in the presence of a positive frequency encoding, G_x gradient. The echo is formed when the area under the positive lobe of the readout gradient, G_x, matches the area under the pre-phase gradient, G_{pre}. Sampling of k-space is done at discrete intervals along the trajectory path, as indicated by the green squares in Figure 1.11. The FOV of the resulting MR image (see Figure 1.12) is determined by the spacing of the measurements in k-space :

$$FOV_{x,y} = \frac{1}{\Delta k_{x,y}} \tag{1.21}$$

Ultimately the FOV and spatial resolution of the MR image depend on the sampling spacing ($\Delta k_{x,y}$) of the k-space, and distance sampled away from the origin of k-space, respectively (i.e. total area under applied gradients). Two commonly used k-space trajectories are shown in 1.13.

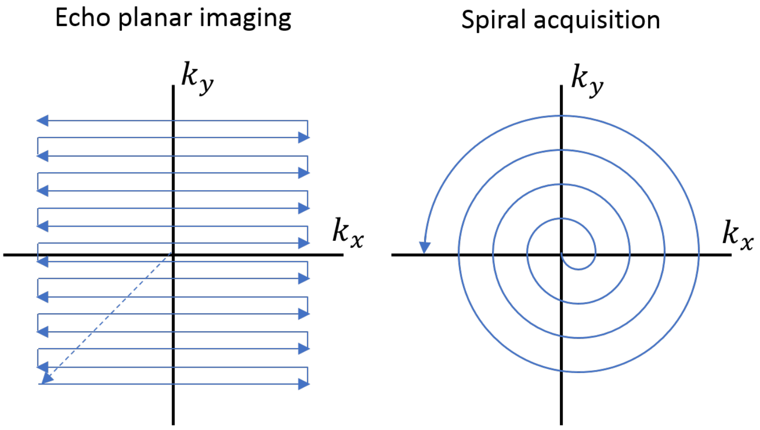

Figure 1.13: k-space trajectories.

Accelerated k-space sampling

k-space contains the complex signal and has conjugate symmetry. As mentioned before, a single point in k-space represents a frequency in the whole of the resulting image, and because of this, under-sampling the k-space can speed up the acquisition without necessarily losing signal or spatial resolution. In principle, acquiring half of k-space as shown in Figure 1.14**B** leads to a reduced SNR but no loss of sharpness or resolution. This is know as *half Fourier* imaging.

Reducing the k-space coverage has the advantage of producing good image quality at a reduced acquisition time, but it also introduces artefacts if the data is not in phase at the centre of k-space.

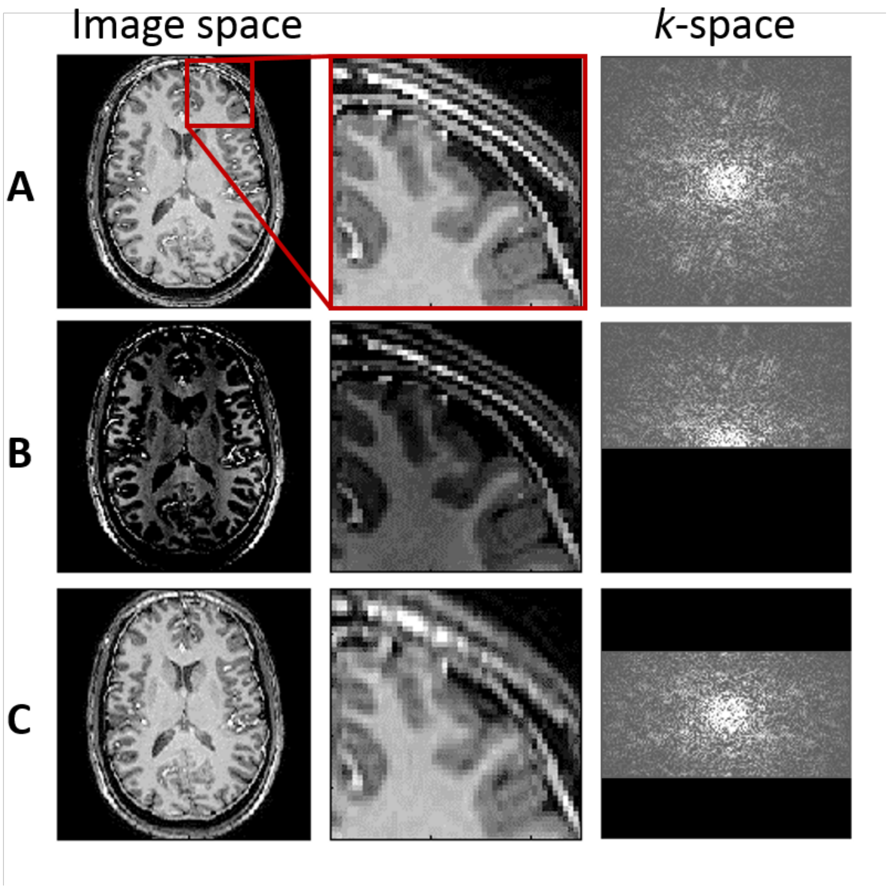

Figure 1.14: Relationship of k-space sampling to sharpness and SNR of MR images. Row **A** shows an MR image produced with full k-space coverage. Row **B** shows the effect of sampling only half of the k-space (while zero-filling the other half), giving the same resolution and FOV as in row **A** but lower SNR (the intensity of the images in row **B** has been increased for visualization purposes). Row **C** shows the result of not sampling the high spatial frequencies in the k_y direction in k-space . This results in half the resolution in the vertical direction and a blurrier image, but no SNR (or signal intensity) loss.

Three dimensional imaging can be achieved via multi-slice 2D imaging or by also sampling k-space in the z-direction with the use of the G_z gradient for spatial encoding instead of slice selection. The textbook by Bernstein et al.[1] covers the k-space in great detail.

The introduction of multi-coil arrays has also opened up new possibilities for accelerated k-space sampling. Initially developed to improve SNR, multi-coil arrays can be designed to cover multiple areas of the k-space simultaneously (hence termed *parallel imaging*), reducing total acquisition time. In parallel imaging multiple decoupled RF receive coils are used, each with a separate preamplifier and digitizer, and therefore separate sensitivity profiles. The signal from all separate receive coils can be combined for higher SNR, but because the FOV of the separate coils overlap, it is possible to use the coil profiles to provide the same spatial encoding and undersample high resolution data. Part of the object outside the FOV of each coil creates a signal that wraps back into the image after Fourier transform, but techniques like SENSitivity Encoding (SENSE)[12] are able to reconstruct the unwrapped images.

1.4.3 Field Mapping

Field mapping is of particular importance in the work described in this thesis, and indeed for all quantitative study of NMR signal. Field inhomogeneities in both B_0 and B_1 can perturb the quantitative results, particularly when both sensitivity and specificity of certain effects (like MT and CEST) are highly dependent on the static and RF magnetic fields. Robust and quantitative in-vivo mapping of B_0 and B_1 is an essential prerequisite for quantitative MRI.

$\mathbf{B_0}$ mapping

The static magnetic field, B_0, inhomogeneity can be measured using a double gradient echo field mapping sequence (Figure 1.15). In this sequence, two gradient echo images are acquired with different echo times (TE_1 and TE_2).

The local magnetic field, B_z, will modify the phase of the spins in that area. The difference in phase, $\Delta\phi(r)$, between the two images acquired at TE_1 and TE_2 is proportional to the field in the voxel and the echo time difference, ΔTE by

$$\Delta\phi(r) = \gamma \cdot B_z(r) \cdot \Delta TE. \tag{1.22}$$

The field offset from B_0 can then be estimated as

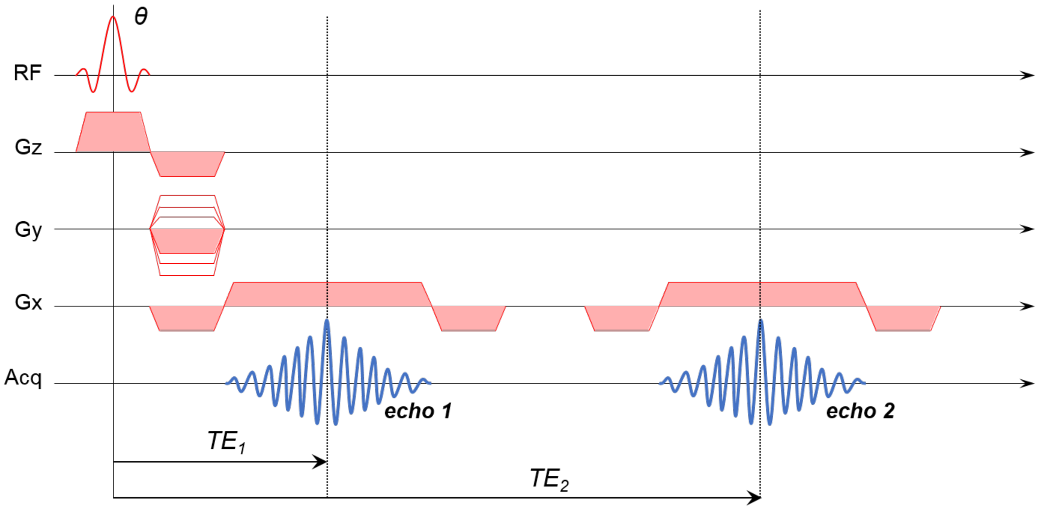

Figure 1.15: B_0 mapping, double echo sequence.

$$\Delta B_z(r) = \frac{\Delta\phi(r)}{\gamma \cdot \Delta TE}. \tag{1.23}$$

Field maps generated using this method give the variation in B_0, or frequency offset, for each voxel in the imaged slice or volume (Figure 1.16 (right)), and can be used to correct distortion in images or errors in quantitative data. More specifically, in the case of MT and CEST where saturation is given to frequencies far off-resonance to water, the saturation frequency must be known accurately and robustly.

B$_1$ mapping

B_1 describes the spatial distribution of the transmitted RF field across the recorded FOV. This is again of particular importance to the work presented in this thesis as it is the major factor affecting MT and CEST, and has to be accurately and robustly recorded. The inhomogeneity of the RF field depends on, among other factors, the B_0 strength and the size of the object being imaged. The RF tissue-specific wavelength depends on ω_0, and in the human brain at 7T is around 13cm. This also happens to be the average width of the human brain, leading to constructive interference in the middle of the brain, and destructive interference at the edges of the brain (Figure 1.16 (left)).

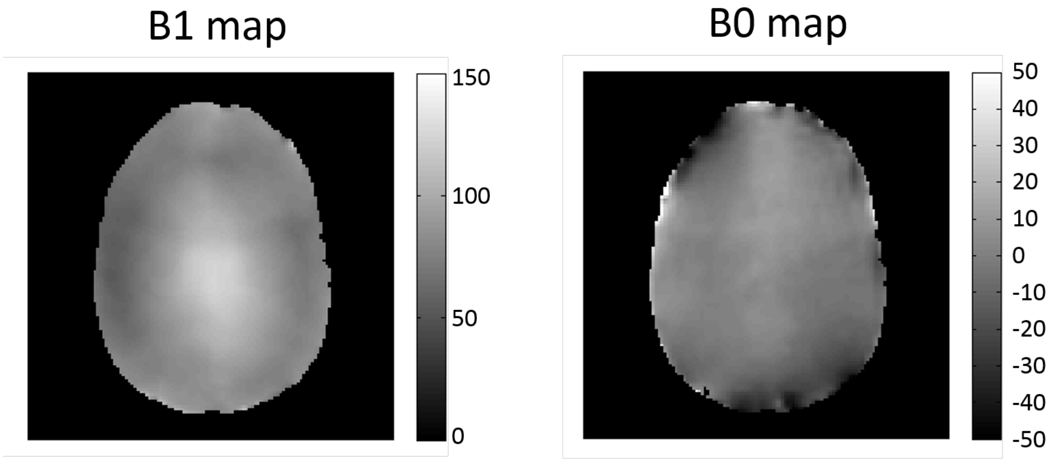

Figure 1.16: B_1 map (left) and B_0 map (right). The scale of the B_1 map is shown in percentage of requested flip angle, α, and the scale of the B_0 map is shown as frequency offset from ω_0, in Hz.

RF shimming techniques[2,11] are being developed, but monitoring the local Specific Absorption Rate (SAR) of such techniques is difficult, limiting their use (for now) in the human brain. While B_1 inhomogeneities are still unavoidable, methods have been developed to accurately measure them[13,15]. The most common method, and the one used in the work presented in this thesis, is the Actual Flip angle Imaging (AFI) method[15].

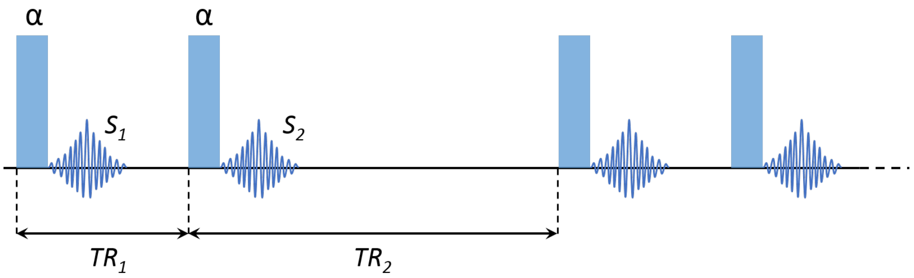

Figure 1.17: Timing diagram of the AFI dual TR pulse sequence.

The AFI method uses two identical RF pulses with flip angle (FA) α followed by two delays TR_1 and TR_2 (Figure 1.17). The method assumes relaxation effects to be non-negligible and therefore uses short repetition times ($TR_1 < TR_2 < T_1$), resulting in pulsed steady state of magnetization. A solution of the Bloch equations for the steady state AFI sequence gives the longitudinal magnetization before each excitation pulse as:

$$M_{z,1} = M_0 \frac{1 - E_2 + (1 - E_1)E_2 cos\alpha}{1 - E_1 E_2 cos^2\alpha} \tag{1.24}$$

and

$$M_{z,2} = M_0 \frac{1 - E_1 + (1 - E_2)E_1 cos\alpha}{1 - E_1 E_2 cos^2\alpha}, \tag{1.25}$$

where $E_{1,2} = exp(-TR_{1,2}/T1)$ and M_0 is the equilibrium magnetization. The recorded signal (S_1 and S_2 in Figure 1.17) can then be expressed as:

$$S_{1,2} = M_{x1,2} \exp^{-TE/T_2^*} sin\alpha. \tag{1.26}$$

Because TR_1 and TR_2 are very short, first order approximation of the exponential terms can be applied, and the ratio, r, of the two signals becomes

$$r = S_2/S_1 \approx \frac{1 + n\cos\alpha}{n + \cos\alpha}, \tag{1.27}$$

where $n = TR_2/TR_1$. The actual flip angle can then be estimated as

$$\alpha \approx \arccos\frac{rn - 1}{n - r}. \tag{1.28}$$

This actual flip angle can be used to create maps like the one in Figure 1.16 (left), and represents the percentage of requested FA for each voxel. This knowledge can be used to correct quantitative effects that depend on B_1 , assuming the evolution of the effects with B_1 is known. The concept of B_1 correction is discussed in detail in the following chapters.

1.5 Summary

This chapter has introduced the principles of NMR, from understanding nuclear spin, how it interacts with applied magnetic fields and how signal can be generated. Various contrasts mechanisms have been discussed, including MTC which forms the basis of most of the work presented in this thesis. Finally, field mapping methods are discussed as they are vital in understanding and correcting various effects in MT and CEST.

Bibliography

[1] Matt a Bernstein, Kevin E. King, Xiaohong Joe Zhou, and Wilson Fong. *Handbook of MRI Pulse Sequences*, volume 32. 2005. ISBN 0120928612.

[2] Qi Duan, Peter van Gelderen, and Jeff H. Duyn. Tailored excitation using nonlinear B0-shims. *Magnetic Resonance in Medicine*, 67(3):601–608, 2012.

[3] A N Garroway, P K Grannell, and P Mansfield. Image formation in NMR by a selective irradiative process. *Journal of Physics C: Solid State Physics*, 7(24):L457–L462, 1974.

[4] R. H. Hashemi, W. G. Bradley, and C. J. Lisanti. *MRI: The basics.* 2012. ISBN 0781741572.

[5] Anil Kumar, Dieter Welti, and Richard R. Ernst. NMR Fourier zeugmatography. *Journal of Magnetic Resonance (1969)*, 18(1):69–83, 1975.

[6] P. C. Lauterbur. Image Formation by Induced Local Interactions: Examples Employing Nuclear Magnetic Resonance. *Nature*, 242(5394):190–191, 1973.

[7] Malcolm H Levitt. *Spin Dynamics: Basics of Nuclear Magnetic Resonance.* John Wiley and Sons, 2001. ISBN 9780471489221.

[8] Stig Ljunggren. A simple graphical representation of fourier-based imaging methods. 1983.

[9] P. Mansfield. Multi-Planar Image Formation Using NMR Spin Echoes. *Journal of Physics C: Solid State Physics*, 10:L55–L58, 1977.

[10] P Mansfield, P K Grannell, Carr H Y M, Purcell E, Stalker D C Mansfield P, Orchard M J, Richards K H B, Elleman D D Rhim W-K, Vaughan R W, Tanner J E, Huber L M Waugh J S, and Haeberlen U. NMR 'diffraction' in solids? *Journal of Physics C: Solid State Physics*, 6(22):L422–L426, nov 1973.

[11] Weihua Mao, Michael B Smith, and Christopher M Collins. Exploring the limits of RF shimming for high-field MRI of the human head. *Magnetic resonance in medicine*, 56(4):918–22, oct 2006.

[12] Klaas P. Pruessmann, Markus Weiger, Markus B. Scheidegger, and Peter Boesiger. SENSE: Sensitivity encoding for fast MRI. *Magnetic Resonance in Medicine*, 42(5):952–962, 1999.

[13] Patrick Schuenke, Johannes Windschuh, Volkert Roeloffs, Mark E Ladd, Peter Bachert, and Moritz Zaiss. Simultaneous mapping of water shift and B1 (WASABI)-Application to field-Inhomogeneity correction of CEST MRI data. *Magnetic resonance in medicine*, feb 2016.

[14] D David Stark and G William Bradley. *Magnetic Resonance Imaging, 3rd edition.*, volume 1. Mosby, 3 edition, 1999. ISBN ISBN 0-8151-8518-9; 28607.

[15] Vasily L Yarnykh. Actual flip-angle imaging in the pulsed steady state: a method for rapid three-dimensional mapping of the transmitted radiofrequency field. *Magnetic resonance in medicine*, 57(1):192–200, jan 2007.

Chapter 2

Z-spectroscopy

This chapter describes the mechanisms behind MT and CEST contrast [7,32,41] in the human brain at 7T, together with experimental design criteria and limitations. The term Magnetization Transfer (MT) can be confusing as it implies transfer of magnetization between any proton pools and via any mechanism, but each exchange mechanism produces a separate, measurable effect. In fact the term MT is generally used to refer to dipole-dipole exchange via the macromolecular peak, whereas CEST is the study of transfer of magnetization between mobile compounds and free water, and has contributions of both chemical exchange and dipolar cross-relaxation. This chapter discusses the investigation of both MT and CEST effects at 7T using z-spectroscopy and introduces various semi- and fully-quantitative methods of measuring these effects.

2.1 Magnetization Transfer

MT is a method of generating contrast that provides information on the macromolecular density and tissue integrity of the human brain [16]. It originates from NMR [3], but in an MRI context it was first used by Balaban *et al.* [39] while attempting to perform a spin transfer experiment. As mentioned in the previous chapter, the MRI signal comes only from mobile protons which have sufficiently long T_2 (>2ms) so that signal can be detected before it decays. These protons, termed the *free pool*, are weakly coupled due to motional narrowing[37] and therefore have a very narrow absorption lineshape (red line in Figure 2.1).

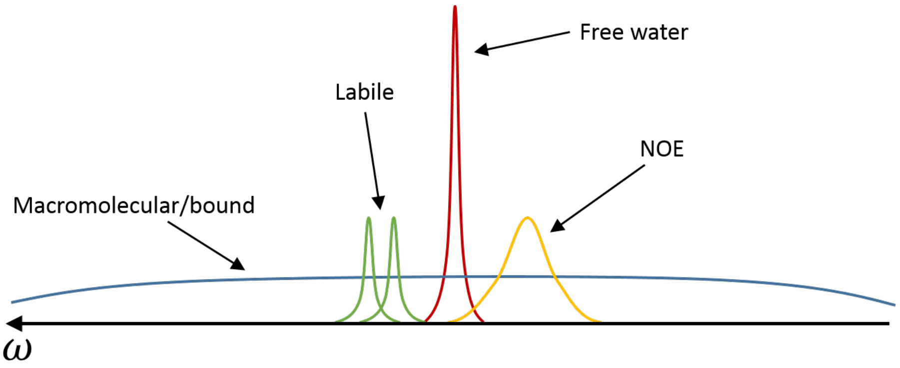

Figure 2.1: Absorption lineshapes for the different proton pools. Note that there are multiple labile pools.

In contrast, protons in macromolecules have highly restricted motion. They experience static and low frequency magnetic fields from neighbouring nuclei and have very short T_2 values (<1ms). So short, in fact, that the signal from them decays too rapidly to be detected directly by conventional NMR. These protons are strongly coupled to each other resulting in a very broad absorption lineshape (in the order of kHz, blue line in Figure 2.1), which makes them much more sensitive to off-resonance radio frequency (RF) irradiation. The width, or full width at half maximum (FWHM) of the absorption lineshape of the proton pools is inversely related to the T_2 of each pool[7].

There also exists another layer of protons between the *free* water pool and the macromolecules, closely associated with the surface of macromolecules, termed the *hydration* layer. In this layer, protons are moderately structured and have restricted motion because of hydrogen bonding with sites on macromolecules. Like protons in macromolecules, these protons in the hydration layer have very short T_2 and a broad range of resonance frequencies.

In a sample like the human brain, free water protons are in constant motion and often come in contact (or in very close proximity) with macromolecules and the hydration layer. When the free water protons are next to a macromolecule, their movement is restricted. These protons are then termed the bound pool protons, and while they are bound to the macromolecule, dipole-dipole exchange of magnetization can occur. MT is of particular importance because of the presence of a large bound proton pool in the myelin surrounding nerve axons in the brain, making MT imaging an ideal modality for investigating myelination in healthy and diseased brain.

2.1.1 The z-spectrum

To investigate this exchange of magnetization, saturation is given to protons in the bound pool that are resonating at a certain frequency offset compared to the free water frequency. The saturation is then gradually exchanged to the free water pool via the mechanisms mentioned above, and finally the signal from the free water protons is read out. Repeating this process at successive, different offset frequencies results in a spectrum that shows the variation in the reduction of water signal depending on saturation frequency, termed the *z-spectrum* (Figure 2.2). Direct saturation of the water frequency causes the measured signal to be completely nulled, giving a zero (or near zero) value on the *z-spectrum* at the water frequency. Any effects on the *z-spectrum* that are near the main water peak are therefore very difficult to distinguish and accurately measure, but because the absorption linewidth of free water is very narrow, this unusable range is limited.

The detected *z-spectrum* depends on multiple factors including RF saturation power and sampling frequencies. A *z-spectrum* like the one in Figure 2.2 shows how the water signal is attenuated to a varying degree for a large range of offset frequencies, sampling multiple exchange mechanisms such as inter and intramolecular dipole-dipole interactions, spin exchange or molecular exchange[5,33,39]. While such spectra hold information on multiple exchange mechanisms, observing the different mechanisms separately is very difficult. Importantly, exchange

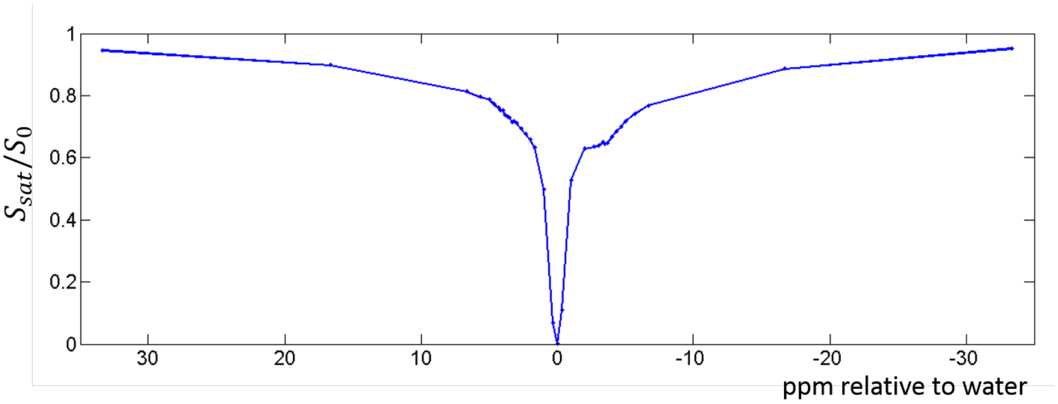

Figure 2.2: In-vivo *z-spectrum* at 7T showing the normalized water signal at each frequency offset sampled. Note the frequency (or ppm relative to water) axis is reversed like in traditional NMR spectroscopy.

of magnetization also influences the observed relaxation times of the measured free water pool. Various methods have been developed to separate the different exchange mechanisms, and are discussed later in this chapter.

Protons bound to different molecules experience varying shielding effects from the external field B_0, causing them to resonate at different frequencies. This is called chemical shift and it is caused by the chemical structure of the molecule and the electron cloud around the proton. Conventionally, the frequency axis in z-spectroscopy is shown from downfield to upfield (from positive to negative ppm values) relative to water. Protons upfield from water experience larger shielding, and therefore resonate at a lower frequency.

2.1.2 Source of MT signal

MT contrast is defined by the concentration of specific cell components like proteins and other macromolecules, together with their chemical environment. Transfer of magnetization can occur via two pathways, dipolar transfer of magnetization or proton exchange. When considering conventional MRI, an RF pulse is applied at the proton Larmor frequency, leading to energy absorption mainly by free water protons. The process of T_1 relaxation begins as soon as the RF

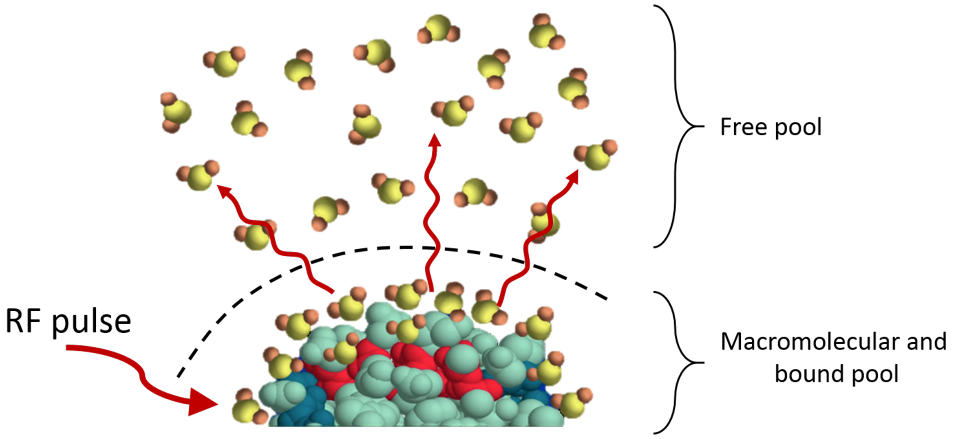

Figure 2.3: Magnetization Transfer mechanism. Saturation is given to the macromolecular proton pool using a frequency selective excitation pulse, and is then transferred to the free water proton pool directly or via the bound pool. (adjusted from[2]).

pulse is turned off, and during this time the absorbed energy is released into the lattice. The lattice includes nuclei that were not excited by the RF pulse in all available pools including the free water pool, macromolecule and bound pools. In an MT experiment, the opposite process occurs. i.e. saturation is given to macromolecular protons only (using a frequency selective excitation pulse that does not excite free water protons), and the energy (or saturation) is then transferred to the free water pool directly, or via the bound pool. This is illustrated schematically in Figure 2.3.

Various mechanisms relay the magnetization from macromolecules to free water, the main ones being direct dipole-dipole interactions. One type of interaction is the Nuclear Overhauser Effect (NOE), which is equivalent to dipolar cross-relaxation through space between two nuclear spins sufficiently close to each other, but drops very fast with distance ($1/r^6$). When free water molecules come in contact with larger proteins or macromolecules, hydrogen bonding (or hydration) occurs and the water molecule motion slows. There are multiple sites on proteins that water can bind to, with different resident lifetimes (τ_M), and each site can be described by a single Lorentzian distribution[15]. The binding sites are also subject to proton transfer, with the exchange rate being specific to each particular site, and are also sensitive to pH.

The semi-solid macromolecular MT is seen on the *z-spectrum* as a very broad, baseline effect with a resonance linewidth of several kHz, centred at approximately -2.4ppm relative to water. The very broad lineshape of this effect corresponds to the short T_2 times, in the order of μs, which provides a large frequency offset for Magnetization Transfer Contrast (MTC) imaging. With exchange rate to free water in the order of $40s^{-1}$[27] and a concentration relative to free water protons of up to 20% in cartilage[27] and up to 13% in the human brain[4], MT provides a sensitive and distinct tissue contrast mechanism. In the context of this thesis, this effect is referred to as the MT pool.

2.1.3 Chemical Exchange Saturation Transfer (CEST)

NMR spectroscopy can give information on spin density, spin-spin coupling, and properties related to the chemical environment of a nucleus, and has been used to quantify up to 20[29–31] metabolites in the brain at 7T. The very low concentration of metabolites and nuclear spins in living tissue, compared to water protons, strongly limits the study or imaging of these metabolites in terms of SNR and spatial resolution.

In CEST, saturation is given to exchangeable solute protons (just as in MT) that resonate at a frequency different from the that of the bulk water protons. The saturation is then transferred to the water protons when the solute protons exchange with water, and the water signal is slightly attenuated. Considering the very low concentration of the solute protons, the signal attenuation is very small, but because the water pool is much larger than the solute pool, each exchanging saturated solute proton is replaced by a non-saturated water proton, which is then again saturated[32]. If the exchange rate between the two pools is fast enough, a substantial enhancement of the saturation transfer effect is seen, allowing the detection of low concentration solutes or metabolites.

CEST effects can be seen on the *z-spectrum* (Figure 2.2) in the range of positive ppm values (0 - 5 ppm), and are caused by labile protons of functional groups like amide, amine and hydroxyl groups[41]. The chemical shift of these effects on the *z-spectrum* differs depending on the proton site in the molecule, but a direct assignment to metabolites in NMR spectroscopy is not possible, although connections between metabolites and CEST effects can be made if their exchange rates, chemical shifts and relaxation times are known.

As the name suggests, the exchange of saturation is a chemical reaction which is often base or acid catalysed. The exchange rate is therefore a function of temperature and pH, and ranges from $10s^{-1}$ for amides[45] to several $10{,}000s^{-1}$ for hydroxyl[40]. The observed CEST effects depend primarily on the concentration of the proton pool (amide, amine, hydroxyl) and the exchange rate between the pool and the free water pool. These two properties affect the *z-spectrum* in very similar ways and measuring them both simultaneously is very difficult, if not impossible.

2.1.4 Nuclear Overhauser Effect (NOE)

The right side of the *z-spectrum* (negative ppm values, upfield from water) is dominated by exchange between water and non-exchanging aliphatic and olefinic protons of macromolecules, resonating in the range of -2 to -5 ppm relative to water. Some recent work suggests that NOE signal can be seen from aromatic protons as well, resonating downfield from water in the range of 1 - 4 ppm[9].

The semi-solid MT contrast also originates from fast dipolar transfer via NOE through spin diffusion followed by transfer to water, but the immobile protons produce a broad, solid-state spectrum. On the other hand, the sharper NOE signal measured upfield of water comes from mobile macromolecular components with finite linewidth[12,33]. The fact that this magnetization transfer comes from non-exchangeable protons indicates either a direct through-space dipolar transfer[10,17] or a relayed mechanism via exchangeable protons[32].

As in the positive side of the *z-spectrum*, protons at different sites on the macromolecules resonate at different frequencies, possibly have different exchange rates to water, and therefore produce separate effects on the *z-spectrum*. Previous studies have shown the NOE effect to be pH-insensitive[11], but a relayed mechanism through exchangable protons means that at least some of the effect is sensitive to pH[32]. The NOE spectrum from z-spectroscopy has even been shown to be visually similar to the proton NMR macromolecular spectrum[12]. The observed NOE effect is therefore a compound peak, but is often modelled as a single peak centred at -3.5ppm relative to water.

Quantification of the upfield NOE effect is not trivial, particularly because of MT interference (MT is centred around -2.4ppm and NOE at -3.5ppm) and the Amide Proton Transfer (APT) effect on the opposite side of the spectrum, but methods have been developed to remove the MT contribution by scanning at low B_1 power, and fit for NOE and APT separately using Lorentzian lineshapes. The work in this thesis (see Chapter 5) suggests that MT and the upfield NOE effect are very strongly coupled in the healthy brain.

2.2 Effects of B_1, saturation time and B_0

All the effects described above that define the shape of the *z-spectrum* , depend on the parameters of the RF irradiation and the homogeneity of the external field, B_0. Because each effect (MT, CEST etc.) has a different exchange rate with water, the amplitude of the effect depends on the strength and duration of the RF irradiation.

Figure 2.4 shows how the shape of the *z-spectrum* changes with increasing B_1 saturation power. The CEST and NOE effects are more prominent in the lower

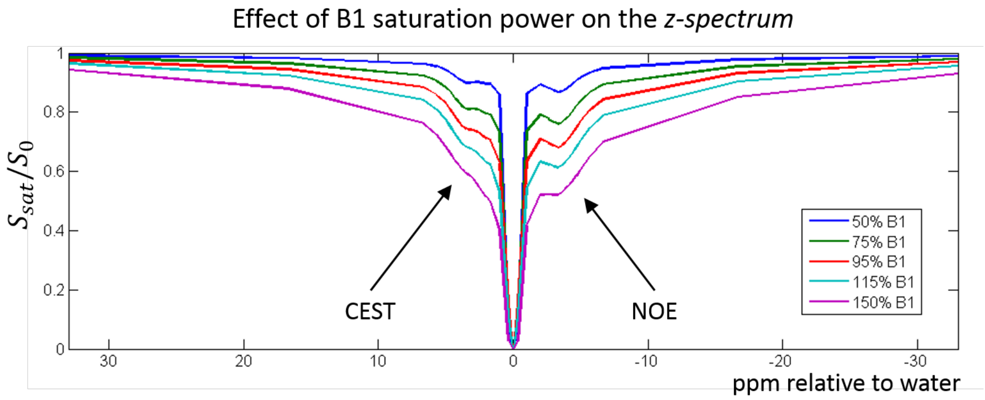

Figure 2.4: Numerically simulated z-spectra at a range of different B_1 saturation powers.

powers because there is less interference from the MT effect and direct water saturation (DS), whereas high saturation power is favourable for MT quantification. In the case of Continuous Wave saturation (CW), the amplitude and duration of the RF pulse is easily varied, giving control over the labelling efficiency of each effect, but Specific Absorption Rate (SAR) concerns limit the use of CW irradiation in-vivo. Instead, a pulsed irradiation scheme is employed.

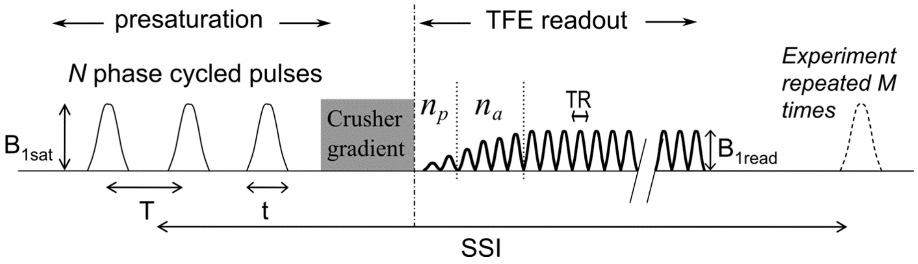

Figure 2.5: The pulsed irradiation MT experiment. Pre-saturation period followed by a readout scheme. The pre-saturation period consists of **N** number of pulses, of **t** ms length, spaced **T** ms appart, at B_{1sat} power. A crusher gradient at the end of the saturation pulse train removes any residual transverse magnetization. The attenuated water signal is then read out using an appropriate readout scheme with a low FA B_{1read}. n_p and n_a are ramped RF pulses before and at the start of the acquisition, respectively. SSI is the Shot to Shot Interval in the Turbo Field Echo (TFE) sequence. From[21].

Figure 2.5 shows a pulsed irradiation scheme. The amplitude and duration of the saturation pulse can be controlled with B_{1sat}, pulse duration **t**, and pulse spacing **T**. While pulsed irradiation gives some control over the saturation scheme, it is very difficult to describe analytically.

Static field, B_0, inhomogeneities also have a strong effect in z-spectroscopy. The rf irradiation is given to a narrow band of frequencies (≈200Hz), and targeted at specific frequencies for CEST, NOE and MT respectively. If the irradiation frequency has an offset based on inhomogeneities of the field, the irradiation is given to a frequency slightly shifted with respect to the one requested. This leads to a shifted spectrum and also poor labelling of the effects.

While B_0 shimming produces a relatively homogeneous field, frequency shifts of up to 100Hz can still be seen across the human brain. Field mapping (see Chapter 1) allows for accurate mapping of the field inhomogeneities, and if the inhomogeneity is known across the volume, the spectra can be shifted and re-interpolated to the original sampled frequencies using methods like Water Saturation Shift Referencing (WASSR)[14].

2.3 Modelling Magnetization Transfer

The simple two pool model described by Henkelman *et al.*[6,7] is useful in describing the basics of magnetization transfer when trying to understand exchange between proton pools or compartments of a model. This model, shown in Figure 2.6, shows the transfer of magnetization between two pools - the liquid, or free water pool, **A**, and the semi-solid, or macromolecular pool, **B**.

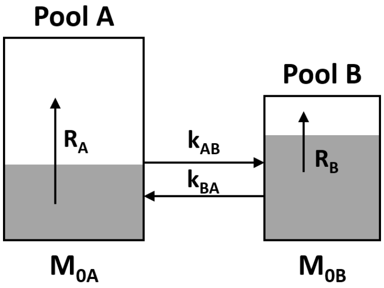

Figure 2.6: The two pool model of magnetization transfer. Pools A and B are the free water pool and semi-solid macromolecular pool respectively. R_A and R_B represent the longitudinal relaxation rates of each pool, and M_{0A} and M_{0B} are the relative equilibrium magnetization of each pool. The transfer of magnetization between pools A and B is shown as k_{AB} and k_{BA}. Adjusted from[7].

The free water pool is larger than the macromolecular pool, as can be seen by the relative size of the compartments in Figure 2.6, and saturation of the free water pool depends on the saturation of pool **B**, the relaxation rates R_A and R_B, and exchange rates k_{AB} and k_{BA}. After RF irradiation, in each pool, some of the spins are in the longitudinal orientation (or unsaturated), shown as the unshaded part of the compartment, and the rest of the spins are saturated (shaded, lower part of compartment). As long as the exchange rate between the two pools (k_{AB} and k_{BA}) is faster than the relaxation rate R_A, saturation of the free water pool can be measured.

The work presented in this thesis describes the measurement of full z-spectra in the approach to steady state *in-vivo* at 7T, and quantifying the parameters of three proton pools; the MT, NOE and APT pools[4]. To allow quantification of the three pools, the two pool model was extended to a four pool model as discussed below. The Bloch McConnell equations[18] were used to numerically simulate the transfer of magnetization between the four compartments.

2.3.1 Four compartment model

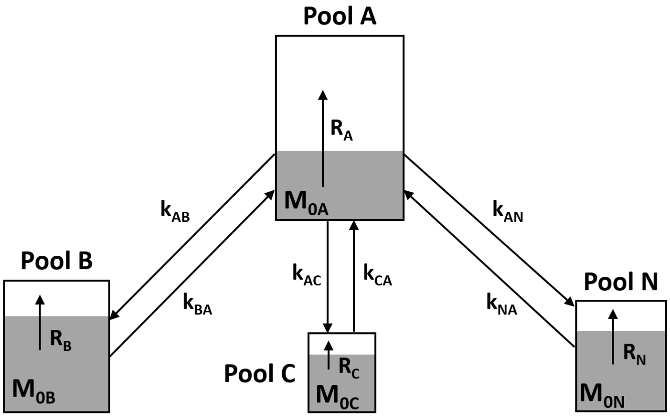

Figure 2.7: The four pool model of magnetization transfer. Pools A and B are the free water pool and semi-solid macromolecular pool respectively, and pools C and N are the exchangeable protons and upfield NOE protons respectively. The longitudinal relaxation times of each proton pool are shown, together with the exchange rates to water.

The model assumes four interacting proton pools which are (i) the free water magnetization describing the water moving freely in the intra or intercellular space (free pool, M_f), (ii) the macromolecular protons and protons in the hydration layer of proteins and macromolecules (bound pool, M_b), (iii) a smaller pool of labile protons in chemical exchange with the free pool (exchanging pool, M_c), and (iv) the non-exchanging aliphatic and olefinic protons responsible for the NOE effect (NOE pool, M_n). The proton pools are assumed to be in exchange with water, but any exchange between the pools (M_b to M_c etc.) is ignored (Figure 2.7). The evolution of each proton pool, except for the bound pool, is described by modified Bloch equations, while each pool is considered to have a single transverse relaxation time T_2. The bound pool (M_b) is instead modelled by a symmetric Super-Lorentzian lineshape function[19,26], although a recent study suggests inhomogeneous broadening of the lineshape[34]. The model of Woessner *et al.*[38] is used to describe the evolution of magnetization in our four compartment model:

$$\frac{dM(t,\omega_{rf})}{dt} = A(t,\omega_{rf}) \cdot M(t,\omega_{rf}) + B \cdot M_0 \tag{2.1}$$

where

$$M(t,\omega_{rf}) = \begin{pmatrix} M_x^f(t,\omega_{rf}) \\ M_y^f(t,\omega_{rf}) \\ M_z^f(t,\omega_{rf}) \\ M_x^b(t,\omega_{rf}) \\ M_y^b(t,\omega_{rf}) \\ M_z^b(t,\omega_{rf}) \\ M_x^c(t,\omega_{rf}) \\ M_y^c(t,\omega_{rf}) \\ M_z^c(t,\omega_{rf}) \\ M_x^n(t,\omega_{rf}) \\ M_y^n(t,\omega_{rf}) \\ M_z^n(t,\omega_{rf}) \end{pmatrix}, M_0 = \begin{pmatrix} 0 \\ 0 \\ M_0^f \\ 0 \\ 0 \\ M_0^b \\ 0 \\ 0 \\ M_0^c \\ 0 \\ 0 \\ M_0^n \end{pmatrix}, B = \begin{pmatrix} 0&0&0&0&0&0&0&0&0&0&0&0 \\ 0&0&0&0&0&0&0&0&0&0&0&0 \\ 0&0&\frac{1}{T_1^f}&0&0&0&0&0&0&0&0&0 \\ 0&0&0&0&0&0&0&0&0&0&0&0 \\ 0&0&0&0&0&0&0&0&0&0&0&0 \\ 0&0&0&0&0&\frac{1}{T_1^b}&0&0&0&0&0&0 \\ 0&0&0&0&0&0&0&0&0&0&0&0 \\ 0&0&0&0&0&0&0&0&0&0&0&0 \\ 0&0&0&0&0&0&0&0&\frac{1}{T_1^c}&0&0&0 \\ 0&0&0&0&0&0&0&0&0&0&0&0 \\ 0&0&0&0&0&0&0&0&0&0&0&0 \\ 0&0&0&0&0&0&0&0&0&0&0&\frac{1}{T_1^n} \end{pmatrix}, \tag{2.2}$$

$$A(t,\omega_{rf}) = \begin{pmatrix} -\frac{1}{T_2^f}-k_f & -2\pi\Delta_f & 0 & k_{bf} & 0 & 0 & k_{cf} & 0 & 0 & k_{nf} & 0 & 0 \\ 2\pi\Delta_f & -\frac{1}{T_2^f}-k_f & -\omega_1(t,\omega_{rf}) & 0 & k_{bf} & 0 & 0 & k_{cf} & 0 & 0 & k_{nf} & 0 \\ 0 & \omega_1(t,\omega_{rf}) & -\frac{1}{T_1^f}-k_f & 0 & 0 & k_{bf} & 0 & 0 & k_{cf} & 0 & 0 & k_{nf} \\ k_{fb} & 0 & 0 & -\frac{1}{T_2^b}-k_{bf} & -2\pi\Delta_b & 0 & 0 & 0 & 0 & 0 & 0 & 0 \\ 0 & k_{fb} & 0 & 2\pi\Delta_b & -\frac{1}{T_2^b}-k_{bf} & -\omega_1(t,\omega_{rf}) & 0 & 0 & 0 & 0 & 0 & 0 \\ 0 & 0 & k_{fb} & 0 & \omega_1(t,\omega_{rf}) & -\frac{1}{T_1^b}-k_{bf}-R_b(\omega_{rf}) & 0 & 0 & 0 & 0 & 0 & 0 \\ k_{fc} & 0 & 0 & 0 & 0 & 0 & -\frac{1}{T_2^c}-k_f & -2\pi\Delta_c & 0 & 0 & 0 & 0 \\ 0 & k_{fc} & 0 & 0 & 0 & 0 & 2\pi\Delta_c & -\frac{1}{T_2^c}-k_{cf} & -\omega_1(t,\omega_{rf}) & 0 & 0 & 0 \\ 0 & 0 & k_{fc} & 0 & 0 & 0 & 0 & \omega_1(t,\omega_{rf}) & -\frac{1}{T_2^c}-k_{cf} & 0 & 0 & 0 \\ k_{fn} & 0 & 0 & 0 & 0 & 0 & 0 & 0 & 0 & -\frac{1}{T_2^n}-k_{nf} & -2\pi\Delta_c & 0 \\ 0 & k_{fn} & 0 & 0 & 0 & 0 & 0 & 0 & 0 & 2\pi\Delta_c & -\frac{1}{T_2^n}-k_{nf} & -\omega_1(t,\omega_{rf}) \\ 0 & 0 & k_{fn} & 0 & 0 & 0 & 0 & 0 & 0 & 0 & \omega_1(t,\omega_{rf}) & -\frac{1}{T_2^n}-k_{nf} \end{pmatrix}, \tag{2.3}$$

In these matrices, the superscript f indicates the free water pool, b indicates the bound pool, c the exchangeable protons, or CEST pool and n the NOE pool. (M_x^i, M_y^i, M_z^i) are the components of the magnetization for each pool, where $i = f, b, c$, or n. M_0^i is the equilibrium magnetization for each pool, and T_1^i and T_2^i are the longitudinal and transverse relaxation times of each pool. Δ_i represents the difference in frequency between the applied saturation pulse of amplitude $\omega_1(t)$ and frequency ω_{rf}, and the chemical shift of the corresponding pool δ_i. The exchange rates between each of the pools and the free water pool are shown as k_{bf}, k_{cf} and k_{nf}, and the rates from water to the other pools are shown as k_{fb}, k_{fc} and k_{fn}. The relationship between the forward (to water) and backward (from water) exchange rates is defined by the equilibrium magnetization of each pool as

$$k_{ij} = \frac{M_0^j}{M_0^i} k_{ji} \tag{2.4}$$

k_f represents the total exchange rate between the free water pool and all other pools, and is the sum of the rates k_{fb}, k_{fc} and k_{fn}. $R_b(\omega_{rf})$ describes the Super-Lorentzian lineshape of the bound pool. It is important to note that the longitudinal and transverse relaxation times of the free water pool depend on the relaxation parameters of all the other pools, where:

$$\frac{1}{T_1^{obs}} = \frac{1}{T_1^f} + \frac{M_0^b}{M_0^f}\frac{1}{T_1^b} + \frac{M_0^c}{M_0^f}\frac{1}{T_1^c} + \frac{M_0^n}{M_0^f}\frac{1}{T_1^n} \tag{2.5}$$

and

$$\frac{1}{T_2^{obs}} = \frac{1}{T_2^f} + \frac{M_0^b}{M_0^f}k_{bf} + \frac{M_0^c}{M_0^f}k_{cf} + \frac{M_0^n}{M_0^f}k_{nf} \tag{2.6}$$

For the work presented in this thesis, SAR and time restrictions limit the acquisition of *in-vivo* 7T z-spectra to a pulsed pseudo-steady-state scheme. To study the approach of the system to steady-state, an Ordinary Differential Equation

(ODE) solver was implemented. This enabled the computation of the evolution of the magnetization of the different pools during the approach to saturation, using a 4^{th} order Runge-Kutta algorithm with a $10\mu s$ interval. A pulse by pulse numerical simulation was implemented, with the resulting value of M_z^f used to plot the *z-spectrum*, using the method described in[20].

2.4 MT imaging sequences

Imaging the magnetization transfer effects is another variable to consider when designing a quantitative MT/CEST methodology. The most effective labelling of magnetization transfer effects is when the exchanging pool is fully saturated, but achieving that requires very long saturation, usually in the order of 3-5 seconds. In *in-vivo* scanning, the RF power delivered must be kept as low as possible, and within SAR limitations, so a trade-off between saturation, spectral and spatial resolution is always present. The design of the MT experiment must take all these factors into account, and can be split into two parts: saturation and image readout.

2.4.1 Saturation

Saturation of exchanging protons is best performed with CW rectangular pulses of long duration and narrow bandwidth, since the saturation bandwidth is proportional to $1/t_{sat}$. The CW saturation is also easy to model analytically, and allows for a straightforward optimisation to achieve maximum CEST contrast. However, specifically at ultra high field (7T), SAR regulations and hardware limitations preclude the use of CW irradiation, and instead require a pulsed irradiation scheme[28].

Pulsed saturation consists of a train of RF pulses followed by a readout, or RF pulses interleaved with a segmented readout. Both schemes are shown in

Figure 2.8 as **Pulsed SAT** and **Pulsed segmented SAT** respectively. Pulsed saturation (middle diagram in Figure 2.8) offers a wide variety of parameter control, useful in characterizing the desired saturation. These parameters include saturation power, pulse width/bandwidth, number of pulses, duty cycle and pulse shape. Gaussian or Gaussian windowed Sinc pulses[25] are commonly used as they can achieve narrow bandwidth ($\sim$ 200Hz) with little to no sidebands.

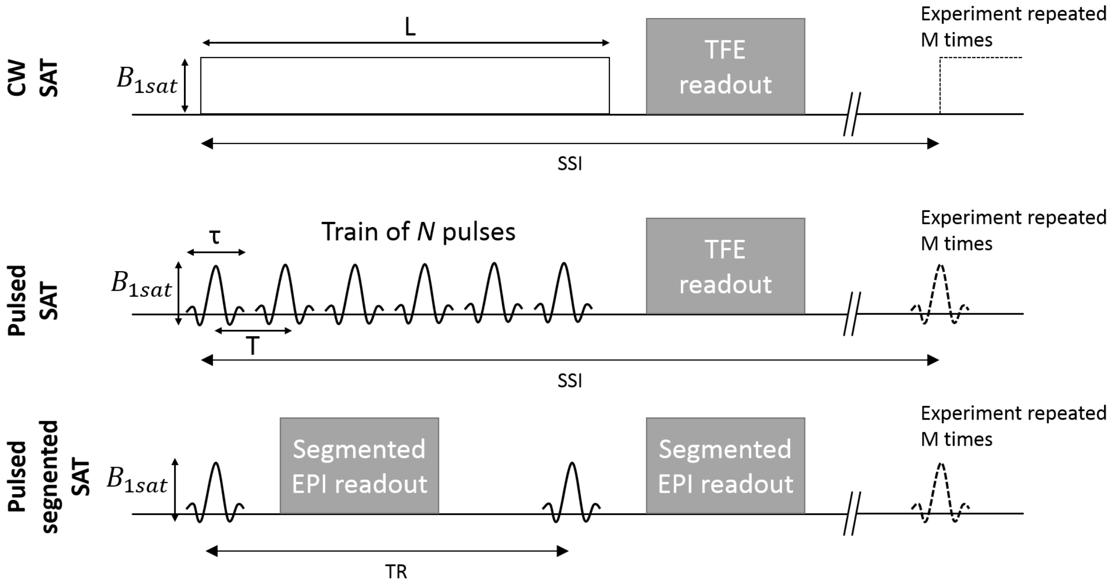

Figure 2.8: Three commonly used saturation schemes for MT imaging. The top diagram shows an example of a CW saturation scheme, with saturation power B_{1sat} and saturation pulse length L. The middle and bottom diagrams show pulsed saturation schemes when using a train of pulses (middle) or interleaved RF pulses with a segmented readout (bottom). In the case of pulsed saturation (middle), the pulse duration (τ) and time delay between saturation pulses (T) can be adjusted, giving control over the duty cycle of the entire saturation train.

2.4.2 Imaging

Several unconventional saturation/imaging schemes have been developed to acquire *z-spectra*, like dual band irradiation to assess the broadening of the semi-solid macromolecular pool[34] and Gradient-Reversed Ultrafast Z-Spectroscopy (GRUFZS)[35] to speed up *z-spectrum* acquisition, but the two most commonly used imaging schemes are shown in Figure 2.8. These methods are known as transient state (or pseudo-steady state) readout (Figure 2.8 middle) and steady-state segmented readout (Figure 2.8 bottom).

The transient state readout offers a higher degree of parameter control and is therefore the method of choice for all the work presented in this thesis. This method has also been proven to be more sensitive to CEST effects at low saturation power than the steady-state readout [13]. The transient state readout consists of a train of N RF saturation pulses at a given off-resonance frequency, followed by a Turbo Field Echo (TFE) readout. The TFE readout comprises of a chain of rapidly acquired, single gradient echoes, sampling k-space from the centre outwards, radially, as the signal reaches a steady state and the MT contrast decays with T_1 and saturation effects. An M number of shots (usually 3-5) are required to achieve the desired FOV and spatial resolution, and a shot-to-shot interval (SSI) of $\sim$3s is used to allow the longitudinal magnetization of the different pools to relax back to equilibrium before the next saturation train is applied.

The steady-state acquisition scheme (bottom of Figure 2.8) is made up of interleaved RF saturation pulses and segmented EPI readout. The steady-state signal is built up over M number of TRs and k-space is sampled from outer edges to the centre, radially, so that when the centre of k-space is sampled the magnetization is already in steady state. This imaging scheme does not require a delay between repeats as the magnetization is in steady state, and is therefore a potentially quicker scan, although the SNR/time is generally lower.

2.5 Review of quantification methods

Since the discovery of magnetization transfer as a new contrast mechanism in the human brain, the need to robustly and accurately measure the effect has become apparent. Early attempts at quantifying the effects focused on a simple two pool model (free water pool and bound pool) or Magnetization Transfer Ratio (MTR), but acquiring a full *z-spectrum* where multiple pools can be measured simultaneously, quickly gained popularity. The following section offers a brief review of the quantification methods used in MT and CEST, from MTR, MT asymmetry and Lorentzian fitting, to full Bloch McConnell equation fits and finally our approach of using a database (or Look-Up-Table) of pre-simulated spectra.

2.5.1 Magnetization Transfer Ratio (MTR)

MTR, also referred to as MT Contrast (MTC), studies the basic transfer of magnetization from a saturated pool of protons (usually the bound pool) to the unsaturated free water pool. MTR is widely used in clinical environments because it is a relatively short scan, possible at low B_0 field strength (1.5T and 3T) and it offers an indirect marker of myelin. The method involves acquiring one image without a saturation RF pulse, and another image with a saturation RF pulse. The ratio between the two images is then calculated as

$$MTR = \frac{M_0 - M_S}{M_0} \tag{2.7}$$

where M_0 and M_S are the unsaturated and saturated images respectively. Alternatively, if a full *z-spectrum* is acquired, MTR can be computed by taking M_0 far off-resonance to water ($\geq$50kHz) where no bound pool protons are excited, and M_S as an image closer to the water frequency, where bound pool protons (or CEST/NOE protons) are saturated. The measured MTR effect scales with the power (B_1) of the saturation RF pulse, which is inherently inhomogeneous in the human brain at 7T, but the relationship between MTR and B_1 has been proven to be approximately linear within a sensible range, and therefore easy to correct[23,24].

The contrast in MTR imaging is directly related to the frequency of the M_S image, and can be weighted by multiple effects. The frequency of the M_S image is usually chosen to sample only the bound pool protons, and hence give an MT-weighted contrast, but it can also be chosen to sample NOE or CEST protons.

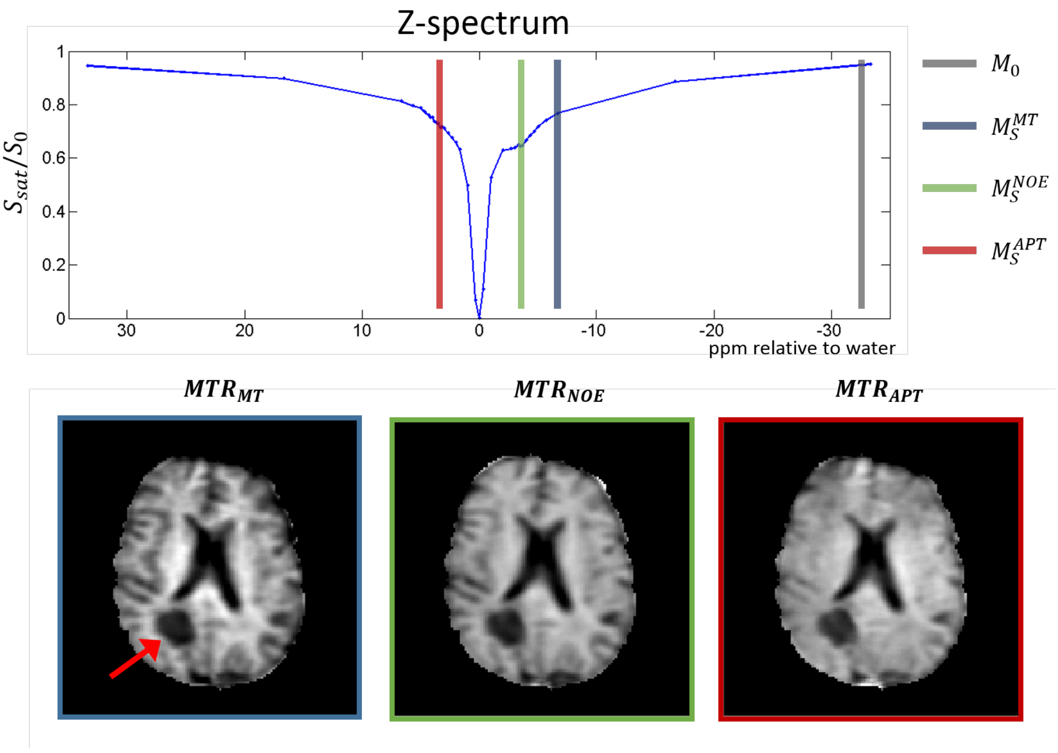

Figure 2.9: MTR images of a patient with a Glioma brain tumour, with MT, NOE and CEST contrast weighting, computed using equation 2.7, where the images used as M_0 and M_S are shown as coloured vertical lines on the *z-spectrum*. Three MTR images are shown, weighted by MT (blue), MT+NOE (green) and MT+APT/CEST (red). The MT-weighted image shows the highest contrast between WM and GM, but no difference in contrast can be seen in the tumour, indicated by the red arrow.

In the latter cases, the contrast has a mixture of MT and NOE/CEST weighting (Figure 2.9), unless the MT signal is suppressed.

2.5.2 Asymmetry analysis

The presence of the wide, Super-Lorentzian bound pool lineshape, together with the symmetric water peak in z-spectra, make quantification of NOE and CEST effects very difficult. Asymmetry analysis of z-spectra[8] has the potential to remove both bound pool MT and DS effects from the spectra, assuming they are symmetrical around the water peak. To do this, MT asymmetry is defined as the difference between the MTR values at the positive offsets and the corresponding negative offsets with respect to water:

$$MTR_{asym} = MTR(+\Delta\omega) - MTR(-\Delta\omega) \tag{2.8}$$

By removing one side of the spectrum from the other, after B_0 correction has been performed, it is assumed that the MT and DS effects are both symmetric and cancel themselves out, leaving only the NOE and CEST effects to be visible.

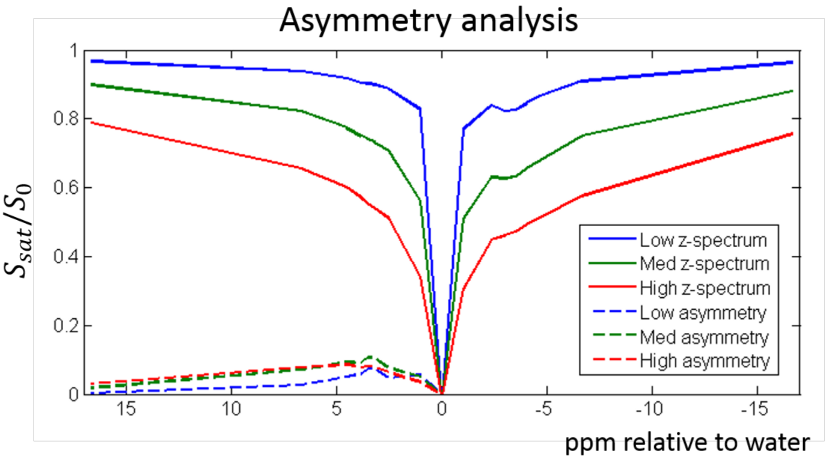

Figure 2.10: Asymmetry analysis on *in-vivo* 7T human brain z-spectra, recorded at 3 different B1 saturation powers.

In reality, at 7T the bound pool lineshape is not symmetrical around the water peak, but at around -2.4ppm relative to water, and it is therefore not entirely eliminated by MT asymmetry. This can be seen as a shift of the asymmetry peak maximum (dotted red line in Figure 2.10) away from water as the saturation power (and therefore MT contribution) increases. Also, the NOE and CEST effects are observed at -3.5ppm and 3.5ppm respectively, so the MT asymmetry measure at 7T is still a mixture of MT, NOE and CEST effects. MTR asymmetry at frequency offset $\Delta\omega$ is therefore more accurately described as

$$MTR_{asym}(\Delta\omega) = MTR^{CEST}_{asym}(\Delta\omega) + MTR^{MT}_{asym}(\Delta\omega) + MTR^{NOE}_{asym}(\Delta\omega) \tag{2.9}$$

Although this signal is a mixture of several individual effects, MT asymmetry has been used to image multiple abnormalities like early ischemia in anaesthetized rats[45], and cancer through an increase in cellular protein/peptide content of malignant cells with respect to normal tissue[44]. This method has sparked an interest in the study of the positive side of the *z-spectrum* (around 3.5ppm) and has led to the development of more quantification methods.

2.5.3 Lorentzian fitting

In order to give more specificity to the various effects seen on a *z-spectrum*, the spectrum can be fitted with a sum of Lorentzian functions, each describing an individual effect, in the same way that metabolites are fitted to NMR spectra in an LCModel-based approach[22]. The macromolecular (bound pool) baseline is modelled by a Super-Lorentzian lineshape, but all other longer T_2 effects, including DS, can be modelled by Lorentzian lineshapes of amplitude A and FWHM, W, centred at a frequency offset relative to water, ω_{ref}. The summation of a number of effects can be used to fit an *in-vivo z-spectrum*, and is defined[1,42] as

$$L_{fit} = 1 - \sum_{i=1}^{N} A_i \left[1 + \left(\frac{\Delta\omega - \omega_{ref,i}}{0.5 W_i} \right)^2 \right]^{-1} \tag{2.10}$$

where N is the number of proton pools fitted and L_{fit} is the entire fitted spectrum. The fit process works by minimising the square of the difference between L_{fit} and the acquired spectrum (least squares approach). Figure 2.11 shows an example of Lorentzian fitting on *in-vivo* 7T human brain spectra.

The Area Under the Curve (AUC) of each fitted Lorentzian function can then be used as a measure of the relative concentration of each pool, while the FWHM of each function gives an estimate of the T_2 of each pool. The drawback of this method is that each observed effect scales differently with B_1 saturation

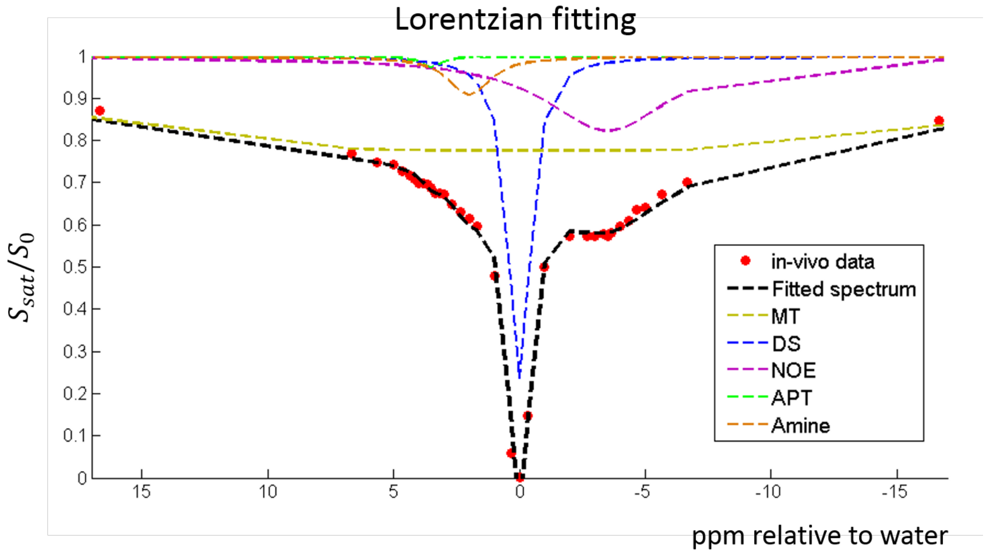

Figure 2.11: Fitted *z-spectrum* of a white matter voxel in the human brain at 7T. The red dots show the acquired data and the dotted black line shows the resulting lineshape from a five pool fit. The five individual Lorentzian functions (MT, DS, NOE, APT and Amine) are also shown.

power, and two voxels of the same tissue, experiencing different B_1 saturation, will produce very different *z-spectra*. This is particularly problematic at 7T where the B_1 field is inherently inhomogeneous. Additionally, the shape of the *z-spectrum* also depends strongly on the observed water T_1, and in cases like Glioma, where the tissue in and around the tumour becomes more liquid (and therefore has longer T_1), the Lorentzian fitted AUC results will be T_1-weighted.

To solve the problem of B_1 dependence, spectra can be acquired at multiple powers to investigate the evolution of each effect with increasing B_1 power. Once this is known, for each voxel, all AUC values can be rescaled to a target B_1 value. The accuracy of this method depends on how many powers are recorded, but is feasible with as low as two powers[36]. In the case of two powers, if linearity is assumed, where B_1 power is equal to zero, AUC is also zero. Figure 2.12 shows a schematic of this method.

The method described in Figure 2.12 is effective in removing the effect of B_1 from Lorentzian fitted AUC values, but not the effect of T_1. A recent study has

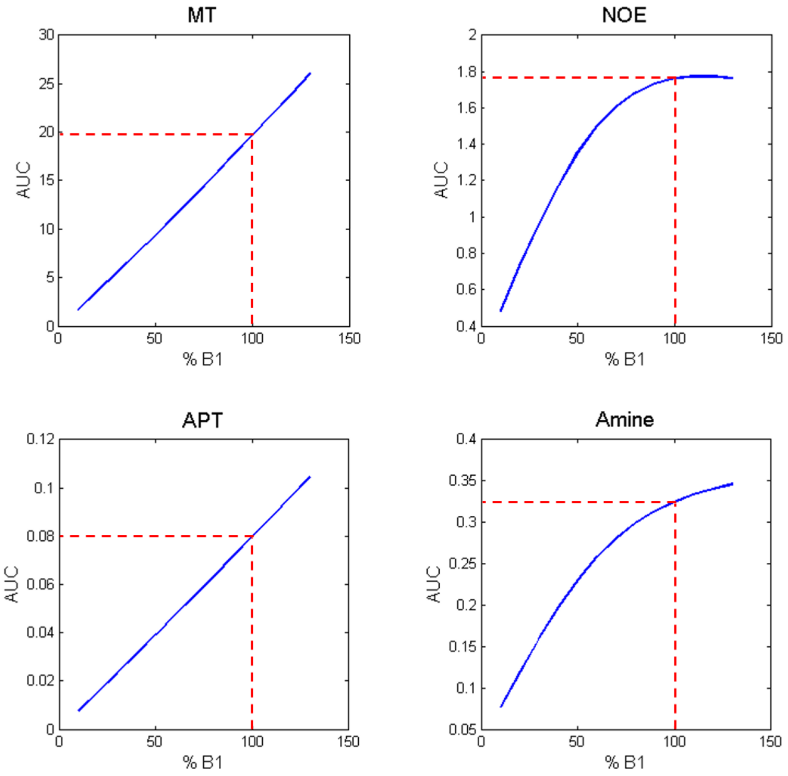

Figure 2.12: Schematic of B1-corrected AUC values from Lorentzian fitted data. The blue lines show smoothing spline functions fitted to three datapoints (two powers and a zero B_1 value - not shown). The dotted red lines show how AUC values can be selected for a target B_1. Note: The method shown here is applied to every voxel, and in regions of low power deposition, the target B_1 may fall outside the range of acquired data, in which case the smoothing spline function is interpolated outwards.

shown that the effects add up inversely in the *z-spectrum*[43], and therefore a new method has been suggested where spillover and MT corrected CEST contrast can be achieved by an inverse analysis of the *z-spectrum*. In this method, a spectrum consisting of all Lorentzian functions except that of the pool of interest (i.e. APT), termed the reference spectrum, $Z_{ref,APT}$, is inversely subtracted from the complete fit of the *z-spectrum*, termed Z_{lab}, to give MTR_{Rex}

$$MTR_{Rex,APT} = \frac{1}{Z_{lab}} - \frac{1}{Z_{ref,APT}} \tag{2.11}$$

This measure can finally be divided by the observed T_1 to give a relaxation-compensated CEST value, termed AREX[36,42].

$$AREX_{APT} = \frac{MTR_{Rex,APT}}{T_{1,obs}} \tag{2.12}$$

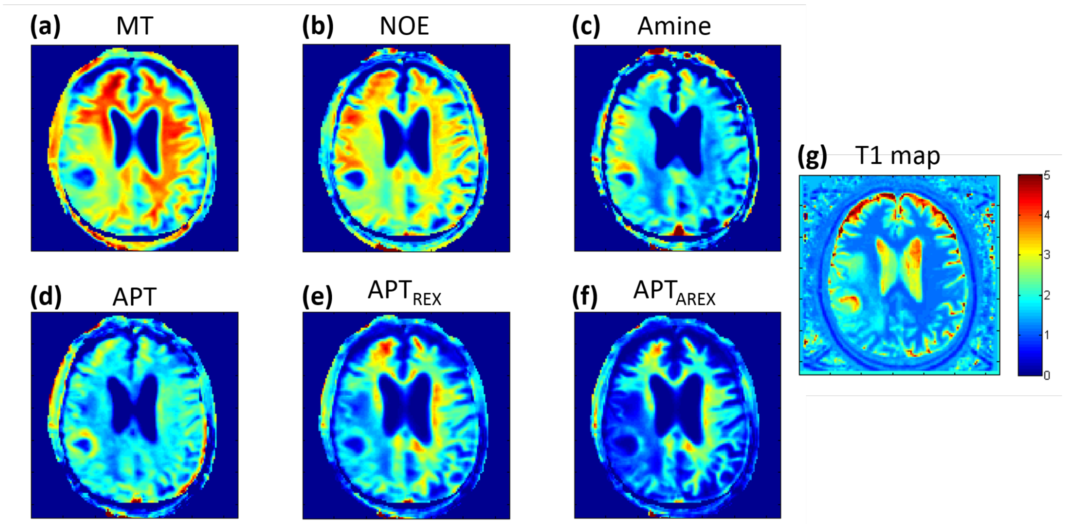

Figure 2.13: B1-corrected Lorentzian fit maps for MT, NOE, Amines and APT (**a-d**) and the corresponding APT_{REX} and APT_{AREX} maps (**e,f**). The APT signal around the Glioma tumor reduces when the signal is corrected for T_1. A T_1 map (colour scale in seconds) is also shown for comparison (**g**).

Figure 2.13 shows AUC maps from the Lorentzian lineshape fitting method, corrected for B_1, MT, spillover (DS) and T_1. Parts **(a-d)** show the results of fitting a five pool model and correcting the AUC values for B_1 using the method explained in Figure 2.12. The APT map **(d)** shows a ring of high intensity around the Glioma tumour, but this almost disappears when the values are corrected for T_1 **(f)**. Parts **(d)-(f)** show the same APT map calculated using the method described in Figure 2.12, equation 2.11 and equation 2.12 respectively. The T_1 map shown in **(g)** suggests that the ring of high intensity still visible in part **(f)** is caused by lower T_1 values compared to the surrounding tissue, since the intensity in the ring is still lower than that of normal appearing white matter (NAWM).

2.5.4 Bloch McConnell fit

The numerical model described in Section 2.3.1 can be adjusted to include any number of pools, and can provide an estimate of the magnetization, M_Z, for any off-resonance frequency selected. If this model can be incorporated in a fitting procedure that simulates the saturation and imaging parts of an MT experiment, then full *z-spectra* can be fitted for estimation of multiple parameters. These parameters can include saturation power, T_1 and T_2 of each pool, exchange rate between the pools and relative proton concentrations of each pool with respect to free water.

This approach is indeed feasible but computationally expensive, as complexity and computation time increase with the number of fitted parameters. If all parameters of 5 pools are to be fitted, then 21 parameters need to be varied. In reality the computation time of such a fit would be unreasonable, so some parameters have to be fixed. Parameters like saturation power (B_1) and the T_1 of the free water pool can easily be measured experimentally, and are therefore not included in the fit. For the rest, if proton pool concentrations are the parameters of interest, exchange rates and T_2s can be set to values found in literature.

For an even lower computational cost, our recent paper[4] proposes a method where acquired spectra can be compared to a database, or Look Up Table (LUT) of simulated spectra created based on the model above. The database includes information on B_1 and water T_1 and limits the fit to proton pool concentrations only. The LUT search is done by brute force least squares fitting, and is explained in detail in Chapter 4.

2.6 Summary

This chapter has introduced the mechanisms of MT and CEST, and the concept of z-spectroscopy. The effects of B_0 and B_1 are discussed, imaging sequences are outlined and the mathematical model that describes the exchange of magnetization between different proton pools is described. The chapter ends with a review on current and novel quantification methods, from basic asymmetry analysis to complex B_1 and T_1 corrected Lorentzian fitting, and finally our own method presented in Chapter 4 of this thesis.

Bibliography

[1] Kimberly L. Desmond, Firas Moosvi, and Greg J. Stanisz. Mapping of amide, amine, and aliphatic peaks in the CEST spectra of murine xenografts at 7 T. *Magnetic Resonance in Medicine*, 71(5):1841–1853, 2014.

[2] Allen D Elster. www.mriquestions.com, 2016.

[3] S Forsén and RA Hoffman. Study of Moderatly Rapid Chamical Exchange Reactions by Means of Nuclear Magnetic Double Resonance. *The Journal of Chemical Physics*, 2892(11):2892–2901, 1963.

[4] Nicolas Geades, Benjamin A. E. Hunt, Simon M. Shah, Andrew Peters, Olivier E. Mougin, and Penny A. Gowland. Quantitative analysis of the z-spectrum using a numerically simulated look-up table: Application to the healthy human brain at 7T. *Magnetic Resonance in Medicine*, oct 2016.

[5] V Guivel-Scharen, T Sinnwell, S D Wolff, and R S Balaban. Detection of proton chemical exchange between metabolites and water in biological tissues. *Journal of Magnetic Resonance*, 133(1):36–45, 1998.

[6] R M Henkelman, X Huang, Q S Xiang, G J Stanisz, S D Swanson, and M J Bronskill. Quantitative interpretation of magnetization transfer. *Magn Reson Med*, 29(6):759–766, 1993.

[7] R. M. Henkelman, G. J. Stanisz, and S. J. Graham. Magnetization transfer in MRI: A review. *NMR in Biomedicine*, 14(2):57–64, 2001.

[8] Jun Hua, Craig K. Jones, Jaishri Blakeley, Seth A. Smith, Peter C M Van Zijl, and Jinyuan Zhou. Quantitative description of the asymmetry in magnetization transfer effects around the water resonance in the human brain. *Magnetic Resonance in Medicine*, 58(4):786–793, 2007.

[9] Tao Jin and Seong-Gi Kim. In-vivo saturation transfer imaging of nuclear overhauser effectfrom aromatic and aliphatic protons: implication to APT quantification. In *ISMRM*, page pp2528, 2013.

[10] Tao Jin, Ping Wang, Xiaopeng Zong, and Seong Gi Kim. Magnetic resonance imaging of the Amine-Proton EXchange (APEX) dependent contrast. *NeuroImage*, 59(2):1218–1227, 2012.

[11] Tao Jin, Ping Wang, Xiaopeng Zong, and Seong-Gi Kim. MR imaging of the amide-proton transfer effect and the pH-insensitive nuclear overhauser effect at 9.4 T. *Magnetic Resonance in Medicine*, 69(3):760–770, mar 2013.

[12] Craig K. Jones, Alan Huang, Jiadi Xu, Richard A E Edden, Michael Schar, Jun Hua, Nikita Oskolkov, Domenico Zaca, Jinyuan Zhou, Michael T. McMahon, Jay J. Pillai, and Peter C M van Zijl. Nuclear Overhauser enhancement (NOE) imaging in the human brain at 7T. *NeuroImage*, 77: 114–124, 2013.

[13] Vitaliy Khlebnikov, Nicolas Geades, Dennis W. J. Klomp, Hans Hoogduin, Penny Gowland, and Olivier Mougin. Comparison of pulsed three-dimensional CEST acquisition schemes at 7 tesla: steady state versus pseudosteady state. *Magnetic Resonance in Medicine*, jul 2016.

[14] Mina Kim, Joseph Gillen, Bennett A. Landman, Jinyuan Zhou, and Peter C M Van Zijl. Water saturation shift referencing (WASSR) for chemical exchange saturation transfer (CEST) experiments. *Magnetic Resonance in Medicine*, 61(6):1441–1450, 2009.

[15] S H Koenig. Classes of hydration sites at protein-water interfaces: the source of contrast in magnetic resonance imaging. *Biophysical journal*, 69(2):593–603, 1995.

[16] Ives R. Levesque, Paul S. Giacomini, Sridar Narayanan, Luciana T. Ribeiro, John G. Sled, Doug L. Arnold, and G. Bruce Pike. Quantitative magnetization transfer and myelin water imaging of the evolution of acute multiple sclerosis lesions. *Magnetic Resonance in Medicine*, 63:633–640, 2010.

[17] Wen Ling, Ravinder R Regatte, Gil Navon, and Alexej Jerschow. Assessment of glycosaminoglycan concentration in vivo by chemical exchange-dependent

saturation transfer (gagCEST). *Proceedings of the National Academy of Sciences of the United States of America*, 105(7):2266–2270, 2008.

[18] Harden M. McConnell. Reaction Rates by Nuclear Magnetic Resonance. *The Journal of Chemical Physics*, 28(3):430, 1958.

[19] Clare Morrison and R. Mark Henkelman. A Model for Magnetization Transfer in Tissues. *Magnetic Resonance in Medicine*, 33(4):475–482, apr 1995.

[20] O E Mougin, R C Coxon, A Pitiot, and Penny A. Gowland. Magnetization transfer phenomenon in the human brain at 7 T. *NeuroImage*, 49(1):272–81, 2010.

[21] Olivier Mougin, Matthew Clemence, Andrew Peters, Alain Pitiot, and Penny Gowland. High-resolution imaging of magnetisation transfer and nuclear Overhauser effect in the human visual cortex at 7 T. *NMR in Biomedicine*, 26(11):1508–1517, 2013.

[22] S W Provencher. Estimation of metabolite concentrations from localized in vivo proton NMR spectra. *Magnetic resonance in medicine : official journal of the Society of Magnetic Resonance in Medicine / Society of Magnetic Resonance in Medicine*, 30(6):672–9, 1993.

[23] Stefan Ropele, Massimo Filippi, Paola Valsasina, Tijmen Korteweg, Frederik Barkhof, Paul S. Tofts, Rebecca Samson, David H. Miller, and Franz Fazekas. Assessment and correction of B1-induced errors in magnetization transfer ratio measurements. *Magnetic Resonance in Medicine*, 53(1):134–140, 2005.

[24] Rebecca S. Samson, Claudia A M Wheeler-Kingshott, Mark R. Symms, Daniel J. Tozer, and Paul S. Tofts. A simple correction for B1 field errors in magnetization transfer ratio measurements. *Magnetic Resonance Imaging*, 24(3):255–263, 2006.

[25] Benjamin Schmitt, Moritz Zaiß, Jinyuan Zhou, and Peter Bachert. Optimization of pulse train presaturation for CEST imaging in clinical scanners. *Magnetic Resonance in Medicine*, 65(6):1620–1629, 2011.

[26] J G Sled and G B Pike. Quantitative imaging of magnetization transfer exchange and relaxation properties in vivo using MRI. *Magnetic resonance in medicine*, 46(5):923–31, nov 2001.

[27] Greg J. Stanisz, Ewa E. Odrobina, Joseph Pun, Michael Escaravage, Simon J. Graham, Michael J. Bronskill, and R. Mark Henkelman. T1, T2 relaxation and magnetization transfer in tissue at 3T. *Magnetic Resonance in Medicine*, 54(3):507–512, 2005.

[28] Phillip Zhe Sun, Thomas Benner, Ashok Kumar, and A. Gregory Sorensen. Investigation of optimizing and translating pH-sensitive pulsed-chemical exchange saturation transfer (CEST) imaging to a 3T clinical scanner. *Magnetic Resonance in Medicine*, 60(4):834–841, 2008.

[29] I Tkác, P Andersen, G Adriany, H Merkle, K Ugurbil, and R Gruetter. In vivo 1H NMR spectroscopy of the human brain at 7 T. *Magnetic resonance in medicine : official journal of the Society of Magnetic Resonance in Medicine / Society of Magnetic Resonance in Medicine*, 46(3):451–6, 2001.

[30] Ivan Tkác, Gülin Oz, Gregor Adriany, Kamil Uğurbil, and Rolf Gruetter. In vivo 1H NMR spectroscopy of the human brain at high magnetic fields: metabolite quantification at 4T vs. 7T. *Magnetic resonance in medicine : official journal of the Society of Magnetic Resonance in Medicine / Society of Magnetic Resonance in Medicine*, 62(4):868–79, 2009.

[31] B. L. van de Bank, U. E. Emir, V. O. Boer, J. J. a. van Asten, M. C. Maas, J. P. Wijnen, H. E. Kan, G. Oz, D. W. J. Klomp, and T. W. J. Scheenen. Multi-center reproducibility of neurochemical profiles in the human brain at 7T. *NMR in Biomedicine*, 28(3):306–316, 2015.

[32] Peter C M van Zijl and Nirbhay N Yadav. Chemical exchange saturation transfer (CEST): What is in a name and what isn't? *Magnetic Resonance in Medicine*, 65(4):927–948, apr 2011.

[33] Peter C M Van Zijl, Jinyuan Zhou, Noriko Mori, Jean Francois Payen, David Wilson, and Susumu Mori. Mechanism of magnetization transfer during on-resonance water saturation. A new approach to detect mobile proteins, peptides, and lipids. *Magnetic Resonance in Medicine*, 49(3):440–449, 2003.

[34] Gopal Varma, Guillaume Duhamel, Cedric De Bazelaire, and David C. Alsop. Magnetization transfer from inhomogeneously broadened lines: A potential marker for myelin. *Magnetic Resonance in Medicine*, 73(2):614–622, 2015.

[35] Neil E. Wilson, Kevin D'Aquilla, Catherine Debrosse, Hari Hariharan, and Ravinder Reddy. Localized, gradient-reversed ultrafast z-spectroscopy in vivo at 7T. *Magnetic Resonance in Medicine*, 00:1–8, 2016.

[36] Johannes Windschuh, Moritz Zaiss, Jan Eric Meissner, Daniel Paech, Alexander Radbruch, Mark E. Ladd, and Peter Bachert. Correction of B1-inhomogeneities for relaxation-compensated CEST imaging at 7T. *NMR in Biomedicine*, 28(5):529–537, 2015.

[37] Donald E. Woessner. Brownian motion and its effects in NMR chemical exchange and relaxation in liquids. *Concepts in Magnetic Resonance*, 8(6):397–421, 1996.

[38] Donald E. Woessner, Shanrong Zhang, Matthew E. Merritt, and A. Dean Sherry. Numerical solution of the Bloch equations provides insights into the optimum design of PARACEST agents for MRI. *Magnetic Resonance in Medicine*, 53(4):790–799, 2005.

[39] S D Wolff and R S Balaban. Magnetization transfer contrast (MTC) and tissue water proton relaxation in vivo. *Magnetic Resonance in Medicine*, 10 (1):135–144, 1989.

[40] Nirbhay N. Yadav, Craig K. Jones, Jiadi Xu, Amnon Bar-Shir, Assaf A. Gilad, Michael T. McMahon, and Peter C M Van Zijl. Detection of rapidly exchanging compounds using on-resonance frequency-labeled exchange (FLEX) transfer. *Magnetic Resonance in Medicine*, 68(4):1048–1055, 2012.

[41] Moritz Zaiss and Peter Bachert. Chemical exchange saturation transfer (CEST) and MR Z-spectroscopy in vivo: a review of theoretical approaches and methods. *Physics in medicine and biology*, 58(22):R221–69, 2013.

[42] Moritz Zaiss, Benjamin Schmitt, and Peter Bachert. Quantitative separation of CEST effect from magnetization transfer and spillover effects by Lorentzian-line-fit analysis of z-spectra. *Journal of Magnetic Resonance*, 211 (2):149–155, 2011.

[43] Moritz Zaiss, Junzhong Xu, Steffen Goerke, Imad S. Khan, Robert J. Singer, John C. Gore, Daniel F. Gochberg, and Peter Bachert. Inverse Z-spectrum analysis for spillover-, MT-, and T1-corrected steady-state pulsed CEST-MRI - application to pH-weighted MRI of acute stroke. *NMR in Biomedicine*, 27(3):240–252, 2014.

[44] Jinyuan Zhou, Bachchu Lal, David A. Wilson, John Laterra, and Peter C M Van Zijl. Amide Proton Transfer (APT) Contrast for Imaging of Brain Tumors. *Magnetic Resonance in Medicine*, 50(6):1120–1126, 2003.

[45] Jinyuan Zhou, Jean-Francois Payen, David A Wilson, Richard J Traystman, and Peter C M van Zijl. Using the amide proton signals of intracellular proteins and peptides to detect pH effects in MRI. *Nature medicine*, 9(8): 1085–90, aug 2003.

Chapter 3

Macromolecules in the human brain

3.1 Introduction

As discussed previously, magnetization transfer experiments study the transfer of macromolecule-associated saturation to free water, where it can be imaged and quantified. The interest in macromolecules comes from the strong correlation with myelin content, making the modality a potental marker of myelination for neurological disorders such as Multiple Sclerosis (MS). In fact, MT has been extensively used in MS to observe demyelination via the loss of signal coming from myelin and other macromolecules[18,28], while proton (^1H) Magnetic Resonance Spectroscopy (MRS) has enabled the study of specific biochemical aspects of the human brain in great detail. The importance of these methods lies in the non-invasive detection of metabolite concentrations, giving the possibility to track changes in metabolite concentration that relate strongly with brain diseases like tumours and neurodegeneration.

The human brain is composed of around 80% water, while the remainder consists of multiple complex molecules, like proteins and lipids. The main cell in the human brain is the neuron, made up of the body of the cell, or soma, containing the nucleus, dendrites connecting each neuron to surrounding neuron cells, the axon, a fine cable-like projection that extends to other neurons, and the axon terminal containing synapses for communication with the other neurons. The axon is surrounded by a fatty, insulating material called the myelin sheath, which is part of a separate glial cell, the oligodendrocyte. The purpose of this insulating material is to aid the transmission of electrical signal along the axon.

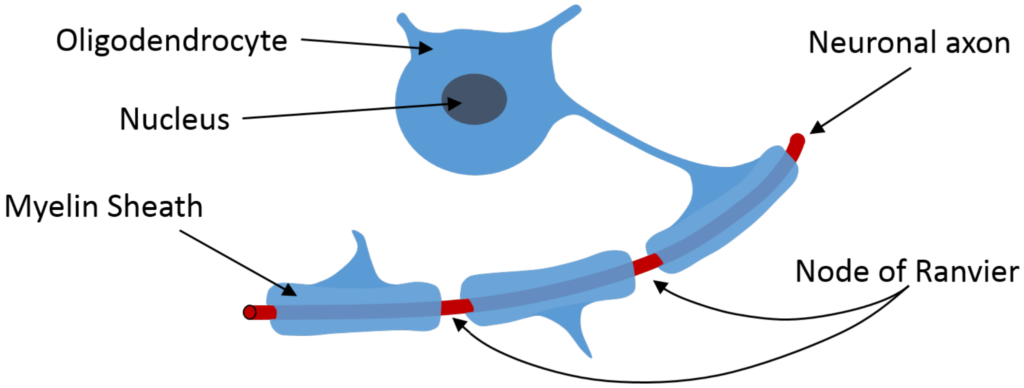

Figure 3.1: Schematic of myelin sheath surrounding the axon of a nerve fibre, and the oligodendrocyte providing the myelin sheath. The myelin sheath is an extension of the plasma membrane of the oligodendrocyte, and is wrapped around the axon up to 100 times.

The oligodendrocyte can provide myelination for 40 or more different axons[7,32], but for only one section of any given axon[32] (see Figure 3.1). One layer of myelin sheath measures approximately 16-18nm in width, but one axon can have up to 100 layers wrapped around its body. The main component of white matter is therefore myelin, which is essential for the normal function of nerve fibres and the brain as a whole. Myelin accounts for about 50% of the total weight of the white matter, the volume being determined by the number of axons, their calibre and the thickness of the myelin sheath[32].

Examining the surface of the myelin sheath in more detail reveals that the membrane is formed by a series of lipid bilayers (the lipids elements being phospholipids, glycolipids and cholesterol) and proteins attached to, or suspended in the lipid bilayer. The myelin sheath is a multi-layer membrane, very tightly wound around nerve axons, causing the movement of water molecules as well as the tumbling of other molecules and proteins on the surface of the myelin sheath to dramatically slow down. This suggests that while the human brain white matter (dry weight) is composed of about 55% lipids and 40% protein[32], the MT signal observed in z-spectroscopy is linked to macromolecules bound to myelin. Additionally, histology experiments indicate that MT effects in the white matter can be linked to myelin quantity[22,30].

3.2 Macromolecules in z-spectroscopy

3.2.1 Introduction

The signal from macromolecules (MM) in z-spectroscopy (usually termed the semi-solid or MT effect) is observed as a very wide Super-Lorentzian lineshape, spanning across a bandwidth of multiple kilohertz relative to water, depending on saturation power. MT is usually an unwanted effect in z-spectroscopy and is fitted so that it can be removed from CEST effects (just like the macromolecular spectrum in conventional proton spectroscopy), but has proven very useful when studying demyelinating disease. In *in-vivo* spectra, the MT effect is seen as a very wide peak centred at around -2.4ppm (see Figure 3.2b), observable together with NOE and CEST effects. Unlike NOE and CEST effects, the MT effect can be studied alone by acquiring a *z-spectrum* at frequencies far off-resonance to water (Figure 3.2a). The aim of this chapter is to investigate the distribution of MM signal across the brain, focusing on the lineshape T_2^b, using two different estimation methodologies.

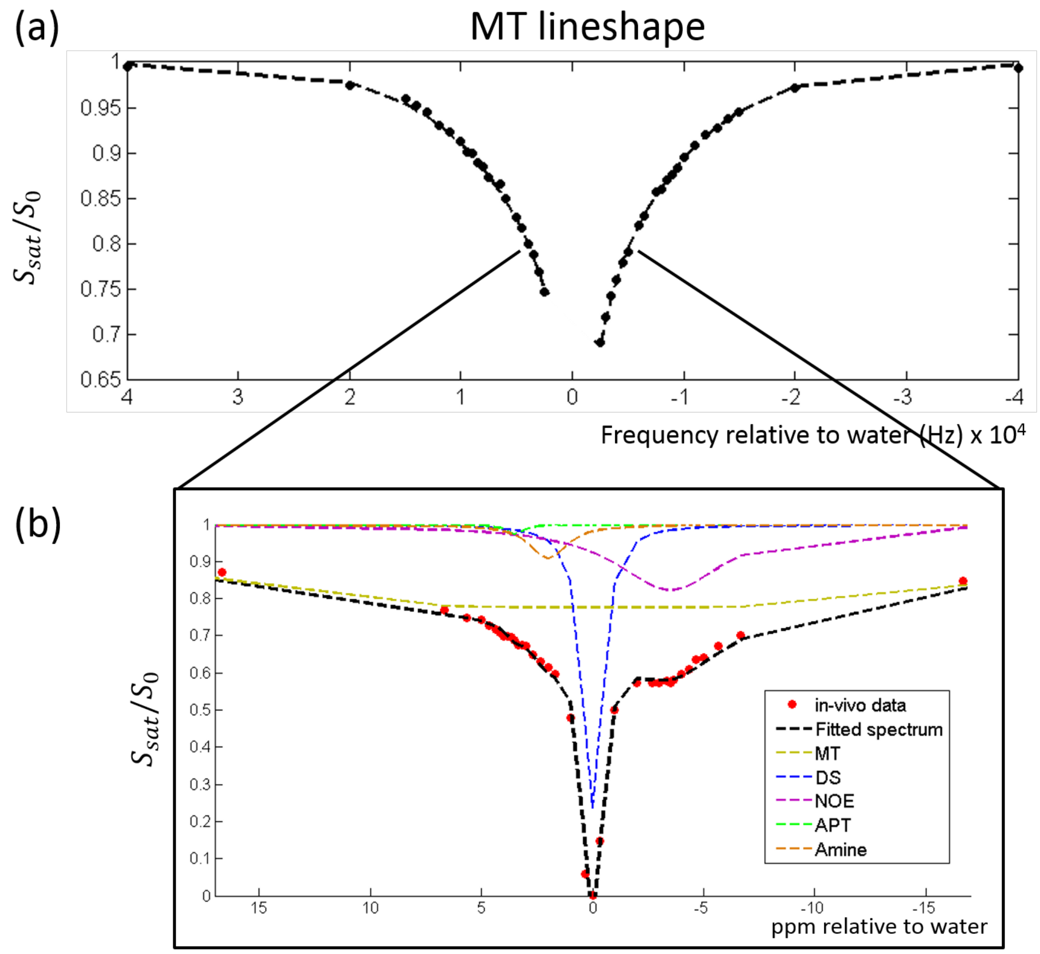

Figure 3.2: (a) A *z-spectrum* in the range of -40kHz to 40kHz, excluding the frequencies between -2500Hz to 2500Hz where NOE and CEST effects are observed (*in-vivo* data). Note the asymmetry of the spectrum, centered at around -650Hz. (b) A Lorentzian lineshape fitted *z-spectrum* in the range of -5kHz to 5kHz showing MT, NOE and CEST effects. Corpus Callosum ROI.

3.2.2 Methods

By acquiring spectra at high power and far off-resonance to water as in Figure 3.2a, the semi-solid MT effect can be observed with minimal interference from NOE and CEST effects. A study was designed to observe the MT lineshape across the brain, looking at the frequency offset centre of the effect, the width (or T_2) of the lineshape and the effect of B_1 power on the spectrum. Two methods were used to evaluate the lineshape: first, a simple model of fitting a single Super-Lorentzian lineshape to the spectra, and second, by fitting the spectra with a multi-pool Bloch McConnell model.

Spectra were acquired on a 7T (Philips Achieva) scanner with a 32-channel receive coil, at two B_1 saturation powers ($0.75\mu T$ and $1.25\mu T B_{1,RMS}$, saturation train of 20 Gaussian-windowed sinc pulses, 30ms in duration (BW = 200Hz) and spaced 30ms apart for a 50% duty cycle), the spectrum being symmetrically sampled at -40000, -20000, -15000, -14000, -13000, -12000, -11000, -10000, -9500, -9000, -8500, -8000, -7500, -6500, -6000, -5000, -4500, -4000, -3500, -3000, -2500, 2500, 3000, 3500, 4000, 4500, 5000, 6000, 6500, 7500, 8000, 8500, 9000, 9500, 10000, 11000, 12000, 13000, 14000, 15000, 20000 and 40000 Hz relative to water. A B_0 map was acquired to monitor variation in the static field but was not used for B_0 correction because the direct saturation water peak was not sampled. The variation in B_0 within the whole scanned volume did not exceed 100Hz (0.33ppm), and in the averaged ROI spectra shown it was below 10Hz. Only one subject was scanned, 30 years old, but was scanned twice to assess repeatability.

Super-Lorentzial lineshape fit

Characterization of the MT lineshape has been previously attempted with various different lineshapes, including Lorentzian, Gaussian and Super-Lorentzian shapes[21]. The Gaussian lineshape is considered most appropriate for dipolar interactions in a rigid system, while the Lorentzian lineshape describes mobile liquid systems best. In the case of partially ordered materials, like semi-solids, both our work and previous research has shown that the Super-Lorentzian shape, which includes an integration over all possible dipolar orientations in the semi-solid material, fits the MT effect best[21,33]. The Super-Lorentzian shape is the absorption lineshape of the MT effect, and to get an estimate of the pool T_2, a full model fit taking account of the lineshape is necessary. Nevertheless, fitting the lineshape alone can give an approximation of the proton pool T_2. The Super-Lorentzian (SL) lineshape is defined as

$$SL(2\pi\Delta) = A\int_0^{\frac{\pi}{2}} d\theta sin\theta\sqrt{\frac{2}{\pi}}\frac{T_2^b}{|3\cos^2\theta - 1|}e^{-2\left(\frac{2\pi\Delta T_2^b}{|3\cos^2\theta-1|}\right)^2}, \tag{3.1}$$

where θ is the dipole orientation angle with respect to the external magnetic field, A is the amplitude of the function and Δ is the frequency shift. The SL function was fitted to acquired spectra using non-linear least squares curve fitting (***lsqcurvefit*** function in Matlab), by fitting for T_2^b, frequency offset, Δ, and amplitude, A of the function. An example of the fit is shown in Figure 3.3. The Super-Lorentzian lineshape fit was also compared to a Lorentzian fit and also a Gaussian fit, to assess whether this shape was indeed more appropriate for characterizing the MT effect.

Various datapoints were collected throughout the scan to evaluate and correct for any signal drift caused by heating of the RF and gradient coils that introduces variation in B_1 and F_0. These datapoints were always collected at a frequency offset to water of 50kHz, and to keep the scan time short, in the data shown here, only three signal drift datapoints were collected; one at the beginning of the scan (also used for *z-spectra* normalization), one in the middle of the scan (just before the water frequency) and one at the end. A linear function was fitted to the three points, giving datapoints at each frequency in the *z-spectra.* The acquired *z-spectra* were then normalized by the signal drift signal. The result of this signal drift correction is shown in Figure 3.5.

Numerical Bloch McConnell fit

The model described in Section 2.3.1 of this report can be used to estimate the bound pool T_2. Using the far off-resonance data that excludes any frequencies near water, where NOE and CEST are observed, the numerical Bloch McConnell model can be used to simulate the effects of parameter values in the spectra.

The acquired spectra (same as in Section 3.2.1), ranging from -40kHz to 40kHz and excluding the range between -2500Hz to 2500Hz, should have minimal contributions from other proton pools (like NOE and CEST) so a two pool model was fitted (water, MT). The fit was performed on small ROIs in the Corpus Callosum and the relative B_1 of the ROI was taken from a separately acquired B_1 map. T_1 was assumed to be 1.2s and exchange rates were fixed at 50Hz and 10Hz for the MT and NOE pools respectively. The parameters left to vary were the concentration, T_2 relaxation and frequency offset of the MT pool.

3.2.3 Results

Super-Lorentzian lineshape fit

The example fit in Figure 3.3 shows that the lineshape fitting model fitted the data with very low residuals, providing estimations of T_2 and frequency shift. Figure 3.4 shows that the Super-Lorentzian shape gives the best fit, but in the range of -10kHz to 10kHz the simpler Lorentzian shape describes the lineshape adequately (low residuals). This is important as it shows that when fitting spectra using a multi-pool Lorentzian model to estimate NOE and CEST parameters, and frequency sampling is within ±10kHz, the MT can be fitted as a Lorentzian shape too.

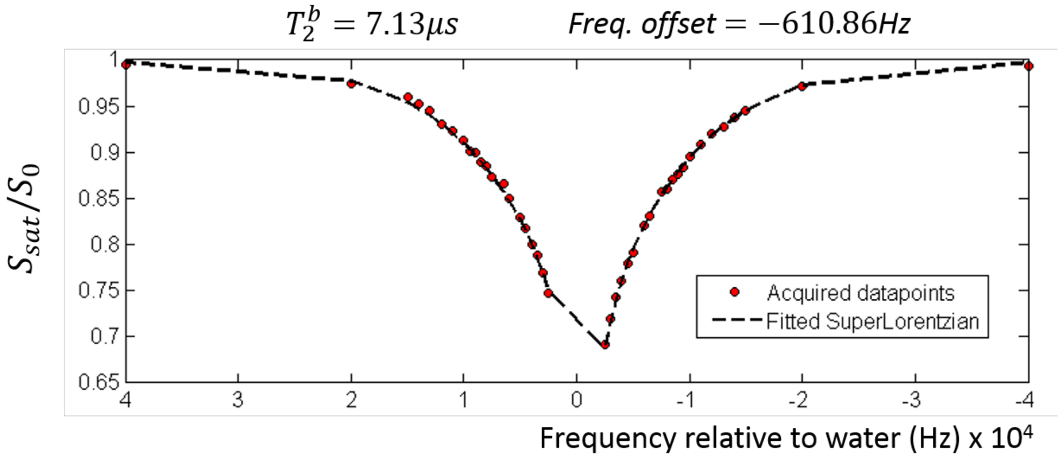

Figure 3.3: Super-Lorentzian function from Equation 3.1 (dotted line) fitted to an averaged *in-vivo* white matter spectrum (red dots). The T_2^b and offset frequency values are shown in the title of the plot.

Signal drift correction is shown in figure 3.5. This has the potential to alter T_2^b estimations, and an alternative method to eliminate the effect is by sampling the

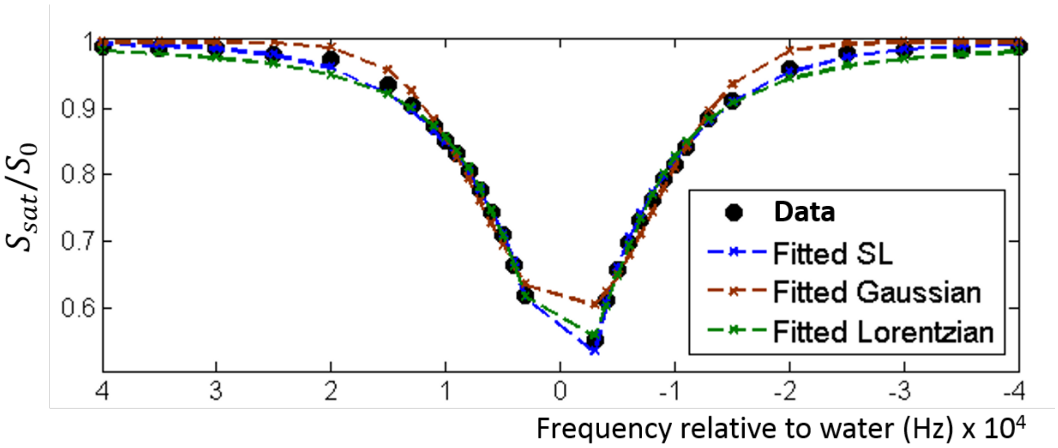

Figure 3.4: MT data fitted with Super-Lorentzian, Lorentzian and Gaussian functions. The full spectrum residuals were 0.0013, 0.0025 and 0.01 respectively.

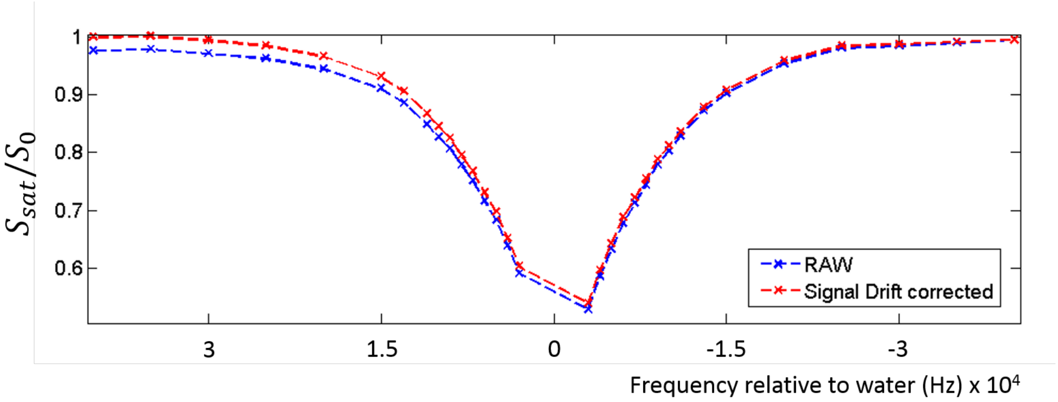

Figure 3.5: Signal drift correction of an acquired MT spectrum. Note that the spectrum is sampled from negative to positive frequencies, hence the greater drift in positive frequency datapoints.

spectrum in a pseudo-random way, or sample the spectrum inside out, but if the scan is longer than around 7 minutes signal drift correction is still advisable.

An example of a single slice fit using the Super-Lorentzian lineshape method is shown in Figure 3.6. Figure 3.6(c and f) show a shift of the MT lineshape by about -500Hz to -650Hz relative to water(note that there is an uncertainty of about 100Hz due to the lack of B_0 correction), in line with previous observations, and a CSF contrast is also apparent. While the model fits the data with low residuals, it is sensitive to B_1 power. This can be seen in Figure 3.6(a) where the estimated T_2 is shorter in areas of high B_1 (blue arrow). Parts a-c in Figure 3.6 are from a single power spectrum at 1.25μT B_1, and parts d-f show the results after B_1 correction has been applied, interpolating the spectra to a target B_1 of 1μT. The spectra in parts d-f have also been corrected for signal drift.

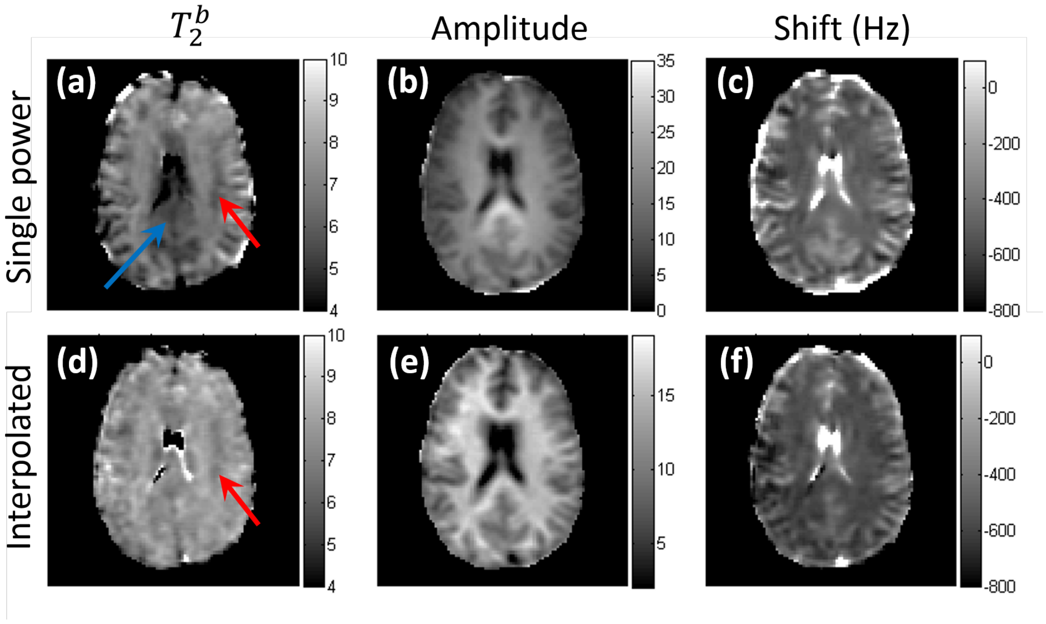

Figure 3.6: Maps of (a,d) fitted T_2 of the Super-Lorentzian model from equation 3.1, (b,e) fitted amplitude of the model and (c,f) fitted shift in Hz. Note the red arrows in part (a) and (d), showing shorter T_2 values in certail areas (possibly related to fibre orientation), and the blue arrow showing shorter T_2 values in areas of high B_1 saturation power or Super-Lorentzian amplitude (which disappears after B_1 correction). The spectra in (d-f) have been corrected for signal drift.

The sensitivity to B_1 can also be seen in the fit of the same ROI acquired at two different B_1 saturation powers. Figure 3.7 shows how the same ROI from two separately acquired datasets (at two different B_1 saturation powers) results in different T_2^b values.

This sensitivity of the Super-Lorentzian T_2^b to B_1 saturation power, together with the fact that this simple model ignores any other proton pools, limits the use of the lineshape fitting method to characterize the bound pool, but it gives a good starting point for a finer search. If a Lorentzian fitting method is employed, then the MT lineshape can be described as a Super-Lorentzian with a T_2^b of around

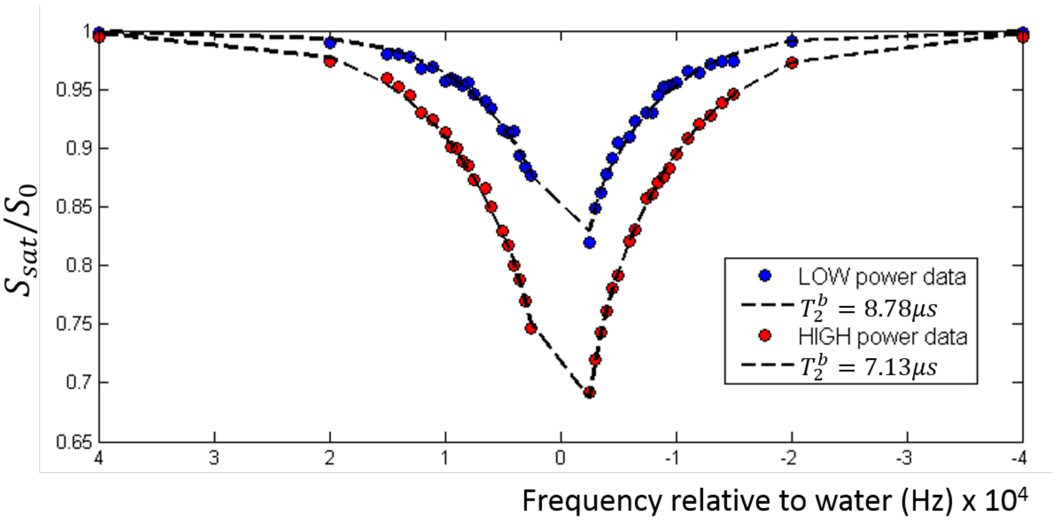

Figure 3.7: Fitting two B_1 saturation powers separately. Fitting the low power data (blue) gives a longer T_2^b value of $8.78\mu m$, compared to $7.13\mu m$ for the exact same ROI in a higher power dataset (red).

$8\mu s$. Alternatively, Figure 3.4 shows that a Lorentzian shape can adequately fit the MT effect, if the sampling frequencies are within ±10kHz. In the work presented in this thesis, where *z-spectra* are simulated numerically and matched to acquired spectra, a different method must be used to estimate T_2^b.

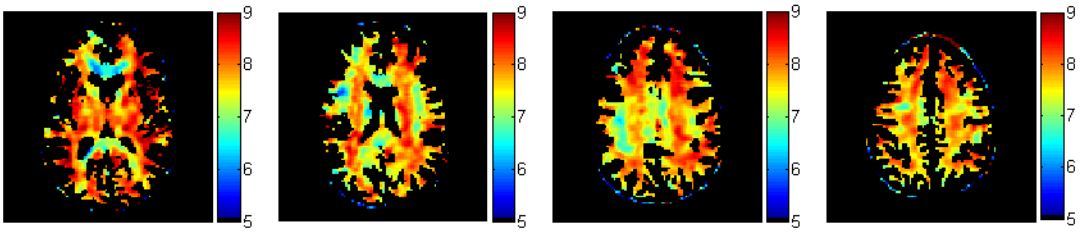

Figure 3.8: T_2^b variation in the WM, at 4 different slices in the brain from bottom (left) to top. Colour scale shows fitted T_2^b. Note how longer T_2^b is fitted where fibre orientation is known to be parallel to B_0, and shorter T_2^b is fitted in the corpus callosum.

The B_1 corrected data in Figure 3.6 were used to create maps of T_2^b in a large 3D volume, to assess the variation of fitted T_2^b in the WM, and whether it relates to fibre orientation as previously observed by Pampel *et. al.*[24]. The results are shown in Figure 3.8, which shows variation that is very similar to that shown by Pampel *et. al.*, but no fibre orientation data were acquired in this study.

Numerical Bloch McConnell fit

Figure 3.9 shows the result of the numerical Bloch McConnell fit, with a bound pool T_2^b of about $14.5\mu s$.

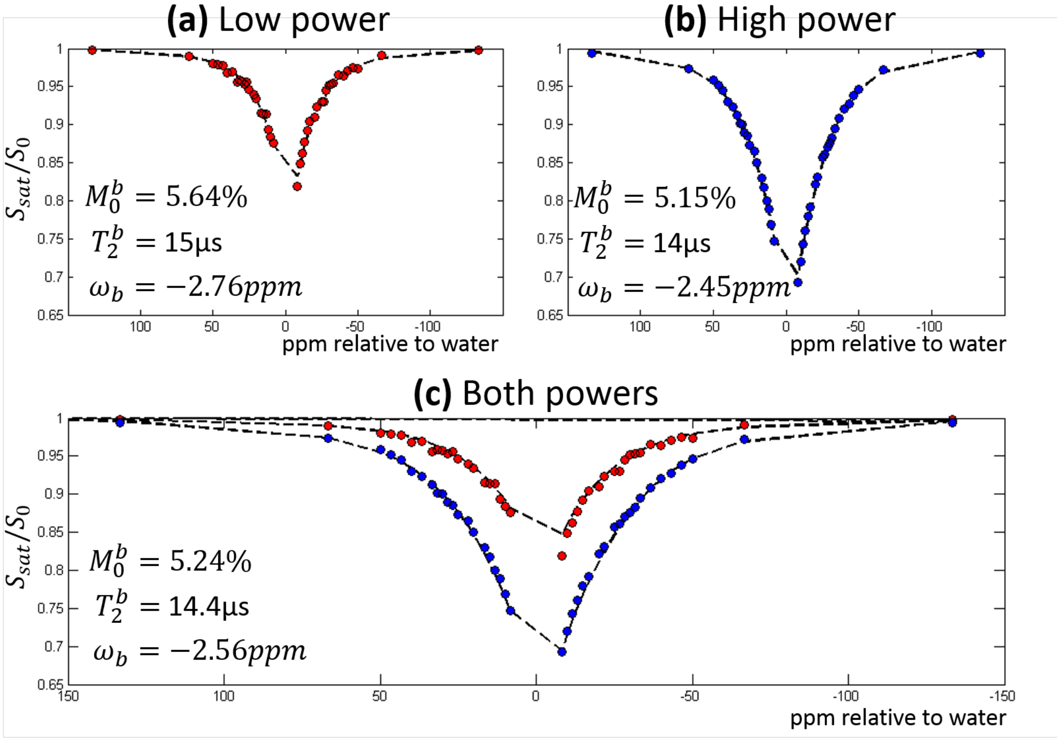

Figure 3.9: Two pool numerical fit to MT spectra. The result of the fit is shown for **(a)** Low and **(b)** High B_1 saturation power spectra. **(c)** shows the two powers fitted together. The estimation of T_2^b remains similar in all three cases.

Figure 3.9 shows the results of performing the fit on the spectra acquired at the two B_1 saturation powers individually, and together. Unlike the previous method of fitting for the absorption lineshape alone, this method can estimate T_2^b values independent of B_1 saturation used, with very small variations of MT proton pool concentration and frequency offset shifts observed. A fit including the NOE pool at -3.5 ppm (fitting for concentration and T_2) was also attempted but no significant change in the estimation of T_2^b was observed.

3.2.4 Discussion

An inconsistency exists in the T_2^b values estimated using the two different methods. Using the first method (SL lineshape fit) produces a fit with comparable residuals to the full fit, but is simplistic in its application and ignores multiple parameters of the magnetization transfer experiment. The SL lineshape fit is allowed to vary in amplitude, width and frequency shift. These parameters relate to relative concentration of the proton pool, exchange rate with water, T_2^b and chemical shift, but B_1 saturation power, water T_1, other proton pools, saturation pulse shape, number of pulses, duty cycle, readout scheme and multiple other variables are ignored.

The Bloch McConnell fit takes account of all these parameters, albeit with some assumptions, giving more precise results. The main variables that have the strongest effect on the resulting T_2^b are B_1 saturation power and water T_1, which can be estimated and included in the full fit, but the relative concentration of the MT protons, their longitudinal relaxation time and their exchange rate with water are unknown, potentially introducing a small uncertainty to the estimation of T_2^b.

Both methods of characterizing the MT effect discussed above have advantages and limitations, and both give an insight into the properties of macromolecules. In semi-quantitative methods like Lorentzian fitting or Lorentzian difference, the first method is useful. When it comes to attempting fully quantitative methods like the full fit explained in Chapter 2, more accurate estimation of T_2^b is required. The macromolecular signal in z-spectroscopy can be very effectively studied with high sensitivity, using these two methods, but the source of signal is difficult to probe. The following part of this chapter aims to investigate the individual molecules providing the signal, with specificity unavailable in z-spectroscopy.

3.3 Macromolecules in proton (^1H) spectroscopic imaging

3.3.1 Introduction

The abundance of protons in tissue in the human brain allows for high sensitivity quantification of metabolites, especially at high field (7T) where up to 20 metabolites have been quantified using single voxel ^1H spectroscopy[34,35,37]. Additionally, approximately 10 broad resonances arise from large molecules in the brain like proteins and peptides made up of amino acids like leucine, isoleucine, valine, threonine, alanine, lysine, arginine, glutamate and glutamine[4]. Macromolecular signal is of particular importance as significant changes in the intensity of the signal between 0.5ppm and 2ppm have been observed in stroke[13], Multiple Sclerosis (MS)[23,26,31] and tumors[10]. Because these macromolecules overlap with metabolite resonances it is important to characterize the signal of these macromolecules across the brain. This enables more accurate quantification of metabolites on one hand, and may reveal a potential new marker of neuro-degeneration. This section is specifically focused on investigating regional, spectral and relaxation differences of macromolecules (MM) in the human brain.

High field Magnetic Resonance Spectroscopic Imaging (MRSI) provides various advantages like increased SNR, which leads to higher spatial resolution and increased spectral resolution in the form of increased chemical shift dispersion between metabolite resonances. High field also introduces problems like increased B_1 and B_0 field inhomogeneity across the brain, increased Chemical Shift Displacement Errors (CSDE) and shortened T_2 relaxation times. While the increased signal loss due to T_2 relaxation can easily be avoided with the use of very short acquisition delays (TE) in pulse acquire MRSI, the lipid suppression in un-localized MRSI is challenging and often results in high SAR deposition due to high RF demand for lipid suppression pulses. B_1 inhomogeneity can be reduced by using multiple channel transmit coils[16], or adiabatic pulses which also reduce the CSDE in case of localized MRSI.

While excellent lipid suppression can be achieved with localization methods such as semi-LASER and Outer Volume Suppression (OVS)[20], it comes at the cost of long TR values (>4000ms at 7 Tesla[12]) due to SAR limitations which result in long measurement times, particularly for high spatial resolutions. Another way to suppress this unwanted lipid signal is with the use of a gradient crusher coil positioned between the head and the head coil[5]. This eliminates the use of any additional RF for lipid suppression, thereby enabling the use of short TR and higher spatial resolution.

MRSI at short TE and short TR allows enhanced detection of macromolecules (MM), particularly at high fields (i.e. 7T). Using high spatial resolution and a crusher coil[5], these MM signals can be observed at short TR and TE in the human brain without contamination of lipid signals. There is a need for better understanding of the relaxation properties of macromolecules, as well as their regional distribution, so in this study we aimed to investigate the relaxation, spectral and regional differences of macromolecular spins in the human brain using T_1 mapping, high resolution MRSI and metabolite nulling with a crusher coil at 7T.

3.3.2 Materials and Methods

Data acquisition

T_1 **mapping of macromolecules:** Experiments were performed on a 7T whole body MR system using a 16-channel RF receiver array in a volume transmit head coil (Nova Medical, USA). The crusher coil (MR Coils, the Netherlands) was inserted into the head coil as previously described[5]. For T_1 mapping of MM a single slice high resolution MRSI was obtained at different flip angles in 8 healthy volunteers (6 male, 2 female, 23-55 years old). The flip angles used were 15°, 30°, 50°, 60°, 70° and 90° with a short TR of 160-190ms. The crusher coil was turned on during acquisition. Other measurement parameters were: TE 2.5ms, matrix size 34 x 38, voxel size 5 x 5 x 10mm^3, scan time: 2:42min. A non-suppressed water reference scan was also recorded for post processing[11]. This part of the study was carried out entirely by Markiska Damen as part of her MSc thesis in Utrecht. The crusher coil used for lipid suppression is shown in Figure 3.10, together with an example image of crushed signal coming from the scalp and skull.

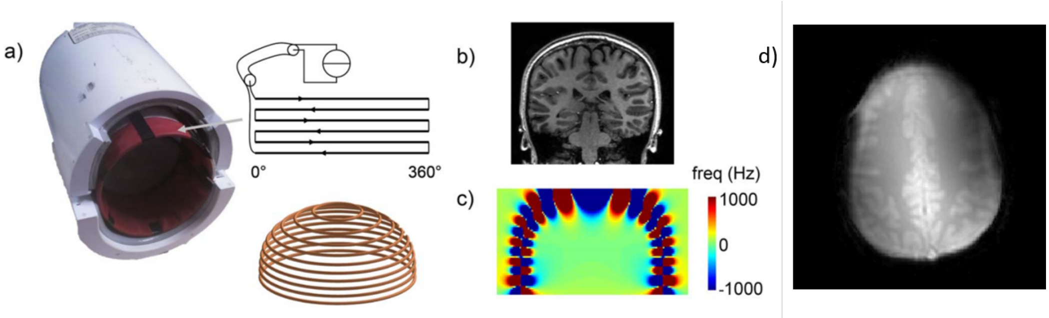

Figure 3.10: Lipid suppression with a crusher coil. Photograph, model and circuitry of the outer volume crusher coil (a), integrated inside a commercially available 16-channel head coil. The thickness of the crusher coil is approximately 5mm. The rods are shaped to enclose the side and top of the head, while the distance between the rods is 10mm, generating a rapidly changing field on the skull (b,c). An example axial image when using the crusher coil is shown in (d).

High resolution MRSI: For the high resolution and metabolite nulled data, five healthy volunteers (3 male, 2 female, 23-36 years old) were scanned. High resolution MRSI datasets were acquired at 7 Tesla using a 32-channel head coil (Nova Medical, USA) and a crusher coil (MR Coils, the Netherlands). A single slice MRSI measurement was performed using the following parameters in a pulse-acquire experiment: TR 300ms, TE 2.5ms , flip angle of 70°, matrix size 40 x 40, voxel size 5 x 5 x 5mm^3, spectral bandwidth of 4000 Hz, sampled at 1024 points, NSA of 2 and water suppression was achieved by using frequency selective spokes pulses[38], for a total acquisition time of 9:04 min. A non-suppressed water reference scan was also recorded for post processing.

Metabolite-nulled MRSI: A difference in measured T_1 relaxation time between macromolecules and metabolites in the human brain allows nulling of selected metabolites using an inversion pulse[4]. Metabolite nulled MRSI data were acquired with a Double Inversion Recovery (DIR) experiment, with inversion times for metabolite nulling as proposed by Považan *et. al.* in[27]. VAPOR water suppression[34] was used. The following scan parameters were used: TR 1000ms, TE 2.5ms, excitation flip angle 90°, TI1 870ms, TI2 296ms, matrix size 18 x 18, voxel size 15 x 15 x 10mm^3, spectral bandwidth of 6000Hz, sampled at 512 points, NSA of 4, for a total acquisition time of 9:53min. For inversion, an adiabatic full passage pulse was used with duration of 25ms and 98% inversion bandwidth of 2.2kHz, centered at 0.5ppm. In all experiments a separate non-water-suppressed acquisition at lower (half the matrix size) resolution and one average was acquired for eddy current correction and residual water removal.

Data processing

T_1 **mapping:** The spectra were processed using NMR Wizard[8], an algorithm based on a linear combination of metabolite peaks implemented in MATLAB[17]. The water residual signal in the metabolite data was removed by fitting and subtracting the non-suppressed water reference scan from the metabolite data[19]. Hankel Lanczos Singular Value Decomposition (HLSVD) filtering[25] was also used to remove any remaining residual water signal. The spectra from all voxels were fitted without a baseline correction. Simulated basis sets of creatine, glutamate, glutamine, glutathione, choline, myo-inositol, NAA, NAAG and a single measured macromolecular baseline (based on inversion recovery T_1 nulling) were included in the fitting. Automatic phasing of the spectra was implemented by maximizing the largest peak in the spectrum with the optimum phase. Furthermore, the frequency offset and FWHM determined from a Creatine signal was used as starting parameter for the fit. After fitting, all spectra per volunteer were sorted by flip angle after B_1 inhomogeneity correction. Data points within manually segmented regions of interest (ROIs) of the brain (gray and white matter) were plotted and fitted to the Steady-State Incoherent (SSI) signal[14] as function of the flip angle to estimate the T_1 relaxation time:

$$\hat{\rho}_{SSI}(\theta) = \rho_0 sin\theta \frac{(1 - E_1)}{(1 - E_1 cos\theta)} e^{-T_E/T_2^*} \tag{3.2}$$

where θ is the flip angle, ρ_0 is the spin density and E_1 is e^{-TR/T_1}.

High Resolution MRSI: The water signal and residual was removed from the metabolite data as discussed earlier[19]. The water-removed spectra were then zero-order phase corrected to maximize the amplitude of the NAA peak, and then shifted so that the NAA peak was always at 2.05ppm. This should allow 2D maps of metabolites to be easily created, based on metabolite peak amplitude or area.

The spectra were acquired at very short TR, and were therefore T_1 and B_1 weighted. Equation 3.2 was used to correct the spectra for variations in B_1, T_1 and M_0, as previously attempted in[6], where TR was assumed to be 300ms, T_1 was 405ms for WM and 265ms for GM and θ is a B_1^+ map. The PD map (ρ in equation 3.2) required was obtained by correcting a high resolution FFE image for transmit (B_1^+) and receive (B_1^-) inhomogeneities, and scaling it down to the MRSI resolution. A further step was taken to correct for any receive coil inhomogeneities, by using the modulus of a B_0 map as a receive coil sensitivity map. This was an extra step performed before using equation 3.2. Correction was performed on averaged WM and GM spectra, with T_1 values in the $\hat{\rho}$ equation being set as the macromolecule T_1 values found in the previous part of this study (i.e. 405ms for WM and 265ms for GM). This resulted in spectra that were corrected for B_1 and T_1 saturation based on the relaxation properties of the underlying macromolecular baseline.

Metabolite-nulled MRSI: Metabolite-nulled MRSI spectra were collected to provide further insight into the differences of the macromolecular baseline between WM and GM. Various inversion times (TI) were explored for the DIR experiment, to achieve optimal metabolite nulling. Figure 3.11 shows an example of how metabolite signal is nulled with different TI times, and the optimal times used here, TI1 of 870ms and TI2 of 296ms.

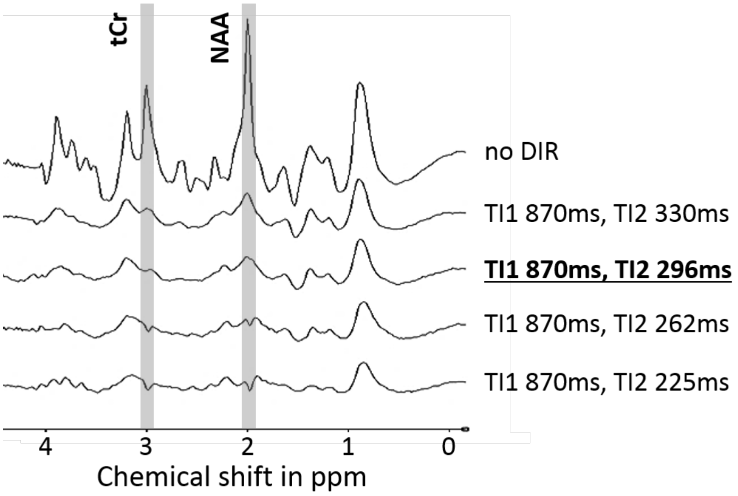

Figure 3.11: Metabolite nulling using Double Inversion Recovery (DIR). A full metabolite spectrum is shown at the top, with metabolite nulled spectra underneath. The Optimal TI times chosen are TI1 of 870ms and TI2 of 296ms (experimental data).

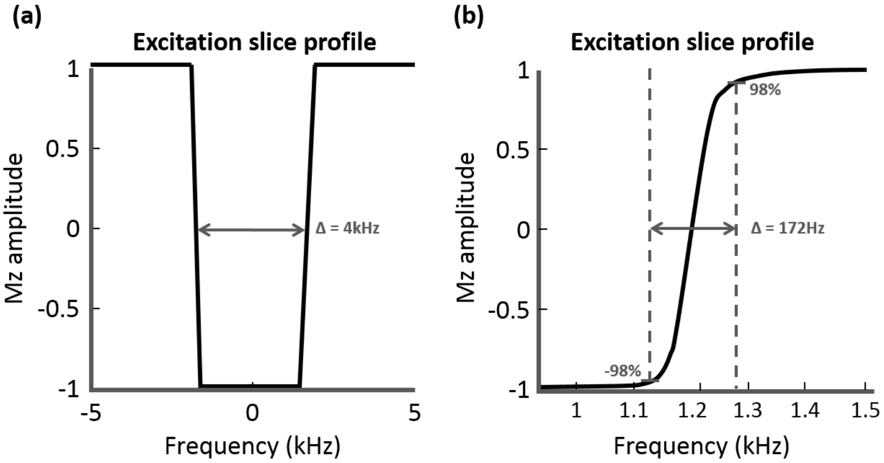

Figure 3.12: Excitation pulse used to invert metabolite signal. (a) shows the full bandwidth of the pulse, from -5kHz to 5kHz and (b) shows the transition from -98% to 98% Mz amplitude, at 172Hz wide.

The inversion pulse used (Figure 3.12) was designed to cover a wide range of the spectrum (2.2kHz at 98% inversion) and null all metabolites to give pure macromolecular signal. Water signal and sidebands were removed and the spectra were phase corrected as explained earlier. Voxels from mainly gray and mainly white matter were averaged to obtain a measured MM profile at short TE and long TR.

3.3.3 Results

T_1 mapping

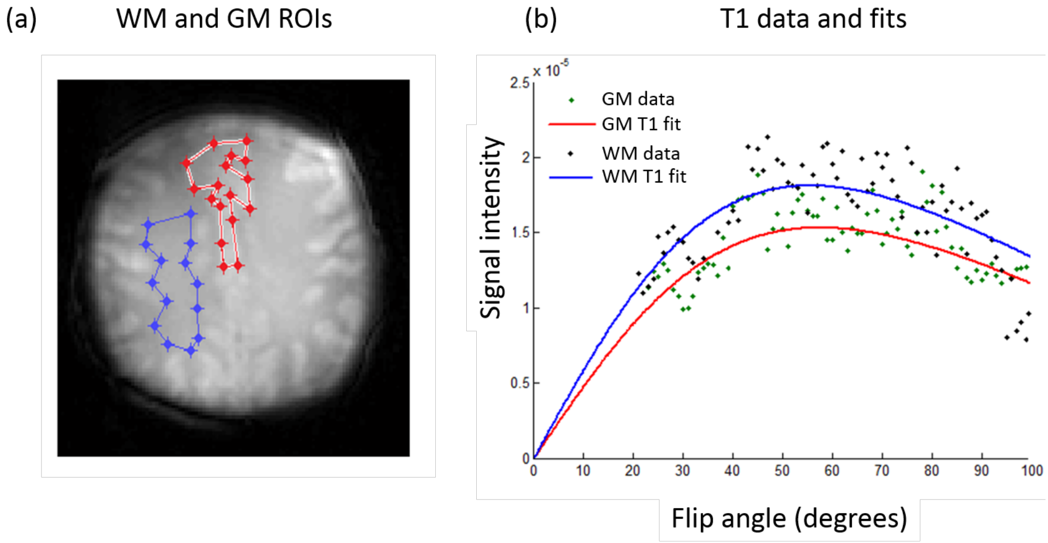

Figure 3.13: (a) Locations of the analyzed GM (red) and WM (blue) areas within a lipid signal crushed transverse brain slice. (b) Flip angle data for the voxels within the ROIs of GM and WM for macromolecule T_1 estimation (dots) and the fit by using the function of the SSI signal (equation 3.2) as function of the flip angle as obtained from a B_1 map.

T_1 was estimated from the variation of the SSI (equation 3.2) signal with flip angle. Figure 3.13b shows a graph of macromolecule SSI signal vs. flip angle for the voxels within the WM and GM regions shown in Figure 3.13a, and the fit to equation 3.2. The T_1 relaxation times for glutamate and the macromolecules are summarized in table 3.1.

The mean T_1 relaxation time for the macromolecules in WM and GM over 6 volunteers were 405 ± 70ms and 265 ± 30ms respectively. These T_1 relaxation times for WM and GM significantly differ (p = 0.01). The average glutamate T_1 value over the 6 volunteers was 1570 ± 50ms.

Table 3.1: T_1 relaxation times for Glutamate and macromolecules for 6 volunteers

Volunteer number	T_1 MM WM (ms)	T_1 MM GM (ms)	T_1 Glutamate GM (ms)
1	484	253	1630
2	337	288	1480
3	498	217	1610
4	380	263	1585
5	335	308	1570
6	395	263	1570
Mean + St.d.	**405 ± 71**	**265 ± 31**	**1574 ± 52**

High resolution MRSI

The water subtracted and phase-corrected spectra were used to create maps of metabolites and macromolecules, but various factors introduce artefacts and uncertainty in the results. Figure 3.14 shows a 2D map of the NAA peak (which is the largest effect observed in NMR spectroscopy and MRSI) together with a B_1 map, a 2D FFE image scanned at the same resolution as the MRSI dataset and a water map acquired with CSI.

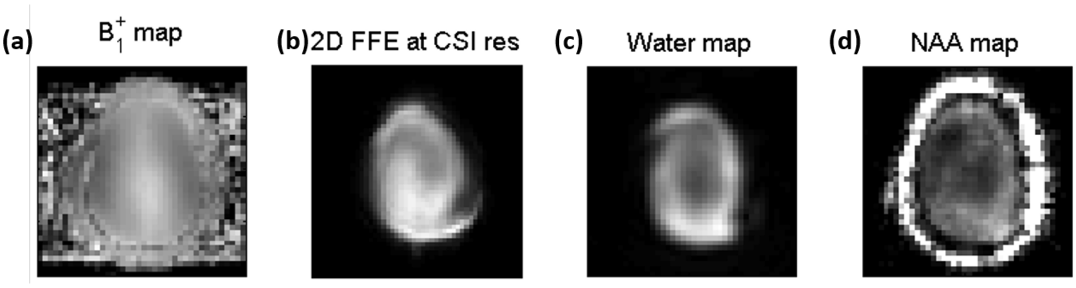

Figure 3.14: (a) acquired B_1 map. (b) 2D FFE at CSI resolution (40x40). (c) water area map from CSI. (d) NAA amplitude map (note the high signal intensity around the skull, caused by the crusher coil distorting the acquired FID).

The NAA map shows an unexpected inhomogeneous distribution across the brain, which can also be seen in the FFE image and the water map. This is likely

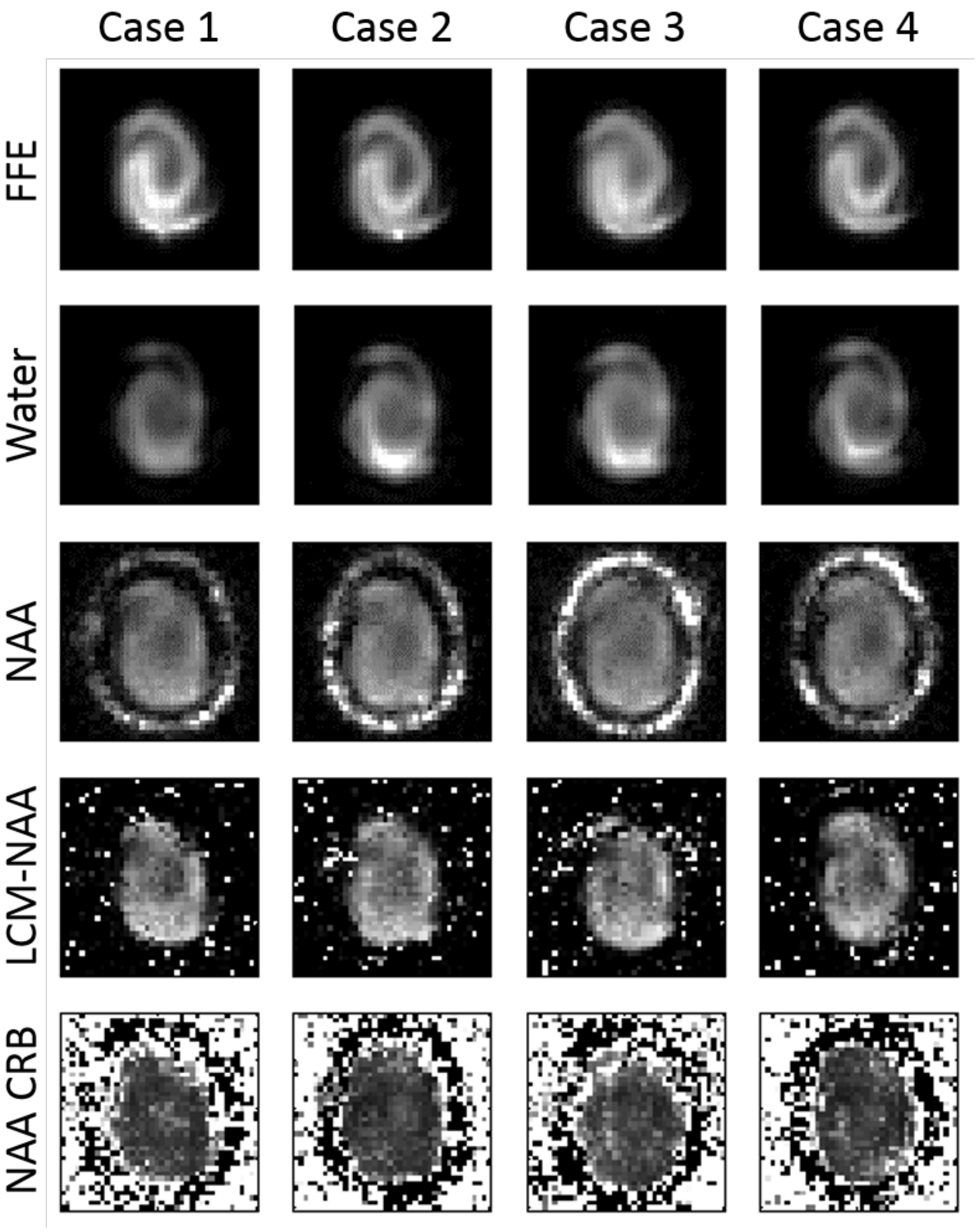

Figure 3.15: Four cases showing inhomogeneous FFE, water and NAA signal, as well as LCModel fitted NAA results. The four cases are from separate scans and subjects. The images in each row are scaled to the same signal intensity. The CRB maps are scaled in %, with ≈7-15% values in the brain.

caused by the presence of the crusher coil within the RF receive coil, as well as the signal crushing. Figure 3.15 shows four more cases of inhomogeneous FFE, water and NAA signal across the brain, together with LCModel fitted NAA amplitude and Cramér-Rao lower bound (CRB) values. All metabolite maps show this inhomogeneous contrast and are therefore not shown here. Regions where the NAA or water map show high intensity indicate higher SNR in the MRSI data, so Regions of Interest (ROI) analysis was performed in those areas. ROIs were drawn on a high resolution anatomical image, which gives good contrast between WM and GM, and then transferred onto the MRSI dataset. A B_1^- map was used to remove any receive coil inhomogeneities from the MRSI dataset, and the averaged WM and GM ROI spectra were signal-corrected using equation 3.2.

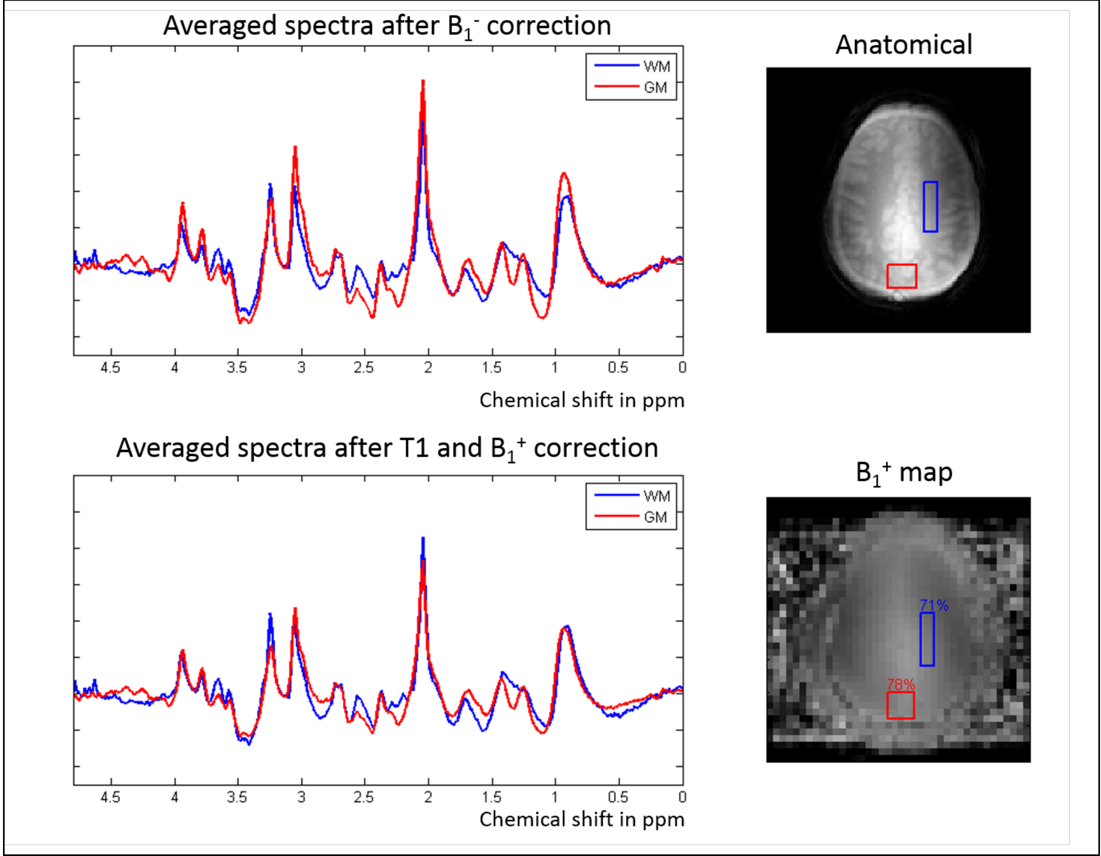

Figure 3.16: Effect of signal correcting two spectra, one in the WM with 71% average B_1 (blue) and one in the GM with 78% average B_1 (red). The signal amplitude between the MM in WM and GM is corrected, and the amplitudes of metabolites like NAA, Cr and Cho can now be compared.

Before and after signal correction examples are shown in figure 3.16. The correction method was applied to both the high resolution MRSI spectra and to the metabolite-nulled MRSI spectra. Because T_1 maps were not acquired for these scans, applying signal correction voxel-wise was not possible. Instead, T_1 was assumed to be 405ms for WM and 265ms for GM, based on the T_1 of the MM measured earlier.

Metabolite-nulled MRSI

The same inhomogeneous signal was observed in the metabolite-nulled data as well, with even lower SNR, so a study of the spatial distribution of metabolite intensities was not attempted. The metabolite-nulled MRSI datasets were acquired at low spatial resolution (18x18) so spectra were selected with mostly WM contribution or mostly GM contribution. Signal correction was performed in the same way as before, but in this case on single-voxel spectra, not an averaged ROI spectrum. Figure 3.17 shows WM and GM spectra acquired using the two different methods ((a)MRSI and (b) metabolite-nulled MRSI. Note that the signal intensities (y-axis) in part (b) were scaled up for visualization purposes). Macromolecules M1 – M9 are labelled on both sets of spectra. Figure 3.17 shows saturation-corrected spectra.

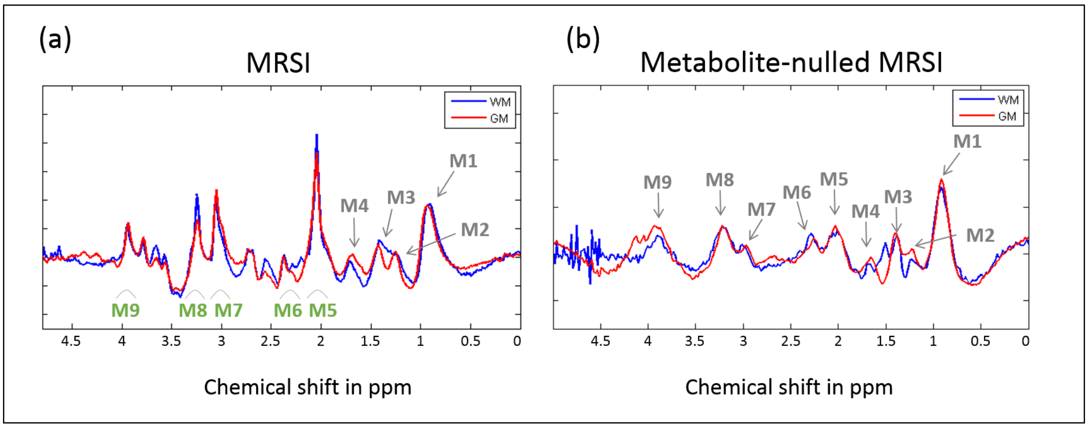

Figure 3.17: (a) Water removed averaged spectra (including metabolites) vs. (b) Metabolite-nulled averaged spectra for WM (blue) and GM (red). The spectra in (a) are from averaged ROIs whereas the spectra on the right are from single voxels in the metabolite-nulled MRSI dataset.

3.3.4 Discussion

In this study we investigated the relaxation, spectral and regional differences of macromolecular spins in the human brain using T_1 mapping, high resolution MRSI and metabolite nulling with a crusher coil at 7T. The T_1 mapping experiment has shown that there is a considerable difference between the relaxation of MM in the WM and GM. A more careful examination of the MM signal is required if the signal is to be fitted and removed from metabolite spectra.

Two more measurements were carried out to study the macromolecular baseline further; a low spatial resolution, metabolite-nulled MRSI study, to acquire a MM spectrum with minimized contribution of metabolites in WM and GM, and a higher spatial resolution, non-metabolite-nulled MRSI measurement to observe how the signal intensity of brain metabolites changes between WM and GM when MM relaxation differences are taken into account.

Multiple technical limitations have to be overcome for robust quantification of spectra. These include lipid contamination, transmit B_1^+ inhomogeneity and receive coil sensitivity, external field (B_0) shift, CSDEs, T_2 relaxation and TE, T_1 relaxation and TR and finally SAR limitations. CSDEs increase with B_0 field strength, and are therefore severe at 7T, but can be mitigated by the use of adiabatic pulses, as previously demonstrated by various groups[1,3,6,29]. Lipid contamination, especially from the scalp near the cortical GM, is also a common problem at 7T MRSI. Multiple methods exist to suppress lipid signal like OVS[20], adiabatic inversion recovery[2], RF shimming[16] or simply by improving the point spread function by increasing the matrix size and applying spatial Hamming filtering[6], but most of these methods involve altering the pulse sequence which results in long TR values and loss of signal. Our approach was to suppress any signal coming from the scalp by using a gradient crusher coil positioned between the head and the head coil[5]. This allowed for the MRSI pulse sequence to remain unchanged and for TR values to be as low as 300ms.

However, the work of this chapter has shown that there are limitations when using a crusher coil, as seen by the inhomogeneous signal in the NAA map as well as the water map. We were therefore unable to produce 2D maps of metabolite and macromolecule concentration. Further investigation also showed a reduction of around 40% in SNR when the crusher coil is placed inside the RF receive coil but not turned on. The source of the whirlpool-like signal seen in the NAA and water maps (See Figure 3.14 and 3.15) is currently being investigated with further phantom scanning in Utrecht, but is likely to be linked to the crusher coil. Additionally, the very short TR of the acquisition results in strong T_1 and B_1 weighting in the resulting spectra, and therefore maps of the metabolites or MM without saturation correction would give no meaningful contrast. Voxel-wise correction requires knowledge of voxel T_1, which was not available in this study, so results are only shown for single or averaged WM and GM spectra. The spectra were corrected using equation 3.2, which includes T_1, B_1^+ and proton density, and Figure 3.16 shows the result of this correction based on MM T_1 relaxation.

Since the T_2 of metabolites decreases with increasing B_0 field strength[9,36], a short TE is desirable so that as little signal as possible is lost due to T_2 decay. In this study we acquired an FID in a pulse-acquire method that allowed for a short TE of 2.5ms. This minimized any signal loss and first-order phase problems. Finally, B_0 was well controlled with shimming and SAR was kept low by avoiding complex pulse sequences required by OVS.

To study the different MM peaks individually, an additional measurement was conducted where the long T_1 brain metabolites were nulled with the use of a Double Inversion Recovery (DIR) acquisition. Because of the DIR scheme, the TR of this metabolite-nulled MRSI measurement was much longer than the TR of the normal MRSI acquisition (1000ms vs. 300ms), making direct comparison between the spectra difficult.

Studying the macromolecular baseline across the head without any contribution from metabolites has proven quite challenging. Even though a crusher coil was used for lipid suppression to speed up the experiment, the acquired data were still of very low spatial resolution, making it very difficult to study WM and GM regions separately. Furthermore, even with four averages (NSA = 4) the SNR is low. The results shown in Figure 3.17b look very promising, but they show an example of one (of very few) pairs of spectra that the signal correction works successfully with.

In the future, if the whirlpool effect can be eliminated, the crusher coil can be used to collect even higher resolution MRSI data with Echo Planar Spectroscopic Imaging (EPSI) which has a gradient during readout and can measure an entire k-line per TR instead of a single point in k-space. This will shorten the scan duration and allow for more averaging, giving higher SNR and a finer point spread function. Additionally, parallel imaging techniques using Controlled Aliasing In Parallel Imaging Results IN Higher Acceleration (CAIPIRINHA) together with short water suppression schemes and no lipid suppression in the pulse sequence (implemented in post processing), have been recently used to push the spatial resolution up to 128x128 with comparable SNR (NAA CRB as low as 10%), although retaining the high SNR required a scan duration of ≈40min.[15].

3.4 Summary

The study of brain macromolecules is becoming increasingly important as it helps with better quantification of brain metabolites and more importantly has the potential of becoming a new biomarker for disease, specifically neurodegeneration. This study has shown that there are clear relaxation and spectral differences between the macromolecular signal in WM and GM. The findings should be used as an indication that the mechanisms underlying the MM signal are not fully understood and should be investigated further, more specifically the relaxation properties of the individual MM peaks.

While the source of the MT signal remains evasive and difficult to investigate, multiple *z-spectroscopy*-based methodologies have been developed in an attempt to quantify the effect. The next chapter of this thesis describes a novel fully quantitative methodology we have developed to simultaneously measure MT, NOE and CEST effects *in-vivo* in the human brain, followed by the final chapter on various applications of this method, in both healthy and diseased human brain.

Bibliography

[1] Ovidiu C. Andronesi, Saadallah Ramadan, Eva Maria Ratai, Dominique Jennings, Carolyn E. Mountford, and A. Gregory Sorensen. Spectroscopic imaging with improved gradient modulated constant adiabaticity pulses on high-field clinical scanners. *Journal of Magnetic Resonance*, 203(2):283–293, 2010.

[2] Priti Balchandani and Daniel Spielman. Fat suppression for 1H MRSI at 7T using spectrally selective adiabatic inversion recovery. *Magnetic Resonance in Medicine*, 59(5):980–988, 2008.

[3] Priti Balchandani, John Pauly, and Daniel Spielman. Interleaved narrow-band PRESS sequence with adiabatic spatial-spectral refocusing pulses for 1H MRSI at 7T. *Magnetic Resonance in Medicine*, 59(5):973–979, 2008.

[4] K L Behar, D L Rothman, D D Spencer, and O a Petroff. Analysis of macromolecule resonances in 1H NMR spectra of human brain. *Magnetic Resonance in Medicine*, 32(3):294–302, 1994.

[5] Vincent O. Boer, Tessa van de Lindt, Peter R. Luijten, and Dennis W J Klomp. Lipid suppression for brain MRI and MRSI by means of a dedicated crusher coil. *Magnetic Resonance in Medicine*, 2068:2062–2068, 2014.

[6] W Bogner, S Gruber, S Trattnig, and M Chmelik. High-resolution mapping of human brain metabolites by free induction decay (1)H MRSI at 7 T. *NMR in biomedicine*, 25(6):873–82, 2012.

[7] RL Davis and DM Robertson. *Journal of Neuropathology.* Williams & Wilkins, 3rd edition, 1997.

[8] RA de Graaf. NMR Processing Software for Spectroscopy, Imaging, and Spectroscopic Imaging, 1999.

[9] Robin a de Graaf, Peter B Brown, Scott McIntyre, Terence W Nixon, Kevin L Behar, and Douglas L Rothman. High magnetic field water and

metabolite proton T1 and T2 relaxation in rat brain in vivo. *Magnetic resonance in medicine : official journal of the Society of Magnetic Resonance in Medicine / Society of Magnetic Resonance in Medicine*, 56(2):386–394, 2006.

[10] J Frahm, H Bruhn, W Hanicke, K D Merboldt, K Mursch, and E Markakis. Localized proton NMR spectroscopy of brain tumors using short-echo time STEAM sequences. *J Comput Assist Tomogr*, 15(6):915–922, 1991.

[11] E K Fram, R J Herfkens, G a Johnson, G H Glover, J P Karis, a Shimakawa, T G Perkins, and N J Pelc. Rapid calculation of T1 using variable flip angle gradient refocused imaging. *MRI*, 5(3):201–208, 1987.

[12] Alexander Fuchs, Mariska Luttje, Peter Boesiger, and Anke Henning. SPECIAL semi-LASER with lipid artifact compensation for 1H MRS at 7 T. *Magnetic Resonance in Medicine*, 69(3):603–612, 2013.

[13] G D Graham, J H Hwang, D L Rothman, and J W Prichard. Spectroscopic assessment of alterations in macromolecule and small-molecule metabolites in human brain after stroke. *Stroke; a journal of cerebral circulation*, 32(12): 2797–2802, 2001.

[14] E Mark Haacke, Robert W Brown, Michael R Thompson, and Ramesh Venkatesan. *Magnetic Resonance Imaging: Physical Principles and Sequence Design*, volume 1st. John Wiley & Sons, Inc., 1999. ISBN 0471351288.

[15] Gilbert Hangel, Bernhard Strasser, Michal Považan, Eva Heckova, Lukas Hingerl, Roland Boubela, Stephan Gruber, Siegfried Trattnig, and Wolfgang Bogner. Ultra-high resolution brain metabolite mapping at 7 T by short-TR Hadamard-encoded FID-MRSI. *NeuroImage*, 2016.

[16] Hoby P Hetherington, Nikolai I Avdievich, Andrey M Kuznetsov, and Jullie W Pan. RF shimming for spectroscopic localization in the human brain at 7 T. *Magnetic resonance in medicine*, 63(1):9–19, 2010.

[17] The MathWorks Inc. MATLAB (R2015b). *The MathWorks Inc.*, 2015.

[18] Zhaleh Khaleeli, Daniel R Altmann, Mara Cercignani, Olga Ciccarelli, David H Miller, and Alan J Thompson. Magnetization transfer ratio in gray matter: a potential surrogate marker for progression in early primary progressive multiple sclerosis. *Archives of neurology*, 65(11):1454–1459, 2008.

[19] A Maudsley, C Domenig, and Y Yu. Water Suppression in 1H MRSI by Reference Subtraction. In *Proceedings 14th Scientific Meeting, International Society for Magnetic Resonance in Medicine*, page 3068, 2006.

[20] Ralf Mekle, Vladimir Mlynarik, Giulio Gambarota, Martin Hergt, Gunnar Krueger, and Rolf Gruetter. MR spectroscopy of the human brain with enhanced signal intensity at ultrashort echo times on a clinical platform at 3T and 7T. *Magnetic Resonance in Medicine*, 61(6):1279–1285, 2009.

[21] C. Morrison, G. Stanisz, and R.M. Henkelman. Modeling Magnetization Transfer for Biological-like Systems Using a Semi-solid Pool with a Super-Lorentzian Lineshape and Dipolar Reservoir. *Journal of Magnetic Resonance, Series B*, 108(2):103–113, 1995.

[22] J. P. Mottershead, K. Schmierer, M. Clemence, J. S. Thornton, F. Scaravilli, G. J. Barker, P. S. Tofts, J. Newcombe, M. L. Cuzner, R. J. Ordidge, W. I. McDonald, and D. H. Miller. High field MRI correlates of myelin content and axonal density in multiple sclerosis: A post-mortem study of the spinal cord. *Journal of Neurology*, 250(11):1293–1301, 2003.

[23] P A Narayana, J S Wolinsky, E F Jackson, and M McCarthy. Proton MR spectroscopy of gadolinium-enhanced multiple sclerosis plaques. *J.Magn Reson.Imaging*, 2(3):263–270, 1992.

[24] André Pampel, Dirk K Müller, Alfred Anwander, Henrik Marschner, and Harald E Möller. Orientation dependence of magnetization transfer parameters in human white matter. *NeuroImage*, 114:136–46, jul 2015.

[25] W. W F Pijnappel, A van den Boogaart, R de Beer, and D van Ormondt.

SVD-based quantification of magnetic resonance signals. *Journal of Magnetic Resonance (1969)*, 97(1):122–134, 1992.

[26] S Posse, B Schuknecht, M E Smith, P C van Zijl, N Herschkowitz, and C T Moonen. Short echo time proton MR spectroscopic imaging. *J Comput Assist Tomogr*, 17(1):1–14, 1993.

[27] Michal Považan, Gilbert Hangel, Bernhard Strasser, Stephan Gruber, Marek Chmelik, Siegfried Trattnig, and Wolfgang Bogner. Mapping of brain macromolecules and their use for spectral processing of (1)H-MRSI data with an ultra-short acquisition delay at 7T. *NeuroImage*, 121:126–135, jul 2015.

[28] Stefan Ropele and Franz Fazekas. Magnetization Transfer MR Imaging in Multiple Sclerosis, 2009.

[29] Tom W J Scheenen, Dennis W J Klomp, Jannie P. Wijnen, and Arend Heerschap. Short echo time 1H-MRSI of the human brain at 3T with minimal chemical shift displacement errors using adiabatic refocusing pulses. *Magnetic Resonance in Medicine*, 59(1):1–6, 2008.

[30] Klaus Schmierer, Francesco Scaravilli, Daniel R. Altmann, Gareth J. Barker, and David H. Miller. Magnetization transfer ratio and myelin in postmortem multiple sclerosis brain. *Annals of Neurology*, 56(3):407–415, 2004.

[31] Uwe Seeger, Uwe Klose, Irina Mader, Wolfgang Grodd, and Thomas Nagele. Parameterized evaluation of macromolecules and lipids in proton MR spectroscopy of brain diseases. *Magnetic Resonance in Medicine*, 49(1):19–28, 2003.

[32] George J. Siegel, R. Wayne Albers, Scott T. Brady, and Donald L. Price. *Basic neurochemistry : molecular, cellular and medical aspects.* Elsevier, 7th edition, 2006.

[33] Christopher D J Sinclair, Rebecca S. Samson, David L. Thomas, Nikolaus Weiskopf, Antoine Lutti, John S. Thornton, and Xavier Golay. Quantitative

magnetization transfer in in vivo healthy human skeletal muscle at 3 T. *Magnetic Resonance in Medicine*, 64(6):1739–1748, 2010.

[34] I Tkác, P Andersen, G Adriany, H Merkle, K Ugurbil, and R Gruetter. In vivo 1H NMR spectroscopy of the human brain at 7 T. *Magnetic resonance in medicine : official journal of the Society of Magnetic Resonance in Medicine / Society of Magnetic Resonance in Medicine*, 46(3):451–6, 2001.

[35] Ivan Tkác, Gülin Oz, Gregor Adriany, Kamil Uğurbil, and Rolf Gruetter. In vivo 1H NMR spectroscopy of the human brain at high magnetic fields: metabolite quantification at 4T vs. 7T. *Magnetic resonance in medicine : official journal of the Society of Magnetic Resonance in Medicine / Society of Magnetic Resonance in Medicine*, 62(4):868–79, 2009.

[36] Frank Träber, Wolfgang Block, Rolf Lamerichs, Jürgen Gieseke, and Hans H. Schild. 1H Metabolite Relaxation Times at 3.0 Tesla: Measurements of T1 and T2 Values in Normal Brain and Determination of Regional Differences in Transverse Relaxation. *Journal of Magnetic Resonance Imaging*, 19(5): 537–545, 2004.

[37] B. L. van de Bank, U. E. Emir, V. O. Boer, J. J. a. van Asten, M. C. Maas, J. P. Wijnen, H. E. Kan, G. Oz, D. W. J. Klomp, and T. W. J. Scheenen. Multi-center reproducibility of neurochemical profiles in the human brain at 7T. *NMR in Biomedicine*, 28(3):306–316, 2015.

[38] Tessa van de Lindt, Ronald Mooiweer, Peter R. Luijten, Dennis W. J. Klomp, and Vincent O. Boer. Fast water suppression for high resolution MRSI by frequency selective spokes pulses at 7 T. In *ISMRM*, page 3766, 2014.

Chapter 4

Quantitative analysis of the Z-spectrum using a numerically simulated Look Up Table (LUT)

4.1 Abstract

This chapter describes a novel method developed to provide accurate and reliable estimation of MT and CEST parameters, specifically proton pool concentrations. The motivation for this work comes from the increasing use of MT and CEST in characterising demyelinating disease and brain tumours, and the lack of a standardised methodology for doing so. The hypothesis this work is based on is that the most precise and reliable way to estimate MT and CEST parameters is by fitting acquired spectra to a multi-pool model, taking account of all variables like B_1 saturation power, water T_1 recovery and all saturation and imaging pulse sequence parameters. Although accurate and reliable, this method comes with a very high computational cost and is therefore unrealistic when a large number of

spectra need to be quantified (as is the case when investigating large tumours). In this method we propose an alternative to fitting individual spectra, by instead matching them to a large database of pre-simulated spectra to extract the proton pool concentrations.

4.2 Introduction

Magnetization Transfer (MT), Chemical Exchange Saturation Transfer (CEST) and Nuclear Overhauser Effect (NOE) phenomena use the transfer of magnetization, or exchange of protons or molecules to sensitize the visible water proton pool to macromolecules or certain moieties[26]. Conventional Magnetization Transfer Ratio (MTR) images are sensitive to a combination of these effects depending on the frequency, power and timing of the off-resonance saturation used. On the other hand, the *z-spectrum*[1] acquires MTR data at various frequency offsets making it potentially possible to investigate all of these phenomena.

However, quantifying the effects of these different processes in the *z-spectrum* remains a challenge since RF irradiation used to probe the various pools will saturate more than one pool, and will generally also cause Direct water Saturation (DS). The spectrum is therefore a mixture of MT, DS, NOE and CEST signals, and the different components are difficult to separate[26,35–37]. Early assessment of the CEST effect was based on asymmetry analysis[39] but this is confounded if independent changes are occurring on either side of the *z-spectrum*. More recent studies have used Lorentzian fitting[8,36] and Lorentzian difference methods of analysis[5]. These methods are relatively simple and may be adequate in some circumstances (for instance where the RF power is well controlled), but are not quantitative, because the effects of the different pools do not add linearly particularly at high saturation powers, and because changes in T1 and RF power[3,25] will perturb the results. Other methods attempt to suppress the MT contribution by applying double frequency irradiation[10,23] but the CEST effects are still diluted by MT and DS, even if isolated from them.

Steady-state saturation is often used for MT imaging and quantification, with the drawback of high SAR and low SNR in the resulting images, but with the advantage of providing an analytical solution for *z-spectrum* quantification. However, a pulsed saturation scheme which does not reach steady state provides increased SNR for high resolution scanning with wide (3D) coverage. The drawback of the saturation not reaching a steady state is that it has proven difficult to analytically determine the signal in the *z-spectra* taking account of the effects of all possible field inhomogeneities. A recent paper[14] has proposed an analytical method of simultaneously determining the concentration and exchange rates of intermediate to fast exchanging protons, in the case of pulsed pre-saturation. So far a numerical computation of the evolution of the various pools is considered to be the gold standard, but involves a large computational cost[2]. In order to avoid the computationally time-consuming requirement to simulate the *z-spectra* for every voxel, here we propose a method of, in effect, fitting *z-spectra* acquired in the pseudo-steady state by comparing the acquired spectra to a large predefined database of numerically simulated spectra based on the Bloch-McConnell equations. The database includes proton pool concentrations, B_1 inhomogeneity and T_1 information.

One particular problem in quantifying *z-spectrum* phenomena is sensitivity to RF saturation power. The *z-spectrum* is sensitive to different pools at different RF powers depending on exchange rates, so inevitable variations in RF power setting and RF inhomogeneity will cause varying sensitivity to different pools. Here we have attempted to mitigate these problems by acquiring data at varying RF powers.

The aim of this work is to develop a new method of quantifying the separate proton pool concentrations from *z-spectra* of the human brain at 7T, by using a look-up table (LUT) and taking account of T_1 and B_1 variations. The sensitivity of the approach has been investigated using Monte Carlo (MC) simulations. It has been tested for measuring MT, NOE and Amide Proton Transfer (APT) CEST in 10 healthy volunteers, and a repeatability study has also been conducted.

4.3 Methods

4.3.1 Model

Fundamentally this method involved, in effect, fitting the *z-spectra* to a model based on the Bloch McConnell equations. However, given the computational time required to simulate model spectra in a non-steady state, measured spectra were instead compared to a LUT (database of simulated spectra) calculated in advance, similar to the dictionaries used in Magnetic Resonance Fingerprinting (MRF)[13].

A four pool version of the modified Bloch McConnell equations (described in Chapter 2.3) was used to create a database of simulated *z-spectra*. The model assumes four interacting pools of protons that consist of (i) the free water magnetization (free pool, M_0^f), (ii) macromolecules and the hydration layer (bound pool, M_0^b), (iii) small proteins in chemical exchange with the free pool at a single frequency, in this case considering Amide Proton Transfer (APT) (exchanging pool, M_0^c) and (iv) protons experiencing dipole cross relaxation through space with the free water magnetization (Nuclear Overhauser Effect – NOE pool, M_0^n). The Bloch-McConnell can be summarized as[29]

$$\frac{dM(t,\omega_{rf})}{dt} = A(t,\omega_{rf}) \cdot M(t,\omega_{rf}) + B \cdot M_0 \tag{4.1}$$

where M is a vector describing the time evolution of each of the proton pools, and A and B are matrices describing the effect of RF saturation, exchange between each proton pool and the free water pool, longitudinal relaxation rates of each proton pool and the lineshape of the bound pool. A full description of this model and its numerical implementation are given elsewhere[17]. It is assumed that each pool can be described by a single transverse relaxation time T_2, except for the macromolecular associated pool which is assumed to be described by a Super-Lorentzian lineshape[15,18,24,27], centred at -2.4ppm relative to water. It is also assumed that all pools are in exchange with the water pool but direct exchange between the other pools is negligible.

No simple analytical solution to this equation exists in the approach to steady state, so instead an Ordinary Differential Equation (ODE) solver was implemented to compute the evolution of the magnetization of the different pools during the approach to saturation, using a 4th order Runge-Kutta algorithm with a 5μs interval, taking account of the saturation and readout pulses used to reach the centre of k-space. This gave the longitudinal magnetization in the free water pool (M_z^f) in the simulated z-spectra.

4.3.2 Estimating parameters from a Look Up Table (LUT)

Z-spectra were simulated for the RF saturation train used to acquire in-vivo spectra (20 Gaussian windowed Sinc RF pulses of bandwidth BW = 200Hz, 30ms long, repeated every T = 60ms, for a 50% duty cycle), at fifteen different off-resonance frequencies of the saturation pulse (Table 4.1). The choice of off-resonance frequencies was determined by examining the Full Width at Half Maximum (FWHM) of fitted Lorentzian curves. The different pools were sampled at frequencies corresponding to their maximum amplitude and FWHM, with more frequencies and therefore more weighting given to the NOE and MT pools. A 50kHz off–resonance saturation was also simulated for normalization of the spectrum.

Different saturation pulse powers provide sensitivity to the different pools (Figure 4.1a), therefore we investigated the potential advantages of simultaneously

Table 4.1: Physical parameters used in the simulation of the database (look-up table).

	Relative concentration (M_0 %)	**T_1 (s)**	**T_2 (ms)**	**Exchange rate with free water pool (Hz)**	**Chemical shift (ppm)**	**Off-resonance saturation frequencies (ppm)**	**B_1 amplitude**	**B_1 scaling**
Free water pool (DS)	-	Five values (1, 1,2, 1,6, 2 and 3 s)	40	-	0	-16.7 -6.7 -4.7 -4 -3.5 -3 -2.3 -1 0 1 2.5 3.5 4.5 6.7 16.7	Nominal B_1 amplitudes of 0.38, 0.75 and 1.25μs $B_{1,RMS}$	Saturation and imaging pulses scaled by 30, 60, 80, 100, 120 and 150%
Bound pool (MT)	Eight values (0.1, 1, 2, 5, 8 ,10, 12 and 15 %)	1	0.009	50	-2.4			
NOE pool	Five values (0.1, 1, 2, 3.5, 5, 6, 8 and 10 %)	1	0.3	10	-3.5			
CEST pool (APT)	Five values (0.02, 0.05, 0.075, 0.1, 0.2, 0.3, 0.5 and 1 %)	1	10	200	3.5			

fitting B_1-coupled spectra acquired at one, two or three powers to optimize the fitting across the different pools. Spectra were simulated for nominal $B_{1,sat}$ (maximum RF amplitudes as defined in Figure 4.2) of 1.9μT, 3.8μT and 6.34μT at 50% duty cycle (equivalent to 0.38μT, 0.75μT and 1.25μT $B_{1,rms}$). Spectra were simulated for a range of pool concentrations and T_1 values (Figure 4.1b) of the free water pool, assuming the other physical parameters shown in Table 4.1.

The T_1 of the free pool was estimated from the observed T_1 and the T_1 of the other proton pools, as previously described[17,20]. Given the variability in the literature, the exchange rates used in this simulation were selected experimentally by initially performing a full fit to spectra from ROIs.

Unfortunately it is impossible to control the B_1 amplitude throughout the volume of interest, particularly at ultra-high field, and this inhomogeneity will alter both $B_{1,sat}$ and $B_{1,read}$ (Figure 4.2). Therefore three B_1-coupled spectra were

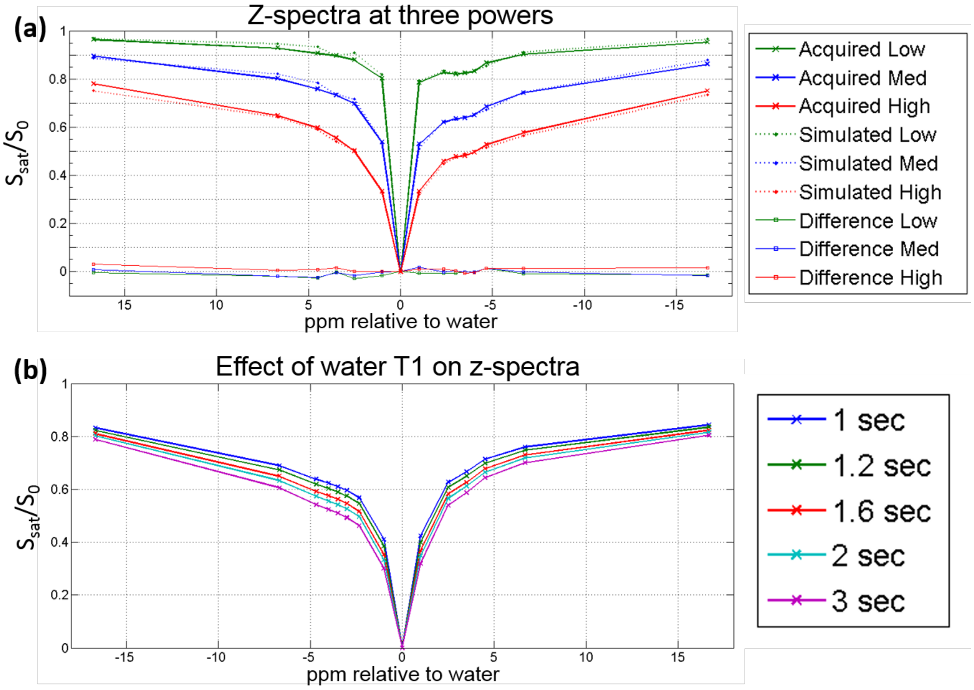

Figure 4.1: (a) Experimentally measured single WM voxel (solid) spectra compared to the fitted (dotted) spectra acquired at $B_{1,rms} = 0.38$ (green), 0.75 (blue) and 1.25 μT (red). The difference between the acquired and simulated spectra (acquired - simulated) is also shown. These three spectra were fitted as a coupled set of spectra acquired at three predefined powers, but they could also be fitted individually. (b) The effects of water T_1 on simulated *z-spectra*.

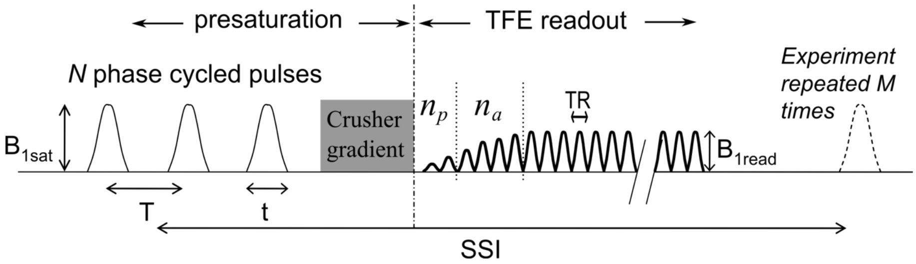

Figure 4.2: The magnetisation transfer-prepared turbo field echo (MT-TFE) sequence: presaturation period followed by the TFE readout. The presaturation period consists of 20 Gaussian windowed Sinc pulses, t = 30ms long and spaced T = 60ms apart, resulting in a 50% Duty Cycle. The crusher gradient at the end of the saturation train removes any residual transverse magnetisation. np = 2 and na = 4 are the number of ramped RF pulses before and at the start of the acquisition, respectively. From[17].

simulated (i.e. with different values of $B_{1,sat}$ but the same values of $B_{1,read}$) for various B_1 scaling factors to account for the effect of B_1 inhomogeneity or RF mis-adjustment. Linear interpolation was used to extend the simulated database

(Table 4.1, simulated for 3 $B_{1,sat}$ values, 6 $B_{1,scale}$, 8 MT, NOE and APT, and 5 T_1 values: 46,080 spectra) to yield spectra for 3 values of $B_{1,sat}$, 16 B_1 scaling factors, 17 T_1 values and 15 MT, NOE and APT concentrations, creating a database of 2.754 million spectra in total. The simulation of the database is computationally expensive (≈10,000 computing hours), taking about 1 week to compute using 128 cores on the University of Nottingham's High Performance Computing facilities.

The proton pool fractions were then estimated by comparing the experimentally measured spectra to the LUT by brute force least squares fitting. This involved calculating the sum of squares difference between the acquired spectrum and every spectrum in the LUT separately, and then selecting the parameters of the simulated spectrum with the smallest residual. This restricted possible fitted values only to the simulated or interpolated values. When fitting coupled triplets (or pairs) of spectra acquired at 3 different values of $B_{1,sat}$ as discussed above, the sum of squares difference was found between the three measured spectra (acquired with fixed ratios of $B_{1,sat}$) and sets of spectra simulated with the same known ratios of $B_{1,sat}$. The results of this fitting are shown in Figure 4.1a.

4.3.3 Monte Carlo simulations

Monte Carlo simulations were used to investigate the robustness of the fit, focusing particularly on the effect of variations in B_1 amplitude. Realistic levels of uniformly distributed noise (*rand* function in MATLAB) was added to a simulated spectrum which was then fitted to the LUT. This was repeated for 10,000 realisations of the noise to determine the resulting variance in the fitted parameters. The spectra were simulated for $M_0^b = 10\%$, $M_0^n = 6\%$ and $M_0^c = 0.25\%$, $T_1 = 1.2$s and the 3 nominal $B_{1,sat}$ amplitudes shown in Table 4.1 (initially with scaling factor of 100%). 2% noise relative to the normalized M_0 was added to each spectral point (assuming 8 minutes to acquire full spectrum), 10% noise was added to the T_1 map acquired in a 10 minute scan and 5% noise was added to the B_1 map acquired in a 3 minute scan.

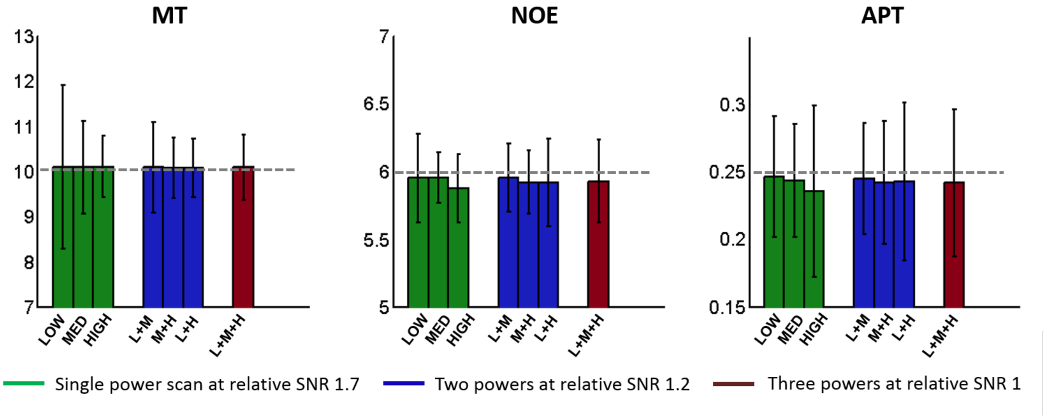

Figure 4.3: Mean and standard deviation in MT, NOE, and APT fit for different power combinations. The noise level assumed for each point in the *z-spectrum* was 1.15% for the single power (equivalent to 25 min/scan), 1.41% for two powers (equivalent to 12.5 min/scan), and 2% for three powers (equivalent to 8 min/scan). T_1 noise was 10% and B_1 noise was 5%. Relative SNR was calculated relative to the SNR of an 8min scan.

Since we know that the results of *z-spectrum* fitting are very sensitive to saturation power, we compared the effect of data acquired at 1, 2 or 3 coupled powers. We adjusted the noise in the simulated *z-spectra* to compensate for the necessary changes in the scan time at each power if the total scan time were to be kept constant (Figure 4.3), i.e. 1 spectrum at a single power with 1.15% noise or 3 spectra at 3 powers with 2% noise each. For a given total acquisition time, the times allowed to acquire the *z-spectra* and T_1 map were also counter-varied as shown in Table 4.2, i.e. as the time given to *z-spectrum* imaging reduced the time given to T_1 mapping increased, with the corresponding image noise levels being adjusted to maintain an SNR/time in each scan and constant total acquisition time. For a total acquisition time of 34 minutes, the times allowed for acquisiton of the T_1 map and *z-spectra* at three powers were varied from 1-16 minutes and 11–6 minutes per power respectively, so that the noise in the T_1 map varied from 31-8% and the noise in the *z-spectra* varied from 1.7%-2.2%. Finally the simulations were used to conduct a sensitivity analysis exploring the effects of B_1 and T_1 errors on MT, NOE and APT.

Table 4.2: Scan Times for T_1 Scan and Single Power *z-spectrum* Scan with Corresponding Simulated T_1 and *z-spectra* Scan Noise.

	Higher *z-spectra* SNR					**Higher T_1 SNR**			
Scan time, T_1 /z-spectra (min)	1/11.3	2/11	4/10.3	6/9.7	8/9	10/8.3	12/7.7	14/7	16/6.3
Z-spectra noise (%)	1.71	1.74	1.8	1.86	1.92	2	2.09	2.18	2.29
T_1 noise (%)	31.62	22.36	15.81	12.91	11.2	10	9.13	8.45	7.91

4.3.4 Data acquisition

Approval for human scanning was obtained from the University of Nottingham Medical School Ethics Committee. Ten healthy subjects (6 female, ages ranging from 19-62 and 4 male, ages ranging from 21-48) were scanned at 7T (Philips Achieva, using a 32-channel Nova head receive array) with a protocol based on the results of the Monte Carlo Simulations (three z-spectra scanned at different powers with 2% noise, T_1 map with 10% noise, and B_1 map and B_0 maps) to assess inter-subject variation. Another three subjects (2 males aged 29 and 34 and 1 female aged 52) were scanned three times each with exactly the same protocol to assess intra-subject repeatability.

Each point on the z-spectrum was acquired using a saturation-prepared 3D TFE sequence[17], (Figure 4.2). The saturation consisted of a train of N = 20 Gaussian windowed Sinc RF pulses of bandwidth BW = 200Hz, 30ms long, repeated every T = 60ms (50% duty cycle), with a phase increment between each pulse, and a spoiler gradient applied at the end of the train to remove any residual transverse magnetisation. *Z-spectra* were acquired by varying the off-resonance saturation frequency as shown in Table 4.1, including a scan at 50 kHz off-resonance for normalization. This was repeated for the three nominal values of $B_{1,sat}$ given in Table 4.1.

The imaging readout was a volume acquisition with a readout train of 410 gradient echoes, TE/TR/FA = 2.7ms/5.8ms/8°, FOV = 192x192x60mm^3, 1.5mm isotropic image resolution, low-high k-space acquisition and a SENSE factor (RL) of 2. The 3D volume acquisition required 5 repetitions of this cycle. Using this 3D non-steady state approach, a 15 point z-spectrum (plus an additional point for normalization), was acquired in 8 minutes (24 minutes total for the three powers). The amplitude of readout pulses was modulated to avoid large variations in signal at the start of the TFE train; there were 2 (np) ramped RF pulses before acquisition, followed by 4 (na) ramped RF pulses at the start of the acquisition, with the remaining pulses at constant flip angle alpha = 8° ($B_{1,read}$, Figure 4.2). Additionally a B_0 map (double echo method, FOV = 252x255x100mm^3 at 3x3x2mm^3 voxels) was acquired for B_0 correction (1 min), along with a whole head B_1 map (dual TR method, at 20ms and 120ms TR, FOV 205x180x132mm^3 at 3.2x4x4 mm^3 voxels, 3 min) and a T_1 map (dual readout PSIR data, FOV = 240x216x160mm^3 at 0.8mm isotropic resolution, SENSE factor (RL) of 2.2 and (FH) of 2, 10 min) giving a total scan time of 38 minutes.

4.3.5 Data pre-processing

Each *z-spectra* dataset was motion corrected using FSL's[7] *mcflirt* function and then all were registered to the same space using a high Contrast-to-Noise Ratio (CNR) image created by averaging across the dynamics of the *z-spectrum* acquired at the highest $B_{1,sat}$. SPM8[19] was used to segment White Matter (WM) and Grey Matter (GM) masks from the PSIR images that were retrospectively registered onto the high CNR image. The masks were thresholded at high probability values (≈ 0.9) to avoid partial volume errors. Similarly the B_0, B_1 and T_1 maps were registered onto the high CNR image space. B_0 correction of all the *z-spectra* datasets was performed voxel-wise prior to the fitting by shifting the whole spectrum based on the difference between the zero point (DS) and B_0 map as described in[35,39]. Regions with very high B_0 shift (above 200Hz) were removed from subsequent analysis as the spectra were too different to the simulated spectra.

4.3.6 Fitting the experimental data

The coupled spectra acquired at 3 different nominal values of $B_{1,sat}$ (and constant values of $B_{1,read}$) were simultaneously fitted to the database by calculating the total sum of squared error between the 3 measured spectra and a set of 3 spectra simulated for the same ratio of actual saturation powers and same actual readout pulse amplitudes. The B_1 map provided a B_1 scaling factor linking the nominal and actual RF powers (and hence $B_{1,sat}$ and $B_{1,read}$) in each voxel. We also recorded the RF drive scales from the Philips scanner for the B_1 map and *z-spectra* acquisitions to allow the B_1 map to be scaled to match the drive scales if necessary. The drive scale is an arbitrary value that is generated after power optimization (a pre-scan step), and relates to power adjustment needed to get the requested flip angle for the given load detected in the coil. The mean and standard deviation RF drive scale in the 10 *z-spectra* and B_1 scans were 0.34 ±0.03 and 0.35 ±0.06 respectively. However data collected with an RF drive scale of <0.22 (a fault state) were discarded since they produced spectra with $B_{1,sat}$ so low that it lay outside the simulated range. The T_1 map also constrained the search.

The fitting was done pixel-wise to create maps of M_0^b, M_0^n and M_0^c. Average values of M_0^b, M_0^n and M_0^c were estimated by averaging the fitted values over the WM and GM masks for the inter-subject variation study, and over ROIs of about 500 voxels in 3 regions of the corpus callosum (CC) for intra-subject repeatability. As a test of the fitting procedure, we also investigate the possibility of fitting the three spectra for B_1 scaling factor as well as pool sizes, since the variation in the *z-spectra* with RF amplitude is so large.

Finally for comparison the spectra were also fitted using the qualitative Lorentzian fitting[28] method. Four Lorentzian curves (Water, MT, NOE and APT) were fitted using least squares curve fitting and, to remove the effect of B_1 inhomogeneity in the Lorentzian maps and hence allow a fair comparison with the LUT approach, we interpolated the results from the three different powers to those expected for $B_{1,RMS} = 0.5\mu T$. The pools were quantified as the Area Under the Curve (AUC) of each fitted curve. We also carried out standard asymmetry analysis for comparison[6].

4.4 Results

4.4.1 Monte Carlo simulations

Figure 4.3 shows the mean and standard deviation in the fitted values when the *z-spectra* were simulated and fitted at only a single target power (Low, Medium or High), at two target powers (L+M, M+H or L+H) or at three target powers (L+M+H). The resulting mean fitted values were all within 1% of the original simulated values. The different combinations of power benefited different measures. For instance fitting the APT signal benefited from all the acquisitions being made at lower powers, whereas this increased the noise in the fit for the MT pool. The results show that if RF power is well controlled then medium power gives a reasonable fit across all three pools considered here (APT, NOE and MT). In reality, especially at 7T, B_1 is not well controlled and scanning at only one power increases the risk of losing data in outlying regions of B_1 amplitude. For this reason we chose to scan and fit for three powers.

Figure 4.4 a shows how the random error in the fitted values changed as the partition of the acquisition time between the T_1 map and *z-spectra* was counter varied whilst keeping the total acquisition time constant. The lowest random error in the fitted MT and NOE values was achieved when T_1 map noise was 10% and z spectra noise was 2%, corresponding to acquisition times of 10 minutes and 8 minutes respectively. On the other hand the lower APT signal benefited from a longer *z-spectrum* scan.

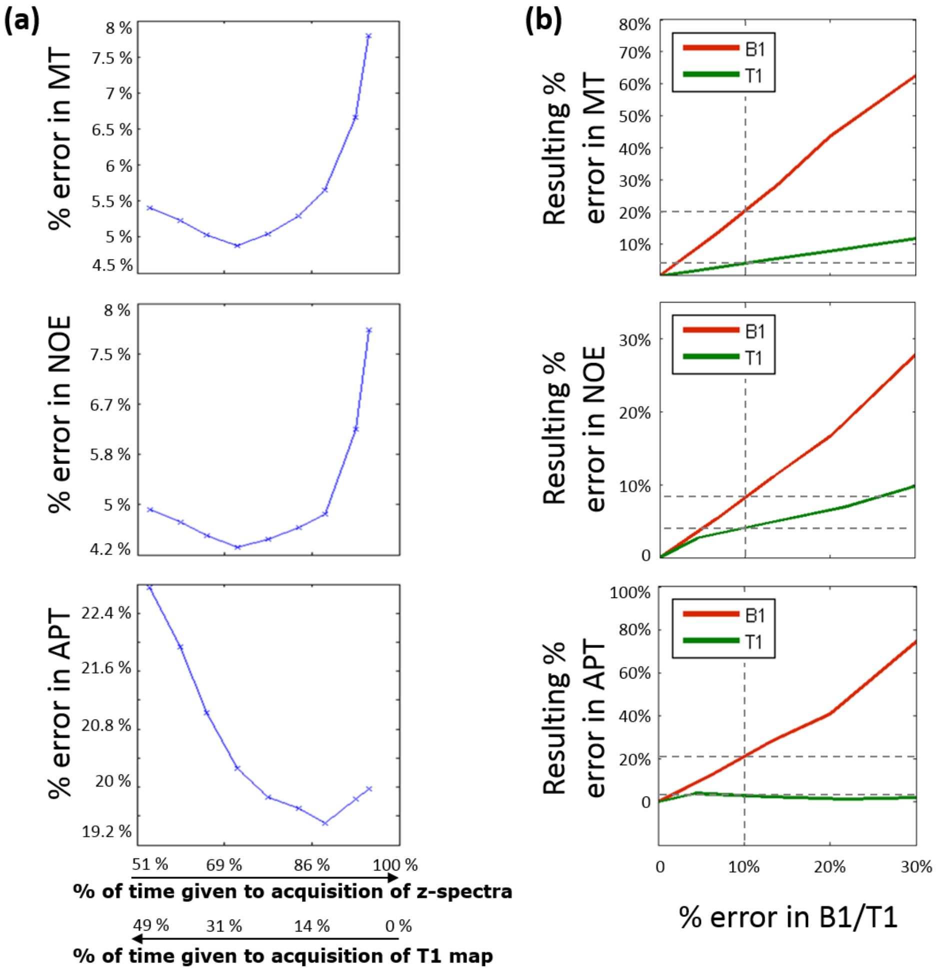

Figure 4.4: **(a)** Percentage error in MT (assuming $M_0^b = 10\%$), NOE ($M_0^n = 6\%$) and APT ($M_0^c = 0.25\%$) fitted for varying noise in the T_1 and *z-spectra* maps as indicated by the % of time given to acquisition of the *z-spectra* or T_1 map. The simulation was done using all three powers. **(b)** Sensitivity analysis on the effects of T_1 and B_1 error on MT, NOE and APT. The dotted lines show the effects a 10% error in B_1 / T_1 (red/green) has on MT, NOE and APT (the results were close to symmetric for positive and negative changes in B_1 and T_1).

Figure 4.4b shows the systematic errors in estimated values of MT, NOE and APT caused by errors in the assumed values of B_1 and T_1. A 5% error in B_1 results in 10% error in MT, 5% error in NOE and 10% error in APT, whereas a 10% error in T_1 results in errors in MT, NOE or APT of <5%. This highlights the requirement for accurate B_1 knowledge when fitting *z-spectra*.

Table 4.3: Comparison of quantitative results for the inter-subject and intra-subject studies.

		$\mathbf{M_0^b}$	$\mathbf{M_0^n}$	$\mathbf{M_0^c}$
Inter-subject variability in 10 subjects (mean and standard deviation in mean across subjects, Figure 4.6)	LUT pool size for WM	8.9 ±0.3%	5.0 ±0.1%	0.21 ±0.03%
	LUT pool size for GM	4.4 ±0.4%	3.0 ±0.1%	0.20 ±0.02%
	Standardised difference GM/WM, LUT fit	7.8	7	0.07
	Standardised difference GM/WM, Lorentzian fit	3.8	0.9	-0.03
	Standardised difference GM/WM, Asymmetry measure at 3.5ppm		0.43	
Intra-subject repeatability in 3 subjects (Figure 4.7)	Average standard deviation in pool size (pool size in %), averaged over voxels and subjects (from LUT method)	1.55%	0.61%	0.07%

4.4.2 Experimental results

The fit took 10.5 minutes for 274000 voxels typically contained in a mask on a dual core 3.3GHz Intel Core i3-3220 processor. Figure 4.5a shows MT, NOE and APT maps produced by fitting data acquired on a healthy volunteer and the B_1 map used in the fit, and Figure 4.5d shows the fitted spectra from a single WM voxel. Figure 4.5 also compares the results of the fitting when including prior information from a separately acquired B_1 map (Figure 4.5a) or fitting the *z-spectra* for MT, NOE, APT and the B_1 scaling factor together (Figure 4.5b). The difference between the two is shown in Figure 4.5c. There is reasonable agreement between the MT, NOE and APT maps produced by both fits and between the fitted and separately measured B_1 map, although there is some mixing of information between the fitted value of B_1 scale and MT as can be seen in the grey matter sulci.

Figure 4.6a shows the average grey and white matter pool sizes for 10 healthy subjects fitted using the LUT approach assuming prior information from B_1 and T_1 maps. Figure 4.6b shows the results of the same data analysed using B_1-corrected Lorentzian fitting[28]. Figure 4.6c shows asymmetry analysis computed at 3.5ppm. Standardised difference[33] between WM and GM was calculated for each pool, together with Coefficient of Variation (CV). Table 4.3 summarizes the quantitative results.

The intra-subject reproducibility results are also shown in Table 4.3 and in Figure 4.7, with the error bars indicating the standard deviation across the voxels within the ROIs.

4.5 Discussion

This study has presented a novel method of deriving quantitative CEST information from any pulse sequence, using a numerically derived database of possible *z-spectra* tailored to the acquisition protocol, and taking account of variations in RF amplitude and T_1. A Monte Carlo simulation was used to investigate the sensitivity of the results to different acquisition protocols and errors in the estimates of B_1 and T_1. The procedure was used to estimate *z-spectrum* parameters using data acquired from ten healthy subjects with intra-subject reproducibility being assessed in a further three subjects. The results indicated that this method could be used for reliable detection of the MT and NOE pools in the white and grey matter of a healthy brain.

Figure 4.6 shows the results of the inter-subject repeatability study, (mean and standard deviation over the whole WM or GM: standard error would be two orders of magnitude smaller) and demonstrates that the estimated parameters are reasonably consistent between subjects. The results from asymmetry analysis at 7T are hard to interpret as there are multiple effects contributing to the resulting metric. For this reason asymmetry analysis is unsuitable at high fields (>3T) and the results presented here show that asymmetry analysis is less sensitive than more quantitative metrics. The reproducibility study (Figure 4.7 - averaging over small ROIs in the corpus callosum) indicates that inter-subject variation is dominated by differences between individuals rather than measurement noise. This data will provide normative information for future studies.

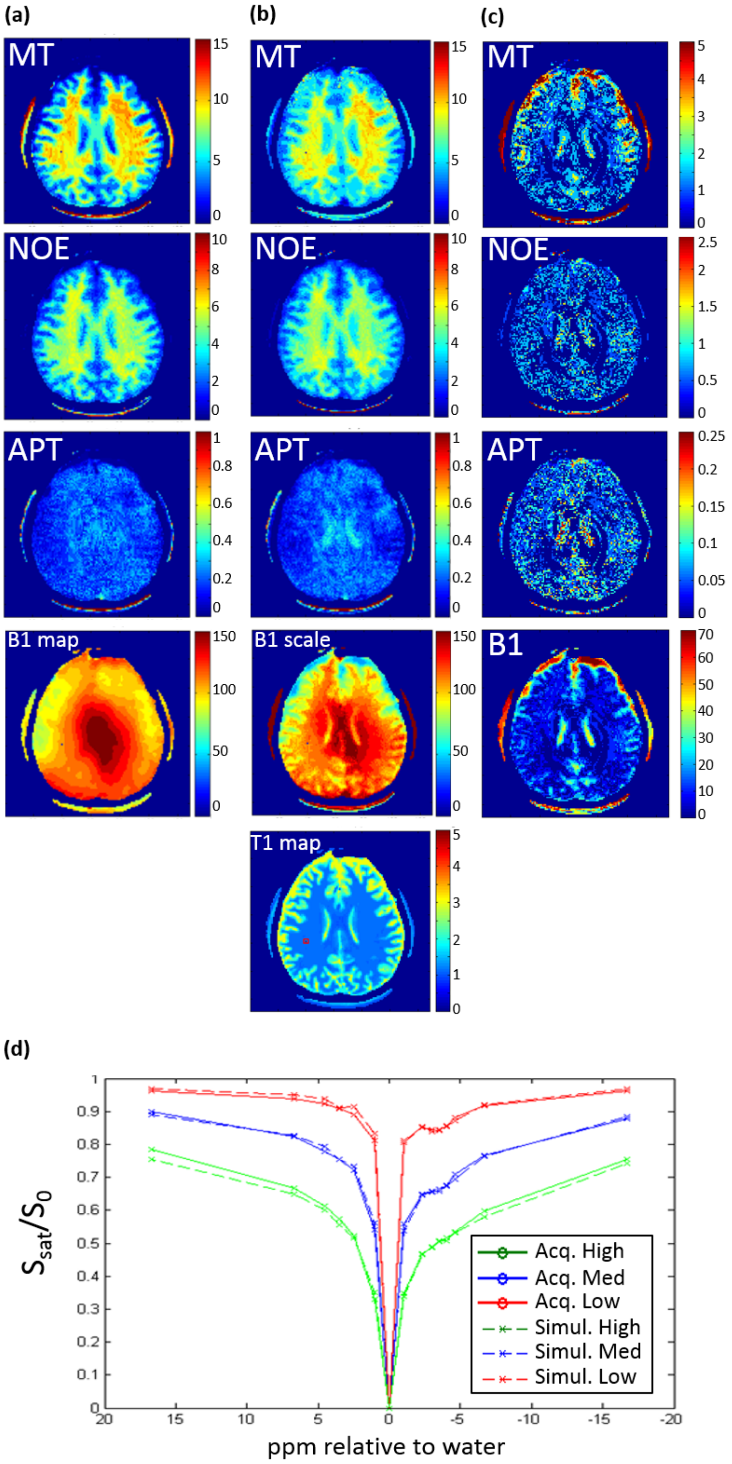

Figure 4.5: MT, NOE and APT maps resulting from the fit. **(a)** shows the results when fitting using a priori knowledge of B_1 taken from the separately acquired B_1 map shown at the bottom of the column. **(b)** shows the results when also fitting for B_1 (without a priori B_1 knowledge - results shown as the $B_{1,scale}$ map). The colormap range for all maps represents the range of simulated spectra, in concentration percentage. **(c)** shows the difference between **(a)** and **(b)**. Below the three columns, a separately acquired T_1 map that was also used in the fit is shown. **(d)** Shows the spectrum from a single voxel in the red ROI shown in the T_1 map or indicated by the black dots in B_1 and MT maps. The solid lines in the spectra show in-vivo spectra and the dotted lines show the fitted simulated spectra.

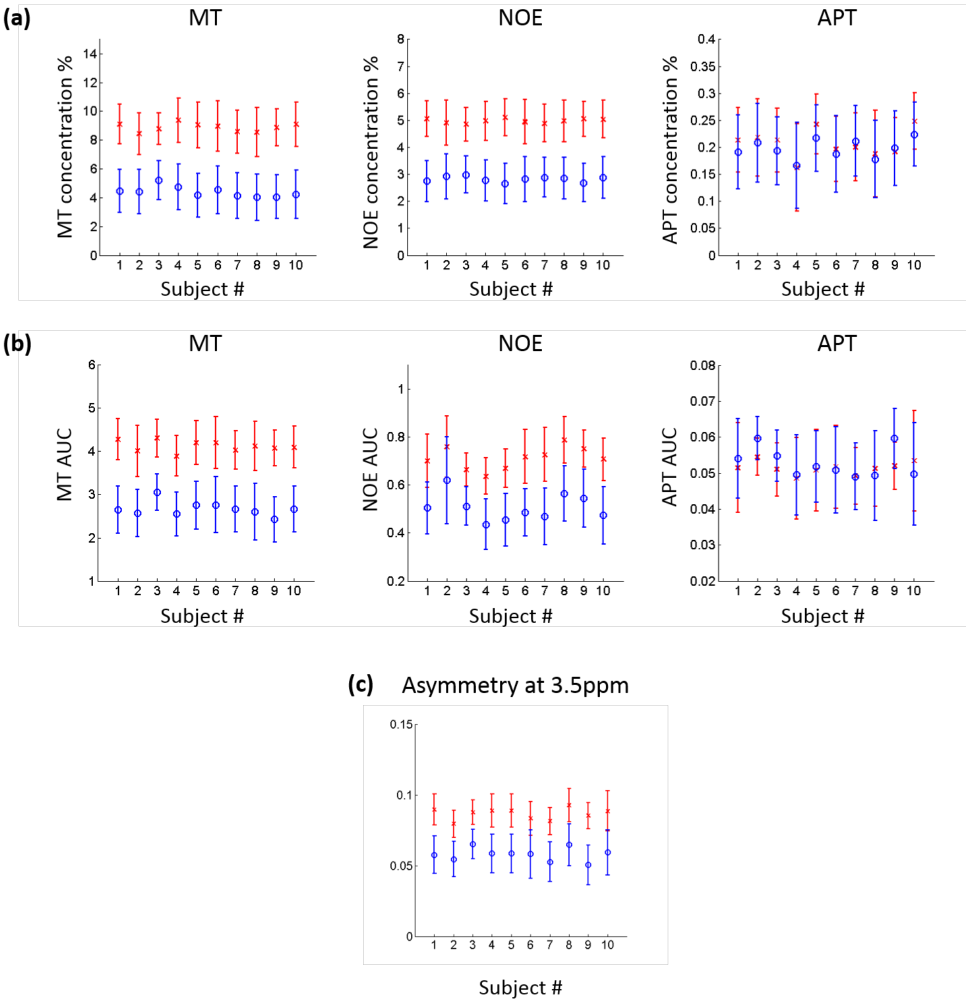

Figure 4.6: (a) Mean and standard deviation of MT, NOE and APT values from WM (red) and GM (blue) masks for ten healthy subjects. (b) B_1 corrected Lorentzian fitted Mean and standard deviation of MT, NOE and APT from the same WM and GM masks. In Lorentzian fitting, the pools are quantified as the AUC of each fitted curve. (c) Asymmetry at 3.5ppm.

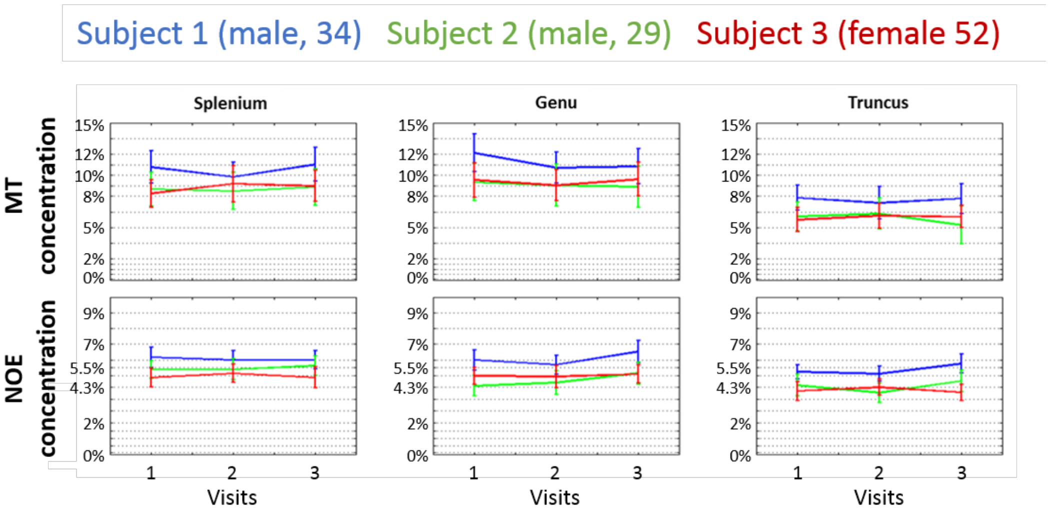

Figure 4.7: Intra-subject reproducibility for three ROIs in the Corpus Callosum. MT and NOE proton pool concentration (mean % pool size with standard deviation across ROI) results are shown for three subjects. Y-axis shows proton pool concentration.

As reported elsewhere, the APT pool was found to be very small in the healthy brain but it is elevated in various pathologies, and it was too small to be detected reliability in the GM of these healthy subjects. However the sequence used here could be better optimized for APT, for instance by acquiring data only at lower power and by better sampling the APT *z-spectrum* peak. In this work we assumed an APT exchange rate from previous in-vivo measurements[12] and our own full fit to Bloch McConnell equations, although lower values are often assumed[32]. Using a lower value in the simulations would have increased the measured pool size. The APT peak is also very close to the amine peak at 1.8 ppm, which is thought to be in fast exchange (>1000 s^{-1}[32]) and, in common with many studies of APT, it is possible that these APT measures will have been contaminated by amines.

The LUT approach has various advantages over current quantification methods. Our approach is fully quantitative, simple, time efficient, and allows simultaneous fitting of multiple parameters and overlapping peaks (even NOE and APT overlap due to the short T_2 of the NOE). However the method has some limitations. The LUT is initially computationally intensive to calculate, although it can be expanded post hoc to incorporate other sequences. The fitted values are restricted to the exact simulated ones, but further precision can be achieved by simulation of more values or interpolation between values. A further refinement would be to use more advanced interpolation methods based on the physical relationship between CEST effects and RF amplitude[30]. Similarly, in this study regions with B_0 shift above 200Hz were not analysed since such spectra had not been included in the data base, but alternatively the B_0 shift could be included in the simulated database.

The LUT currently assumes constant exchange rate parameters, which can have a similar effect on the *z-spectrum* as pool concentration, and which are sensitive to pH which can change in pathology. The effects of exchange rate and concentration could be separated by increasing the dimensions of the LUT to include more acquisition parameters like pulse duration and duty cycle. Similarly it could be extended to include more pools and different relaxation times for each pool. These extensions would likely require the data acquisition to be tuned to give sensitivity to the parameters of interest.

WM and GM masks were aggressively thresholded to avoid partial volume errors, and the MT and NOE results showed very good WM/GM separation (Figure 4.6a) and also variation across WM (Figure 4.7). It is interesting to note that the NOE and MT values appear to be uncoupled in the corpus callosum, with the MT:NOE ratio varying between the truncus and the splenium and genu. Previous work has suggested that the truncus and genus have more myelinated axons than the splenium[22], so this may indicate a difference in sensitivity of the NOE and MT signals to myelination, or alternatively this result may relate to the previously reported dependence of MT on fibre orientation[18]. In practice a small positive APT pool was measured in all GM and WM ROIs. However given that the fit is based on a database of realistic spectra, no negative results are possible, which will bias the results at low signal (the noise distribution is likely to be Rician).

Previously reported Macromolecular pool concentrations for healthy WM range from 10%[16,34] to 15%[21] or higher[4], but assume different models and different physical parameters for the different pools. Two pool models[4,11,21] tend to overestimate the macromolecular pool concentration by effectively including the NOE pool. A previous study[12] that used a four pool model (free water, MT, NOE and APT) found somewhat lower MT and NOE pool concentrations of 6.2% and 2.4% in WM, assuming different values of T_1^b, T_2 and exchange rates for the MT and NOE pools and a Lorentzian lineshape for the bound pool. The same study measured an APT WM pool size of 0.22% which is comparable to that measured here. The results depend on how physically realistic the model is. A recent study[38] has suggested that aromatic NOE signals underlie the APT peak. Further work is required to determine whether this can be separated from APT, for instance by making assumptions about the fraction of the NOE signals.

The sensitivity of the new LUT method is highlighted by the standardized difference between GM and WM for all pool size estimates (Table 4.3) which were considerably larger than for the semi-quantitative Lorentzian fitting, even taking account of B_1 variations in Lorentzian fitting method. The intra-subject variability (Figure 4.7, measured in 500 voxels) was somewhat higher than that predicted from the Monte Carlo results (Figure 4.3). There are several potential reasons for these differences. In terms of systematic differences, firstly the T_1s included in the simulations for the LUT were not long enough to model CSF and secondly flow may have modified the effect of the saturation. Thirdly any errors in other fitted parameters may have led to changes in B_1 being interpreted as change in MT due to the similarity of their effects on the spectra. There is some evidence for this in Figure 4.5 where the difference between the maps calculated by fitting B_1 and using a B_1 map is particularly obvious in regions of low B_1 in the frontal lobes. This problem could be addressed by extending the LUT to lower powers. In terms of random errors, the B_1 scaling factor was generally less than 100%, i.e. the LUT contained spectra simulated at higher power than that achieved experimentally. Furthermore the fit assumed that the B_1 scaling factor was constant across all scans on a particular subject, but we could use the scanner RF drive scale to correct for unexpected changes in RF output. We also showed that the most robust results were achieved by acquiring a separate T_1 map rather than fitting the *z-spectra* for T_1 (Figure 4.4).

The simulations indicate that acquiring data at three coupled RF powers can result in a fit that is robust across different pools, whereas if sensitivity to only one particular pool is required, then fewer powers should be used. However this assumes that the RF power is completely predictable and known prior to the experiment, where as in practice inhomogeneities in the RF field, or variations in the adjustment of the RF amplitude are likely at 7T. Combined with the strong dependence of the results on RF power (confirmed in Figure 4.4b), this suggests that acquiring spectra at a range of powers will reduce the risk of not being at the optimum power for any given pool. The method is sufficiently robust for the B_1 scaling factor to be fitted directly from the *z-spectra* without acquiring a B_1 map (Figure 4.5b), and Monte Carlo simulations suggested that this might be an optimal approach (results not shown) but in practice it was found to be unstable (e.g. GM contrast in the fitted B_1 scaling map). This suggests that the T_2 or exchange rates assumed for the MT pool may not be correct in all locations. The LUT approach can be extended to measure these parameters provided the sequence is adapted to provide sensitivity to them (for example by varying the inter-pulse interval in the saturation[30,31]).

4.6 Conclusions

Quantifying proton pool concentrations from *z-spectrum* data has proved to be challenging. Data from steady state sequences can be fitted to analytical expressions but non-steady-state sequences have advantages in terms of sensitivity[9], SAR and flexibility in the saturation to provide sensitivity to the T_2 of the bound pool and exchange rate. Methods that model the spectra as a sum of Lorentzian lines neglect the nonlinear effect of overlapping contributions to the *z-spectrum*, and it is too computationally expensive to fit the full numerical model to the spectra. This study presents a new method of fitting data from non-steady-state sequences in a feasible computational time by comparing *z-spectra* to a LUT using a priori knowledge of B_1 scaling and T_1. This gave reproducible results in healthy controls, with WM values for M_0^b, M_0^n and M_0^c varying between 7% – 11%, 4% – 6% and 0.1% - 0.3% respectively, and GM values ranging between 3% - 6.5%, 1.8% – 3.5% and 0.1% - 0.3%. The LUT is being extended to include the range of parameters expected in pathology or in other tissue. It could also be extended to fit for the T_2s or exchange rates if experiments were designed to provide sensitivity to these parameters.

4.7 Summary

The method presented in this chapter has been successful at providing fully quantitative results with greater reliability than existing methods. This new method also has the advantage of being study-specific, meaning it can be designed and adjusted to different studies if for example more sensitivity should be given to the APT region, or probing exchange rates between proton pools instead of proton pool concentrations. Repeatability of the method has also been successfully tested, providing very reliable results and forming a strong basis for longitudinal observation of MT and CEST effects. The next chapter of this thesis presents various applications of this method, including a longitudinal MS study.

Bibliography

[1] R G Bryant. The Dynamics of Water-Protein Interactions. *Annual Review of Biophysics and Biomolecular Structure*, 25(1):29–52, jan 1996.

[2] Michael A. Chappell, Manus J. Donahue, Yee Kai Tee, Alexandre A. Khrapitchev, Nicola R. Sibson, Peter Jezzard, and Stephen J. Payne. Quantitative Bayesian model-based analysis of amide proton transfer MRI. *Magnetic Resonance in Medicine*, 70(2):556–567, 2013.

[3] Kimberly L. Desmond and Greg J. Stanisz. Understanding quantitative pulsed CEST in the presence of MT. *Magnetic Resonance in Medicine*, 67 (4):979–990, 2012.

[4] Richard D Dortch, Jay Moore, Ke Li, Marcin Jankiewicz, Daniel F Gochberg, Jane a Hirtle, John C Gore, and Seth a Smith. Quantitative magnetization transfer imaging of human brain at 7 T. *NeuroImage*, 64: 640–9, 2013.

[5] Adrienne N. Dula, Lori R. Arlinghaus, Richard D. Dortch, Blake E. Dewey, Jennifer G. Whisenant, Gregory D. Ayers, Thomas E. Yankeelov, and Seth A. Smith. Amide proton transfer imaging of the breast at 3 T: Establishing reproducibility and possible feasibility assessing chemotherapy response. *Magnetic Resonance in Medicine*, 70(1):216–224, 2013.

[6] V Guivel-Scharen, T Sinnwell, S D Wolff, and R S Balaban. Detection of proton chemical exchange between metabolites and water in biological tissues. *Journal of Magnetic Resonance*, 133(1):36–45, 1998.

[7] Mark Jenkinson, Christian F. Beckmann, Timothy E.J. Behrens, Mark W. Woolrich, and Stephen M. Smith. FSL. *NeuroImage*, 62(2):782–790, 2012.

[8] Craig K. Jones, Daniel Polders, Jun Hua, He Zhu, Hans J. Hoogduin, Jinyuan Zhou, Peter Luijten, and Peter C M Van Zijl. In vivo three-dimensional whole-brain pulsed steady-state chemical exchange saturation transfer at 7 T. *Magnetic Resonance in Medicine*, 67(6):1579–1589, 2012.

[9] Vitaliy Khlebnikov, Nicolas Geades, Dennis W. J. Klomp, Hans Hoogduin, Penny Gowland, and Olivier Mougin. Comparison of pulsed three-dimensional CEST acquisition schemes at 7 tesla: steady state versus pseudosteady state. *Magnetic Resonance in Medicine*, jul 2016.

[10] Jae Seung Lee, Ravinder R. Regatte, and Alexej Jerschow. Isolating chemical exchange saturation transfer contrast from magnetization transfer asymmetry under two-frequency rf irradiation. *Journal of Magnetic Resonance*, 215: 56–63, 2011.

[11] Ives R. Levesque, Paul S. Giacomini, Sridar Narayanan, Luciana T. Ribeiro, John G. Sled, Doug L. Arnold, and G. Bruce Pike. Quantitative magnetization transfer and myelin water imaging of the evolution of acute multiple sclerosis lesions. *Magnetic Resonance in Medicine*, 63:633–640, 2010.

[12] Dapeng Liu, Jinyuan Zhou, Rong Xue, Zhentao Zuo, Jing An, and Danny J J Wang. Quantitative characterization of nuclear overhauser enhancement and amide proton transfer effects in the human brain at 7 Tesla. *Magnetic Resonance in Medicine*, 70(4):1070–1081, 2013.

[13] Dan Ma, Vikas Gulani, Nicole Seiberlich, Kecheng Liu, Jeffrey L. Sunshine, Jeffrey L. Duerk, and Mark A. Griswold. Magnetic resonance fingerprinting. *Nature*, 495(7440):187–192, 2013.

[14] Jan-Eric Meissner, Steffen Goerke, Eugenia Rerich, Karel D Klika, Alexander Radbruch, Mark E Ladd, Peter Bachert, and Moritz Zaiss. Quantitative pulsed CEST-MRI using Ω-plots. *NMR in biomedicine*, 28(10):1196–208, oct 2015.

[15] Clare Morrison and R. Mark Henkelman. A Model for Magnetization Transfer in Tissues. *Magnetic Resonance in Medicine*, 33(4):475–482, apr 1995.

[16] O E Mougin, R C Coxon, A Pitiot, and P a Gowland. Magnetization transfer phenomenon in the human brain at 7 T. *NeuroImage*, 49(1):272–81, 2010.

[17] Olivier Mougin, Matthew Clemence, Andrew Peters, Alain Pitiot, and Penny Gowland. High-resolution imaging of magnetisation transfer and nuclear Overhauser effect in the human visual cortex at 7 T. *NMR in Biomedicine*, 26(11):1508–1517, 2013.

[18] André Pampel, Dirk K Müller, Alfred Anwander, Henrik Marschner, and Harald E Möller. Orientation dependence of magnetization transfer parameters in human white matter. *NeuroImage*, 114:136–46, jul 2015.

[19] D William Penny, J Karl Friston, T John Ashburner, J Stefan Kiebel, and E Thomas Nichols. *Statistical parametric mapping: the analysis of functional brain images: the analysis of functional brain images.* 2011. ISBN 0080466508.

[20] A. Ramani, C. Dalton, D. H. Miller, P. S. Tofts, and G. J. Barker. Precise estimate of fundamental in-vivo MT parameters in human brain in clinically feasible times. *Magnetic Resonance Imaging*, 20(10):721–731, 2002.

[21] Stefan Ropele, Thomas Seifert, Christian Enzinger, and Franz Fazekas. Method for quantitative imaging of the macromolecular 1H fraction in tissues. *Magnetic Resonance in Medicine*, 49(5):864–871, 2003.

[22] Mustafa F Sargon, H Hamdi Celik, M Doğan Aksit, and Ergün Karaağaoğlu. Quantitative analysis of myelinated axons of corpus callosum in the human brain. *The International journal of neuroscience*, 117(6):749–755, 2007.

[23] Rachel Scheidegger, Elena Vinogradov, and David C. Alsop. Amide proton transfer imaging with improved robustness to magnetic field inhomogeneity and magnetization transfer asymmetry using saturation with frequency alternating RF irradiation. *Magnetic Resonance in Medicine*, 66(5):1275–1285, 2011.

[24] J G Sled and G B Pike. Quantitative imaging of magnetization transfer exchange and relaxation properties in vivo using MRI. *Magnetic resonance in medicine*, 46(5):923–31, nov 2001.

[25] Phillip Zhe Sun and A. Gregory Sorensen. Imaging pH using the chemical exchange saturation transfer (CEST) MRI: Correction of concomitant RF irradiation effects to quantify cest MRI for chemical exchange rate and pH. *Magnetic Resonance in Medicine*, 60(2):390–397, 2008.

[26] Peter C M van Zijl and Nirbhay N Yadav. Chemical exchange saturation transfer (CEST): What is in a name and what isn't? *Magnetic Resonance in Medicine*, 65(4):927–948, apr 2011.

[27] Michael J Wilhelm, Henry H Ong, and Felix W Wehrli. Super-Lorentzian framework for investigation of T2* distribution in myelin. In *Ismrm*, 2012.

[28] Johannes Windschuh, Moritz Zaiss, Jan Eric Meissner, Daniel Paech, Alexander Radbruch, Mark E. Ladd, and Peter Bachert. Correction of B1-inhomogeneities for relaxation-compensated CEST imaging at 7T. *NMR in Biomedicine*, 28(5):529–537, 2015.

[29] Donald E. Woessner, Shanrong Zhang, Matthew E. Merritt, and A. Dean Sherry. Numerical solution of the Bloch equations provides insights into the optimum design of PARACEST agents for MRI. *Magnetic Resonance in Medicine*, 53(4):790–799, 2005.

[30] Jiadi Xu, Nirbhay N. Yadav, Amnon Bar-Shir, Craig K. Jones, Kannie W Y Chan, Jiangyang Zhang, P. Walczak, Michael T. McMahon, and Peter C M Van Zijl. Variable delay multi-pulse train for fast chemical exchange saturation transfer and relayed-nuclear overhauser enhancement MRI. *Magnetic Resonance in Medicine*, 71(5):1798–1812, 2014.

[31] Jiadi Xu, Kannie W Y Chan, Xiang Xu, Nirbhay Yadav, Guanshu Liu, and Peter C M van Zijl. On-resonance variable delay multipulse scheme for imaging of fast-exchanging protons and semisolid macromolecules. *Magnetic Resonance in Medicine*, pages n/a–n/a, 2016.

[32] Xiang Xu, Nirbhay N. Yadav, Haifeng Zeng, Craig K. Jones, Jinyuan Zhou, Peter C M van Zijl, and Jiadi Xu. Magnetization transfer contrast-

suppressed imaging of amide proton transfer and relayed nuclear overhauser enhancement chemical exchange saturation transfer effects in the human brain at 7T. *Magnetic Resonance in Medicine*, 75(1):88–96, jan 2016.

[33] Dongsheng Yang and Jarrod Dalton. A unified approach to measuring the effect size between two groups using SAS®. *SAS Global Forum 2012*, page Paper 335, 2012.

[34] Thomas E Yankeelov, David R Pickens, and Ronald R Price. *Quantitative MRI in Cancer*. 2012. ISBN 9781439804360.

[35] Moritz Zaiss and Peter Bachert. Chemical exchange saturation transfer (CEST) and MR Z-spectroscopy in vivo: a review of theoretical approaches and methods. *Physics in medicine and biology*, 58(22):R221–69, 2013.

[36] Moritz Zaiss, Benjamin Schmitt, and Peter Bachert. Quantitative separation of CEST effect from magnetization transfer and spillover effects by Lorentzian-line-fit analysis of z-spectra. *Journal of Magnetic Resonance*, 211 (2):149–155, 2011.

[37] Moritz Zaiss, Junzhong Xu, Steffen Goerke, Imad S. Khan, Robert J. Singer, John C. Gore, Daniel F. Gochberg, and Peter Bachert. Inverse Z-spectrum analysis for spillover-, MT-, and T1-corrected steady-state pulsed CEST-MRI - application to pH-weighted MRI of acute stroke. *NMR in Biomedicine*, 27(3):240–252, 2014.

[38] Moritz Zaiss, Johannes Windschuh, Steffen Goerke, Daniel Paech, Jan-Eric Meissner, Sina Burth, Philipp Kickingereder, Wolfgang Wick, Martin Bendszus, Heinz-Peter Schlemmer, Mark E Ladd, Peter Bachert, and Alexander Radbruch. Downfield-NOE-suppressed amide-CEST-MRI at 7 Tesla provides a unique contrast in human glioblastoma. *Magnetic resonance in medicine*, jan 2016.

[39] Jinyuan Zhou, Jean-Francois Payen, David A Wilson, Richard J Traystman, and Peter C M van Zijl. Using the amide proton signals of intracellular

proteins and peptides to detect pH effects in MRI. *Nature medicine*, 9(8): 1085–90, aug 2003.

Chapter 5

Applications for Quantitative MT/CEST

5.1 Abstract

The previous chapter introduced a new method for *in-vivo* quantitative MT and CEST at 7T[11], providing reliable results between different subjects and within various repeats of the same subject. This chapter describes various applications of that method, from correlations between cortical MT and functional connectivity in the healthy brain[18] to APT imaging in Glioma and a longitudinal evaluation of lesion MT in a MS study. Comparisons to more conventional MT and CEST quantification methods like Lorentzian fitting and asymmetry analysis are shown when appropriate.

This chapter is split into five subsections, each presenting a different MT/CEST application. The first part describes how quantitative MT (qMT) can be used to track myelination in MS, the second and third subsections show the potentials and limitations of APT CEST in Glioma, and the the fourth and fifth subsections focus on correlations between MT, functional connectivity and NOE in the

healthy brain.

5.2 Introduction

MT and CEST can provide a vast variety of potential contrast mechanisms in MRI, especially when CEST agents are used. While several reviews discuss the use of CEST agents[15,39,41,53], this chapter presents *in-vivo* methods that take advantage of the available endogenous CEST agents and can be easily translated to the clinic. Clinical application requires thorough investigation of several issues, including patient comfort, limited scan time, scanning large organs and more importantly RF power deposition. Power deposition increases with field strength, imposing restrictions on what saturation schemes can be used in ultra-high field (7T) magnetization transfer experiments *in-vivo*. To stay within FDA-guided Specific Absorption Rate (SAR) limits, the 3D acquisition scheme described in the previous chapter[31] uses pulsed, pseudo-steady state saturation, at 50% duty cycle.

Because of its strong link to axon and myelin content[36], MT imaging has been extensively used to study several demyelinating diseases including MS[4,7,26], Optic Neuritis[23] (axonal loss but no demyelination) and Wallerian Degeneration[27], and also to enhance contrast in MR angiography[9]. CEST is a more recent methodology which has already found multiple applications. Not long after the original CEST paper[46], Zhou *et. al.*[55] showed that the amide protons of mobile proteins and peptides could be imaged indirectly via the water signal using CEST. This methodology was termed Amide Proton Transfer (APT) CEST and has been mainly used to image ischemia[40,55] and tumour grading in cancer[20,47,56]. This chapter presents work carried out in multiple groups, and my contribution is stated in the introduction of each section.

5.3 MT and NOE in Multiple Sclerosis

5.3.1 Introduction

In Multiple Sclerosis (MS), an abnormal immune system response produces inflammation in the central nervous system which causes damage to the underlying nerve fibre in the form of demyelination and axonal loss, manifesting in chronic multifocal sclerotic plaques. This process of demyelination can sometimes be partially or fully reversed, and the brain tissue appears to recover (remyelination). Furthermore, most lesions appear around the central ventricles of the brain and in the white matter, but cortical gray matter lesions are also possible.

The majority of MS cases begin with a single episode affecting one or several sites in the brain. Such cases are known as Clinically Isolated Syndrome (CIS) and do not always progress into MS. However, if a second demyelinating attack occurs the disease progresses into Relapsing Remitting (RR)MS, with new RRMS episodes occurring randomly, on average 1.5 times per year (see Figure 5.1). Recovery from an MS episode is seldom complete, leading to an accumulation of lesions and symptoms, and disease progression[5]. As the disease progresses, a high percentage (≈70%) of RRMS patients enter the Secondary Progressive (SP)MS phase[6], dominated by axonal loss, demyelination and atrophy of normal appearing white and gray matter, while the rate of new episodes and inflamatory demyelinating decreases[30]. In some cases (only around 20%) MS is progressive from onset, known as Primary Progressive (PP)MS[6].

Focal lesions have long been observed with MRI, for instance using the Fluid Attenuated Inversion Recovery (FLAIR) sequence, and previous studies have attempted to quantify the demyelination process with estimation of the macromolecular proton fraction[7] or qMT[26]. Recent advances in MT and CEST[11,50] have provided more robust methods of quantifying processes that are thought to be strongly linked to myelination, in particular MT and the Nuclear Overhauser Effect (NOE). This section describes a study designed to investigate the time course of MT and NOE content of MS lesions using the fully quantitative method described in Chapter 4, and whether lesion appearance can be predicted by MT. This study was designed by Matthew Cronin, Olivier Mougin, Amal Samaraweera, Penny Gowland and Nikos Evangelou. My contribution to this work included scanning, analysis of the MT data and producing longitudinal results.

5.3.2 Methods

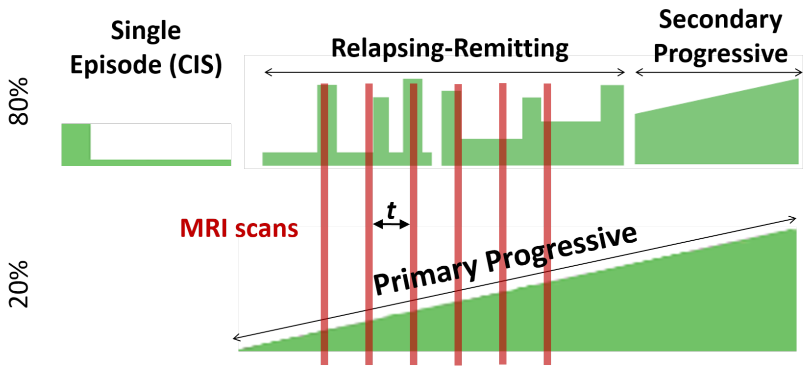

Figure 5.1: The different MS progression types and the design of the longitudinal study. There are six MRI scans, spaced $\boldsymbol{t} = 6$ weeks apart. Adjusted from[5].

With appropriate ethics approval, 4 patients (one male 23 years old, three female, 39, 35 and 27 years old) with Relapsing Remitting Multiple Sclerosis were scanned using a 7T Philips Achieva system with a 32-channel receiver coil. Each patient was scanned 6 times with 6 weeks between scans (30 weeks total, Figure 5.1). For each subject, *z-spectra* scans were acquired at 2 different B_1 saturation powers (0.33μT and 0.65μT) together with a high resolution Fluid-Attenuated Inversion Recovery (FLAIR) for accurate tracking of the lesions. The same 3D *z-spectra* acquisition scheme explained in the previous chapter was used for this study. A B_0 map (double echo method, FOV = 252 x 255 x $100mm^3$ at 3 x 3 x $2mm^3$ voxels) was acquired for B_0 correction (1min), along with a whole head

B_1 map (dual TR method, at 20ms and 120ms TR, FOV 205 x 180 x 132mm^3 at 3.2 x 4 x 4mm^3 voxels, 3 min) and a T_1 map (dual readout Phase-Sensitive Inversion Recovery (PSIR) data, FOV = 240 x 216 x 160mm^3 at 0.8mm isotropic resolution, SENSE factor [RL] of 2.2 and Foot-Head [FH] of 2, 10min).

Fitting The fitting process is the same as in Chapter 4 of this thesis and publication[11], with the exception of number of B_1 saturation powers scanned (2 sets of *z-spectra* scans instead of 3). For each subject visit, B_0 corrected *z-spectra* were fitted pixel-wise for the amplitude of 3 pools (MT, NOE and APT) relative to water, calculating the sum of squares difference between the measured spectra and the spectra in a database of Bloch simulated spectra. The B_1 and T_1 maps were used to limit the search to the corresponding values in the database, thereby applying B_1 and T_1 correction. FLAIR images were used to mask and track MS lesions.

5.3.3 Results

Figure 5.2 shows the MT, NOE and APT maps for one subject at visit 4. The lesion is indicated by the red arrows, showing lower proton pool concentrations and is visible in the low SNR APT image as well, while the periphery of the lesion shows an increase in APT. Figure 5.3 shows an example of an MS lesion that appears in visit 4 (same subject as in Figure 5.2) and gradually shrinks in the next two visits. Both MT and NOE ROI results show an initial reduction of signal followed by a slow and gradual increase of signal, indicating either remyelination or reduction of edema. This effect is seen in both the centre of the lesion (red ROI) and surrounding tissue (green ROI) which is also seen on the FLAIR image. The size of the core and periphery ROIs remained the same throughout the visits, showing that in this case the remyelination effect seen is partially caused by the lesion shrinking in size. Interestingly this MS lesion can be seen in the APT maps too (Figure 5.2), but none of the other lesions presented here (Figure 5.4) showed any change in APT signal.

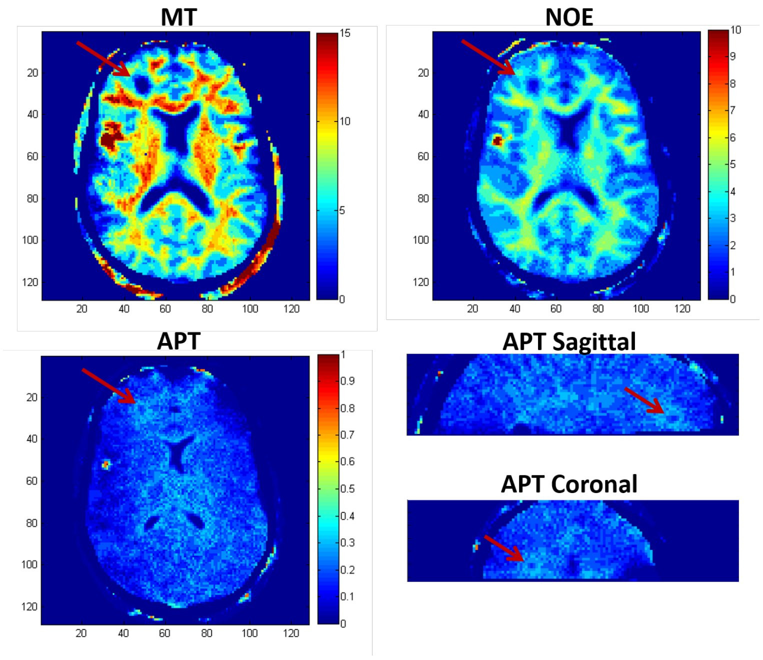

Figure 5.2: MT, NOE and APT maps showing the MS lesion (maps in proton pool %).

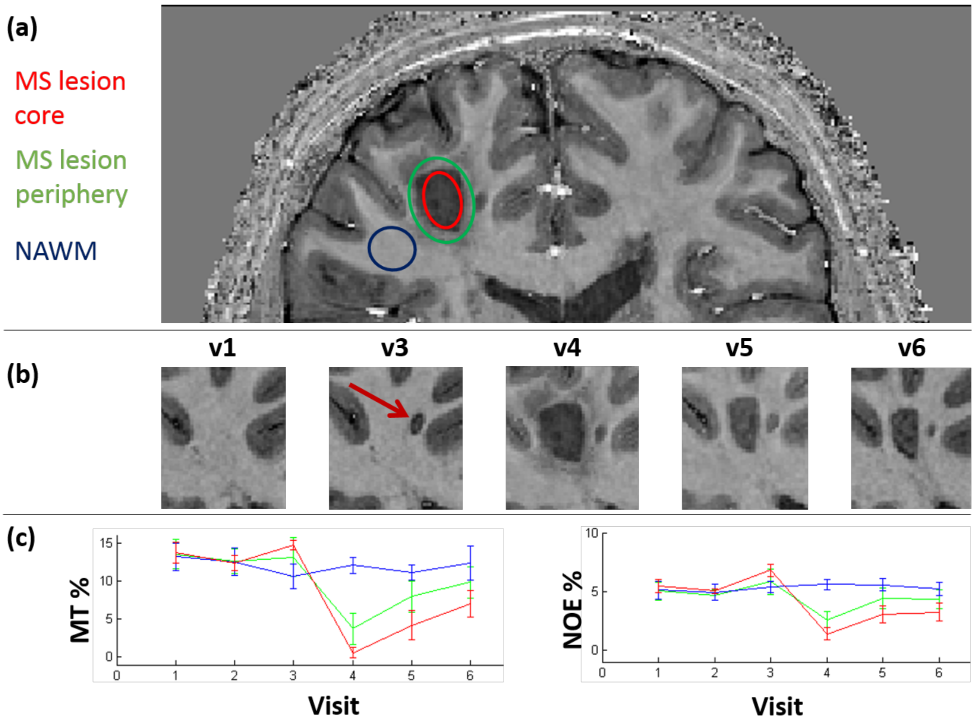

Figure 5.3: MS lesion evolution: quantification with MT and NOE. (a) MS lesion and NAWM ROIs. (b) PSIR images showing the evolution of the lesion. Visit 2 PSIR is missing due to patient movement. (c) Lesion vs. NAWM ROI fitting results for MT (left) and NOE (right). The green periphery ROI excludes any area from the red core ROI. Interestingly a second lesion appears between the gray matter and the main lesion just before the main lesion appears (red arrow). Size of ROIs remained constant throughout the visits.

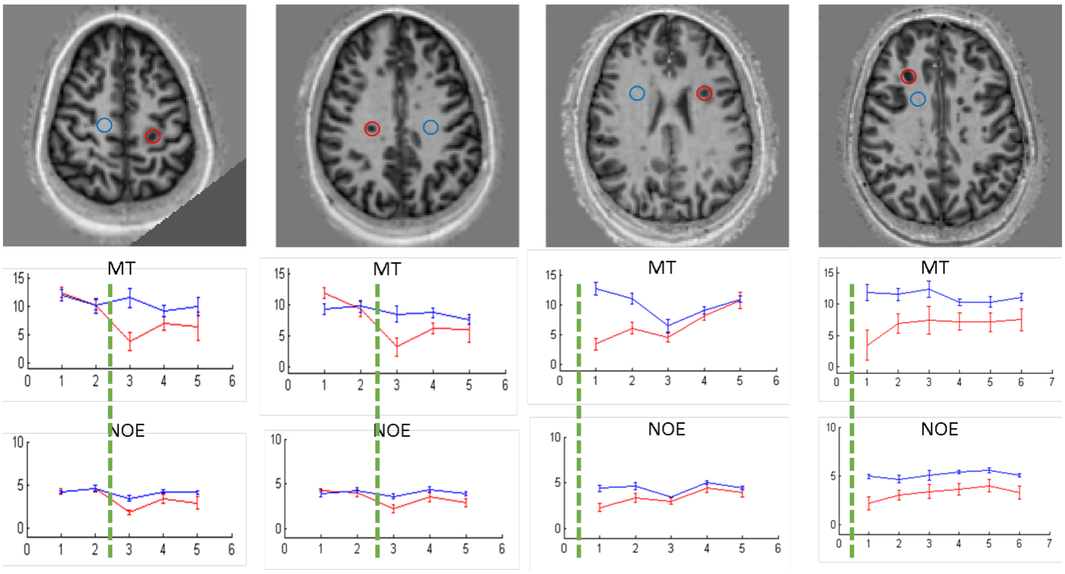

Figure 5.4: Four more examples of MS lesions. From left to right, the first two cases show demyelination, the third case shows remyelination and the fourth case shows no change in MT or NOE values, or myelin content. The dotted green lines indicate when the lesion appears: in the third and fourth cases the lesion was present from visit 1. Red indicates MS lesion and blue indicates NAWM.

Figure 5.4 shows four more examples of tracking MS with MT and NOE, showing cases of demyelination, remyelination and no change in MT or NOE. The first case (left column) shows a lesion that appears between visits 2 and 3. An initial drop of MT signal is observed, followed by a small increase in signal but no complete remyelination in the next 12 weeks. The second case shows the same, partial remyelination seen in case 1. In the third and fourth cases, the lesion was present in the first visit, hence appeared some time before the first visit, but the recovery of the two lesions is different. In the third case, the brain is seen to recover fully, with lesion MT and NOE returning to NAWM levels within the 30 week period, whereas in the fourth case the MT and NOE in the lesion remain consistently low.

Figure 5.5 shows an example of a lesion that covers both WM and GM areas, and the corresponding MT and NOE at each successive visit. The lesion gradually shrinks in the high resolution PSIR and FLAIR images, and both MT and NOE measures follow the same trend. This highlights the effectiveness of the quantification method, even in GM regions where baseline myelin content, MT and NOE

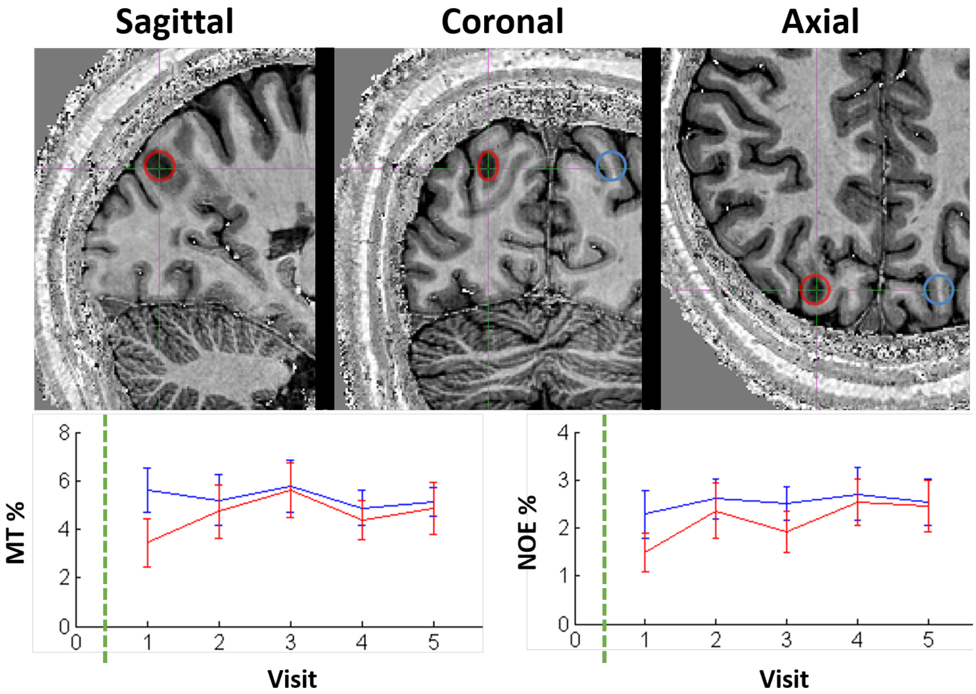

Figure 5.5: Tracking a GM lesion MT and NOE.

are lower.

5.3.4 Discussion

This study presents a method for tracking myelination in MS lesions in a fully quantitative way, with results suggesting both demyelination and remyelination processes. The intra-subject repeatability study in the previous chapter showed variation in MT up to 1.5%, and in NOE less than 1%. The same repeatability study was performed in NAWM regions in MS patients, showing even smaller variations in MT and NOE concentrations (less than 1.2% for MT and less than 0.5% for NOE). This gives confidence to the lesion ROI findings, where a difference of up to 10% is seen in MT, and up to 5% in NOE. The NOE signal consistently gives more stable proton pool concentration measures than MT, because it is less sensitive to variations in B_1, and should therefore be considered as a myelination marker. The APT SNR in this study was low because more time was given to acquiring MT and NOE frequencies that relate to myelination, giving APT data of insufficient quality for any meaningful study. The APT signal in Figure 5.3 however suggests that an APT study of MS lesions could be of interest. The third case in Figure 5.4 is of particular importance as it shows full remyelination of a lesion, although the NAWM MT and NOE values at visit 3 are also seen to decrease. A further investigation of the NAWM ROI showed a very small lesion appearing in that area, which already disappears in visit 4.

This study was designed with a 6 week interval between scans to track a lesion from formation to full recovery. The aim was to evaluate the quantitative methodology, as well as investigate the processes of demyelination and remyelination, and also to investigate the possibility of predicting a lesion site before it is visible in a T_2 -weighted FLAIR image. The study was able to capture and quantify lesions in very early stage of formation, where inflamation is still visible in the periphery of the lesion (Figure 5.3), as well as the processes of demyelination, partial and full remyelination (Figure 5.4).

5.3.5 Conclusions

The study was successful in providing quantitative information on the evolution of MS lesions in the form of MT and NOE proton pool concentrations. One of the aims of this study was the prediction of demyelinating lesions, or remyelination of lesions. While we were unable to make these predictions at the time of writing this thesis, the MT work presented is part of a larger study that includes more quantitative MR methodologies like Quantitative Susceptibility Mapping (QSM), Frequency Difference Mapping (FDM) and Diffusion Tensor Imaging (DTI) data. Future work includes looking at correlations between all the quantitative methodologies, and finding potential trends that can distinguish new lesions from old lesions, as well as lesion evolution.

5.4 Amide Proton Transfer (APT) in Glioma

5.4.1 Introduction

Gliomas are a type of brain tumour originating from glial cells like astrocytes, oligodendrocytes and microglia. The term is used to describe the different types of glial tumours like astrocytomas, oligodendrogliomas and glioblastomas, which can vary in aggressiveness and malignancy. The World Health Organization (WHO) grades Gliomas based on the type of glial cell they originate from, as well as malignancy, into four grades. Grade I are slow growing and benign tumours while grade II are considered low-grade Gliomas that grow slowly but can infiltrate nearby tissue and evolve into higher grade tumours. Grade III are malignant Gliomas that grow faster and more aggressively than grade II tumours, but slower than grade IV Gliomas (or glioblastomas) that are the most aggressive tumours that spread quickly and can affect multiple parts of the brain.

Despite advances in surgery, chemotherapy and radiation therapy, malignant Gliomas remain fatal with a median survival of 2-3 years for grade III and 12-15 months for grade IV tumours[14,34]. Grading of Gliomas is therefore vital for evaluating the disease and creating a treatment plan. The current gold standard for tumour grading is histopathology, where a sample is taken from the brain and examined under a microscope, however the heterogeneous nature of Gliomas complicates the procedure and can lead to false diagnosis. More recently, anatomical MRI scans like T_2-weighted images and FLAIR are beginning to help diagnosis and tumour grading by differentiating between edema and necrotic tissue[24]. Additionally, gadolinium enhanced T_1-weighted images can show blood-brain barrier disruption in tumours[10], although around 10% of glioblastoma cases show no gadolinium enhancement[38].

Amide Proton Transfer (APT) CEST has been linked to concentration of mobile proteins and peptides in tissue, and high APT signal can be seen in tumours[45]. APT CEST has already shown potential in differentiating radiation necrosis from tumour recurrence, and high grade (III and IV) from low grade (I and II) Gliomas[44,54,57], while a new study suggests the NOE signal may be more strongly correlated with tumour grading[17]. This study aims to assess the APT, as well as the NOE and MT signals as molecular markers of high-grade Glioma. Region-of-interest analysis was undertaken for solid Low Grade Glioma (LGG) and glioblastoma (GBM), necrotic and hemorrhagic cystic compartments, perifocal edema and contralateral control tissue. This study was designed by Olivier Mougin, Penny Gowland and Dorothy Auer before the start of my PhD. My contribution was in the analysis of the CEST data.

5.4.2 Methods

Subjects

The study protocol was approved by the local Research Ethics Committee, University and Hospital Trust research governance bodies. Seven patients (details in Table 5.1) with histologically proven cerebral high grade Glioma (GBM, WHO grade IV, n=4) or low grade Glioma (LGG, n=3 [one histologically confirmed]) were recruited from the neuro-oncology clinic at Queen's Medical Centre. The two presumed LGG cases did not undergo diagnostic biopsy due to typical MRI and clinical features including long-term clinical and radiological follow-up; specifically in both tumors mild volume increase and no sign of de-differentiation was observed for at least 2 years after the reference CEST studies. One of the GBM cases had multifocal disease resulting in 5 tumor regions for analysis. Another GBM had a previously diagnosed and low-grade lesion without significant radiological changes during surveillance, which was hence included in the total of 4 LGG lesions. Written informed consent was obtained from each participant. None of the participants had received any prior treatment at the time of the research scan.

Table 5.1: Sex, age, clinical, radiological and pathological diagnosis for each patient scanned at 7T.

Number	**Sex**	**Age**	**Clinical presentation/diagnosis**	**Radiological diagnosis including MRS results**	**Histology**
MS1	M	50	Dysphasia, hemianopia, headache while surveilled for presumed LGG	Left temporo-parietal high grade features with high lipids. De-differenitated multifocal Glioma	Glioblastoma, WHO grade IV, IDH1 staining is negative
MS2	M	56	Seizure	Left frontal, high grade features, only small area of enhancement	Diffuse Astrocytoma, some areas bland, but overall glioblastoma WHO grade IV
MS3	M	61	Weakness, headache	Right temporo-parietal and right thalamic , large aggressive appearing mass, large mobile lipids, high rCBV	Glioblastoma, WHO Astrocytoma Grade IV, IDH1-ve
MS4	F	67	Seizures	Right temporo-parietal, mobile lipids	Glioblastoma, WHO Astrocytoma Grade IV, IDH1-ve
MS5	F	46	Migraine (Incidental)	Left frontal	Oligodendroglioma, WHO grade II, IDH1+ve (R132H clone)
MS6	F	57	Tinnitus, hearing loss, Incidental presumed LGG	Left insula, low grade Glioma appearances with Choline elevation, 4 years f-u with mild increase in size	n.a.
MS7	M	39	Incidental presumed LGG (hearing loss)	Left insular/parietal, low grade possibly oligodendral appearances with choline elevation, >8 yrs f-u with mild increase	n.a.

Clinical protocol at 3T

Seven patients underwent routine radiological diagnostic multimodal MRI at 3T Philips Achieva as part of their clinical management. The clinical protocol included: T_2-FLAIR (TE = 140ms TI = 2750ms TR = 10000ms, voxel 0.9 x 0.9 x 3mm, pre and post Gd contrast T_1w MPRAGE (TE = 3.7ms TI = 960ms TR = 8.0ms, voxel 1 x 1 x 1mm), T_2w (TR = 3000ms, TE = 80ms, voxel 0.4 x 0.4 x 4mm, 1mm slice gap) and diffusion tensor images (16 directions, b = 1000s/mm^2, TE = 56.9ms TR = 8000ms, voxel 2 x 2 x 3mm). Diffusion measures were obtained after registration using FSL, and the average of the eigenvalues was used to produce mean diffusivity (MD) maps.

CEST protocol at 7T

All patients were scanned on a 7T Philips Achieva system equipped with a 32-channel receiver coil and a head only transmit coil. *Z-spectra* were acquired at high resolution across a 3D volume in less than 10 minutes using a 3D MT-TFE sequence[32] which consists of a train of off-resonance saturation pulses followed by a single shot, gradient echo readout. Data were acquired for saturation pulses applied at 24 offset frequencies chosen to adequately sample the NOE and APT peaks (frequencies in Hz of: - 2000; -1500, -1200, -1050, -900, -600, -300, 0, 300, 600, 900, 950, 975, 1000, 1025, 1050, 1075, 1100, 1125, 1150, 1200, 1300, 1500, 2000 and 50 000). The saturation train consisted of 30 saturation pulses applied in 1.8s with $B_{1rms} = 1.1\mu$T, this power being chosen to minimize the sensitivity of the APT signal to variations in B_1, making it possible to pool data between subjects. The imaging readout acquired 410 gradient echoes, TE/TR = 2.8/6ms, FOV = 192 x 186 x 50mm, 1.5mm isotropic voxel size, low-high spiral *k*-space acquisition for the phase encoding. The 3D volume acquisition required 4 repetitions of this cycle, giving an acquisition time of 20s per frequency offset and a total acquisition time of 8 minutes for the whole *z-spectrum*.

T_2^* weighted images were acquired (TE = 13.3ms TR = 732ms, voxel 0.29 x 0.29 x 1mm) and processed offline to produce Susceptibility Weighted Images (SWI), which were used to screen for hemorrhage and to anatomically delineate blood products related to the tumour mass. T_1 weighted MPRAGE images were also collected (TE = 3.7ms TR = 15ms, voxel 0.6 x 0.6 x 1mm). Finally B_0 maps (double echo method (TE = 6/6.5ms, TR = 200ms), FOV = 240 x 240 x 120mm^3 with a voxel resolution of 3 x 3 x 3mm^3) were acquired in 1:30 minute to correct for B_0 inhomogeneities.

Z-spectrum analysis

Two stage interpolation was used for B_0 correction to determine the exact frequency of the saturation. First the *z-spectrum* for each voxel was interpolated and shifted according to the acquired B_0 map. The average minimum of *z-spectra* from all pixels was calculated to estimate the average water frequency. The spectra from each voxel were then shifted to centre them on the average water frequency, and were interpolated to resample them at the original offset frequencies.

A four pool model (same as in Section 2.5.3) was then used to fit the *z-spectrum*. Each pool was modelled by a single Lorentzian of amplitude A_i, width W_i and centre frequency $\omega_{ref,i}$, with the four pools corresponding to free water, MT, NOE and APT. The total signal was modelled as the sum of these 4 pools:

$$L_{fit} = 1 - \sum_{i=1}^{4} A_i \left[1 + \left(\frac{\Delta\omega - \omega_{ref,i}}{0.5W_i} \right)^2 \right]^{-1} \tag{5.1}$$

Equation 5.1 was fitted to the experimental spectra by sum of square minimization (with the peak positions and widths restricted) giving the height (A_i as a fraction of water signal) and width (W_i) of each peak. Once a good fit had been achieved, the Area Under Curve (AUC) of each peak (in ppm) was calculated using trapezoidal integration. The resulting AUC for APT, MT and NOE is thus expressed in ppm multiplied by the height normalised to the water signal. This fit was performed on the *z-spectra* from each voxel or regions of interest. The standard asymmetry analysis was also performed by computing the MT ratio asymmetry MTR_{asym}, defined as:

$$MTR_{asym}(3.5ppm) = MTR(3.5ppm) - MTR(-3.5ppm) \tag{5.2}$$

Because *z-spectra* were only acquired at one B_1 saturation power, correcting the Lorentzian fitted results for B_1 was impossible. For a following study including B_1 and T_1 correction see the next section of this chapter.

ROI definitions

ROIs were manually drawn by a trained researcher under guidance of a senior neuroradiologist. Enhancing and necrotic tumor regions (only present in GBM) were manually outlined on the post Gd-T_1w 3T images using NeuROI[43]. Hemorrhagic regions were identified on the 7T SWI images. Peritumoral edema was identified based on clinical T_2-FLAIR as white matter hyperintensity remote from enhancing Glioma to avoid sampling of non-enhancing Glioma. In low–grade Gliomas, the tumor was defined as the hyperintense regions on the T_2-FLAIR images with no attempt made to differentiate edema from tumor. Secondary tumor masses were only included in APT ROI analysis if radiologically defined as typical LGG or GBM based on T_2, Gd enhancement and MD characteristics. The ROIs were drawn in various parts of the brain, susceptible to different levels of B_1 inhomogeneities at 7T. Since the fitting did not take account of B_1 errors, for each patient a control ROI was drawn in the contra-lateral part of the brain with similar B_1.

Due to the small number of patients, explorative statistics was performed by computing mean differences ±95% confidence interval (CI) for each tumour compartment, defined as the respective group average (and between subject standard deviation) of the difference of regional mean APT/MT/NOE signal of each tumour compartment and control ROI.

5.4.3 Results

Regional CEST changes in LGG and GBM: The mean APT, MT and NOE signals for the ROIs were averaged separately for LGG and GBM, and are summarized in Figure 5.6. The solid GBM tumor compartment including mainly Gd-enhancing regions and one partly enhancing mass, showed a significantly elevated APT signal compared to the control region (mean difference of 7.5, with CI at 95% of 2.2<12.8), with necrotic and hemorrhagic regions showing

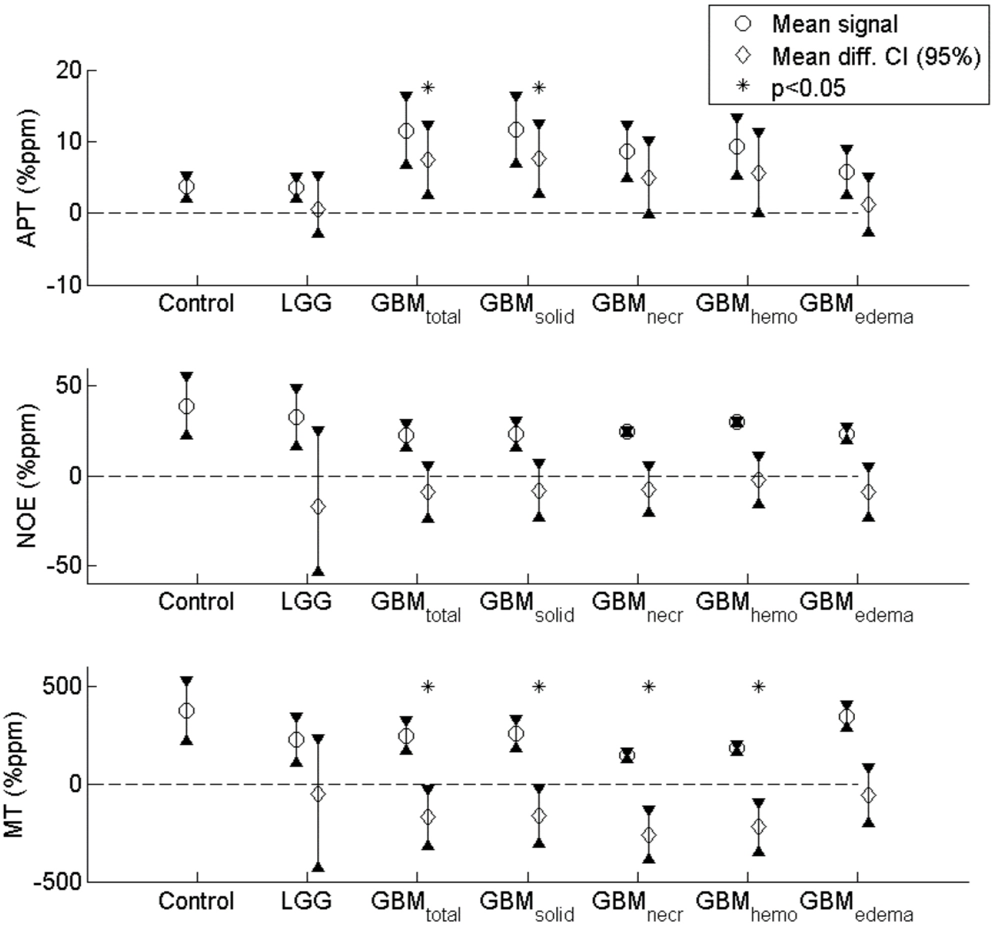

Figure 5.6: Regional APT, NOE and MT averaged over LGG, GBM, its subcomponents and edema expressed as mean and standard deviation. Also shown are the respective mean differences and 95% confidence intervals (CI) compared with controls.

similar trends (mean difference of 5.0 and 5.7, with CI of -0.5<10.5 and -0.3<11.7 respectively). No difference was found between the perifocal edema (only found in GBM) and control ROIs (mean difference of 1.2, CI of -3.1<5.5), nor between LGG and control ROI (mean difference of 1.1, CI of -4.3<6.5). The MT signal was significantly reduced in all GBM compartments, while NOE was not significantly changed in any region.

Comparison with MTR asymmetry-derived APT weighted signal: Figure 5.7 shows the MT, NOE, APT maps produced by fitting the *z-spectra* with

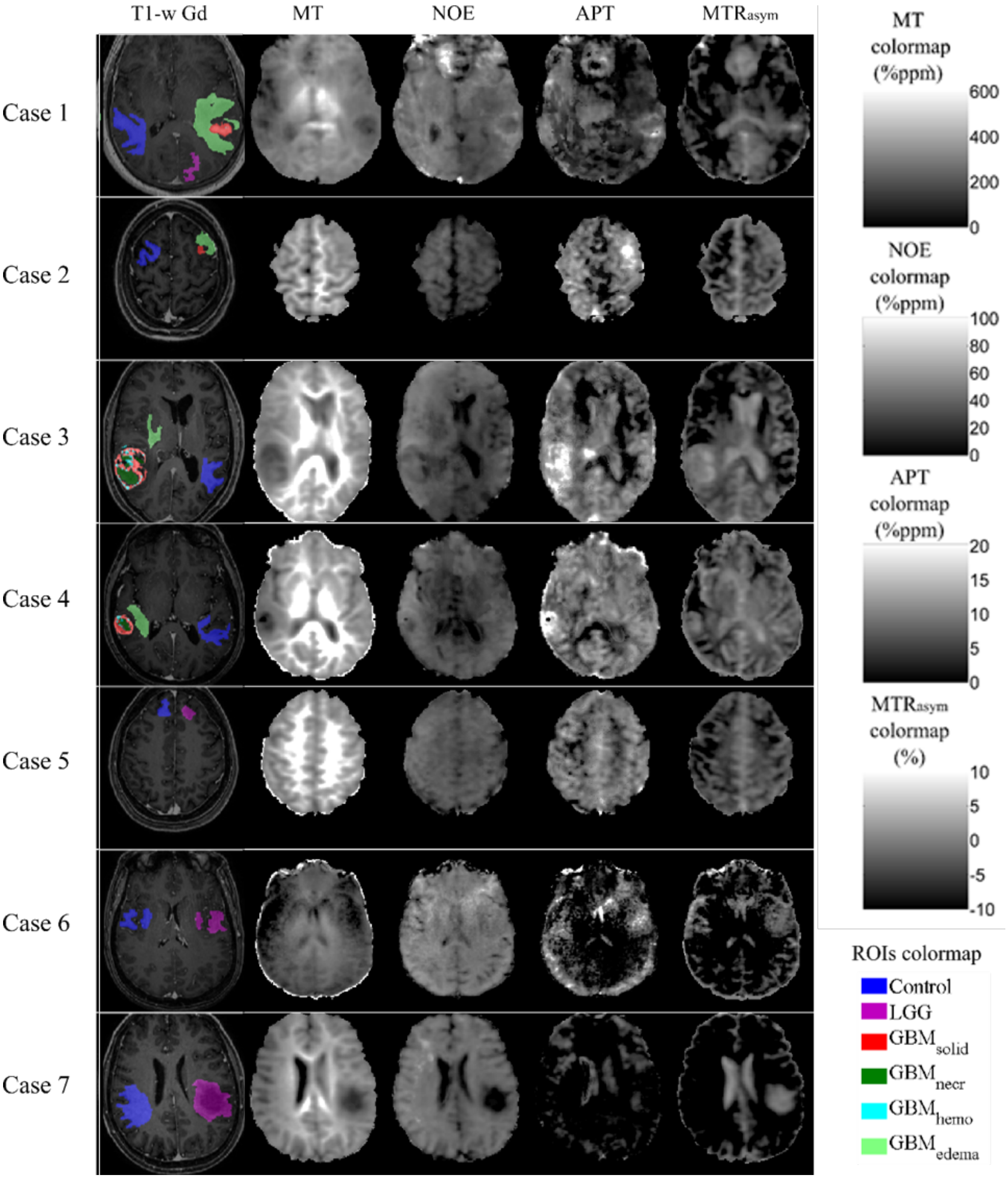

Figure 5.7: Co-registered structural MRI and 7T CEST in GBM (Cases 1-4) and LGG (Cases 5-7). First column: Gd-enhanced T_1w showing ROIs, second column: MT, third column: NOE, fourth column: APT map, and fifth column showing MTR_{asym} (grayscale coded as legend shows).

Lorentzian functions, as well as the asymmetry based APT metric. The MTR asymmetry maps showed high signal clearly exceeding background brain tissue in two cases, one GBM (case 3) and one LGG (case 7), and substantial background ventricular CSF signal was observed in all cases. Moderate gray matter/CSF interface signal was observed in 5/7 cases. In all compartments APT and the MTR_{asym} signal were moderately to strongly correlated (r = 0.43 in LGG, r = 0.49 in edema, r = 0.5 in controls, r = 0.58 in hemorrhage, r = 0.61 in total GBM, and r = 0.63 in solid and necrotic compartments).

5.4.4 Discussion

In this proof of concept study we obtained CEST MRI information with full tumour coverage at ultra-high field (7T), to assess whether the NOE and MT corrected APT signal has diagnostic utility in Glioma patients. We undertook a detailed quantitative analysis of APT/NOE and MT features in a small case series of low and high-grade Gliomas, and found APT increased up to 4 fold in total and solid GBM and MT decreased mainly in necrotic/hemorrhagic compartments, but with no significant NOE changes.

This study is different to early human studies of APT in tumours as it has attempted to overcome potential confounds of the APT signal by fitting a series of Lorentzians to the z-spectrum. Using high-resolution CEST imaging at 7T allowed us to calculate NOE and MT corrected APT maps with substantially increased spatial resolution and coverage. We showed up to 4 fold APT signal increases in glioblastomas that are independent of concurrent NOE and MT effects. We also showed that NOE and MT correction was important, at least at 7T, as asymmetry-based APT-related maps did not allow robust Glioma delineation or background suppression. This is an important contribution to the emerging field of APT imaging in Glioma as previous studies mainly used asymmetry analysis to quantify the APT effect. Asymmetry is measured by simply comparing the magnetization transfer ratio signals collected for saturation at +3.5ppm and -3.5ppm, however, since the APT and NOE effects are almost symmetric around the water peak, any analysis based on asymmetry will be sensitive to changes in either or both of these parameters, although such confounding effects may be field strength dependent as aliphatic NOE are less dominant at 3T[19].

Fitting for APT and NOE as separate effects on the *z-spectrum* allows the independent analysis of parameters in different compartments of the tumour, which may help to unravel the complex biological heterogeneity of Gliomas. There have been attempts to sensitize the asymmetry spectrum to APT but these results are either sensitive to inevitable variation in RF amplitude or assume a linear response to RF saturation in the CEST signal[35].

Limitations: This study was designed in 2013, before our work on the fully quantitative analysis of *z-spectra*, and we used an advanced CEST protocol at 7T but did not attempt to correct for T_1 or RF inhomogeneity (B_1) effects. Both these effects can have a large impact on the MT, APT and NOE signals, hence we attempted to mitigate these effects by choosing a saturation power at which the MT and NOE signal is not very sensitive to RF power[28]. Also, we reduced subject-by-subject variations in RF by comparing APT signals to a contralateral control region. Nonetheless, the effects of local variations in RF amplitude are not fully controlled for and will have contributed to the variance in the results. In the future this can be overcome by including B_1 and T_1 information in the data analysis[11]. Furthermore, recent studies are confirming our fully quantitative CEST results by showing that APT metrics should be corrected for water T_1 recovery, as well as potential downfield NOE effects[22,52]. Additionally, one of the data sets (case 1) was compromised by motion artefacts in the 1050Hz frequency dynamic (APT region), introducing some error in the estimation of APT.

5.5 APT in Glioma using a LUT

The results of the previous Glioma study have shown the potential of APT imaging in grading brain tumours, but were limited by the lack of B_1 and T_1 correction. The following (at the time of writing this thesis, ongoing) work shows the application of the fully quantitative method described in Chapter 4 to Glioma brain tumours. The method includes B_1 and T_1 information and is comparable to more recent B_1 and T_1 corrected Lorentzian-based approaches[51]. This study continues where the previous study ended, adding B_1 and T_1 correction to the methodology. My contribution was in the design of the MT sequence, scanning and analysis of all MT/CEST data.

5.5.1 Methods

Chapter 4 concludes by stating that the Look-Up Table (LUT) fitting approach is versatile in that it can be adjusted to study the parameter of interest, in this case APT. For this study, a new LUT was created that focuses more on APT by sampling the APT region of the spectrum more densely and focusing on a larger range of APT proton pool concentrations. One additional proton pool was also added to the LUT, that of Amine protons which are very near the Amide protons on the *z-spectrum*, in an effort to improve APT quantification further.

Creating a study-specific LUT: The LUT was simulated for two B_1 saturation powers, sampling the APT more in the low power while the high power sampled less frequencies, focusing mostly on MT fitting. The T_2 of the bound pool was also changed to 14μs, based on the results of the MT lineshape study in Chapter 3. Adding an amine proton pool, at low concentrations but high exchange rate, also meant that the APT parameters were changed. In the previous LUT both APT and Amine pools were described by a single effect at 3.5ppm with an exchange rate of 200Hz (in between Amine and APT exchange rates). All the parameters used in the simulation of this LUT are shown in Table 5.2.

Once the original database was numerically simulated, it was again linearly interpolated to 22 B_1 scaling values, 12 T_1 values, 17 MT, 16 NOE, 16 APT and 12 Amine values for a total of 13.8 million spectra at each nominal B_1 saturation level.

Table 5.2: Physical parameters used in the simulation of the LUT.

	Relative concentration (M_0 %)	T_1 **(s)**	T_2 **(ms)**	**Exchange rate with free water pool (Hz)**	**Chemical shift (ppm)**	**Low power saturation frequencies (ppm)**	**High power saturation frequencies (ppm)**	B_1 **amplitude**	B_1 **scaling**
Free water pool (DS)	-	Five values (1.2, 1.8, 2.5, 3 and 4 s)	40	-	0	-33.3 -16.7 -6.7 -5.7 -5 -4.7 -4.3 -4 -3.7 -3.5 -3.3 -3 -2.7 -2 -1 -0.3 0 0.3 1 1.7 2 2.3 2.7 3 3.2 3.3 3.5 3.7 3.8 4 4.2 4.3 4.7 5 5.7 6.7 16.7 33.3	-33.3 -16.7 -6.7 -5.7 -4.3 -3.5 -3 -2.7 -2 -1 0 1 2 2.7 3 3.3 3.5 3.7 4.3 5.7 6.7 16.7 33.3	Nominal B_1 amplitudes of 0.5 and 1.25μs $B_{1,rms}$	Saturation and imaging pulses scaled by 40, 70, 90, 110 and 150%
Bound pool (MT)	Six values (0.1, 1, 2.5, 5, 8 and 15 %)	1	0.014	20	-2.4				
NOE pool	Five values (0.1, 1, 3, 6, and 10 %)	1	0.4	20	-3.5				
APT pool	Eight values (0.01, 0.05, 0.1, 0.25, 0.5, 1, 2 and 3 %)	1	0.5	30	3.5				
Amine pool	Five values (0.01, 0.05, 0.1, 0.25 and 0.5 %)	1	20	1000	2.2				

Data acquisition: The data acquisition was done in the same way as before, but at the different off-resonance frequencies and saturation powers shown in Table 5.2. B_1 and B_0 maps were acquired too, as well as a high resolution PSIR that was also used to create a T_1 map. As before, the MT imaging readout acquired 410 gradient echoes, TE/TR = 2.8/6ms, FOV = 192 x 186 x 50mm, 1.5mm isotropic voxel size, low-high spiral k-space acquisition. The 3D volume acquisition required 4 repetitions of this cycle, giving an acquisition time of 20s per frequency offset and a total acquisition time of 13 minutes for the low power spectra, and 8 minutes for the high power spectra. Multiple 50kHz datapoints (one every 10 frequencies) were also acquired for signal drift correction.

5.5.2 Results

Figure 5.8 shows a fit of spectra from a NAWM ROI to the Glioma LUT. Note how the low power spectrum is more densely sampled around the NOE and APT regions. The two spectra are fitted as a couple, with the B_1 scaling factor dictated by the acquired B_1 map. If there was uncertainty in the power deposition, for instance when the power optimization step of the scan failed and different drive scales were given to the two separate MT scans, then the coupled acquired spectra will not match the coupled simulated spectra. For this reason, the RF drive scales of each scan were recorded and the spectra were matched to the corresponding B_1 values in the LUT.

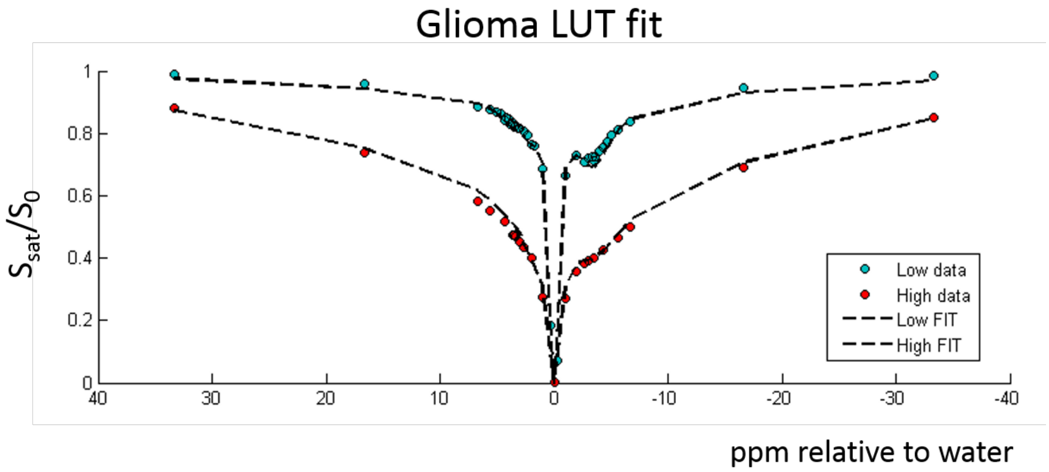

Figure 5.8: An example of the Glioma LUT fit in NAWM.

Figure 5.9 shows the results obtained when using the LUT fitting method in two histologically graded high grade GBM cases. Maps of MT, NOE and APT are shown for both cases, together with T_1 maps extracted from the PSIR data.

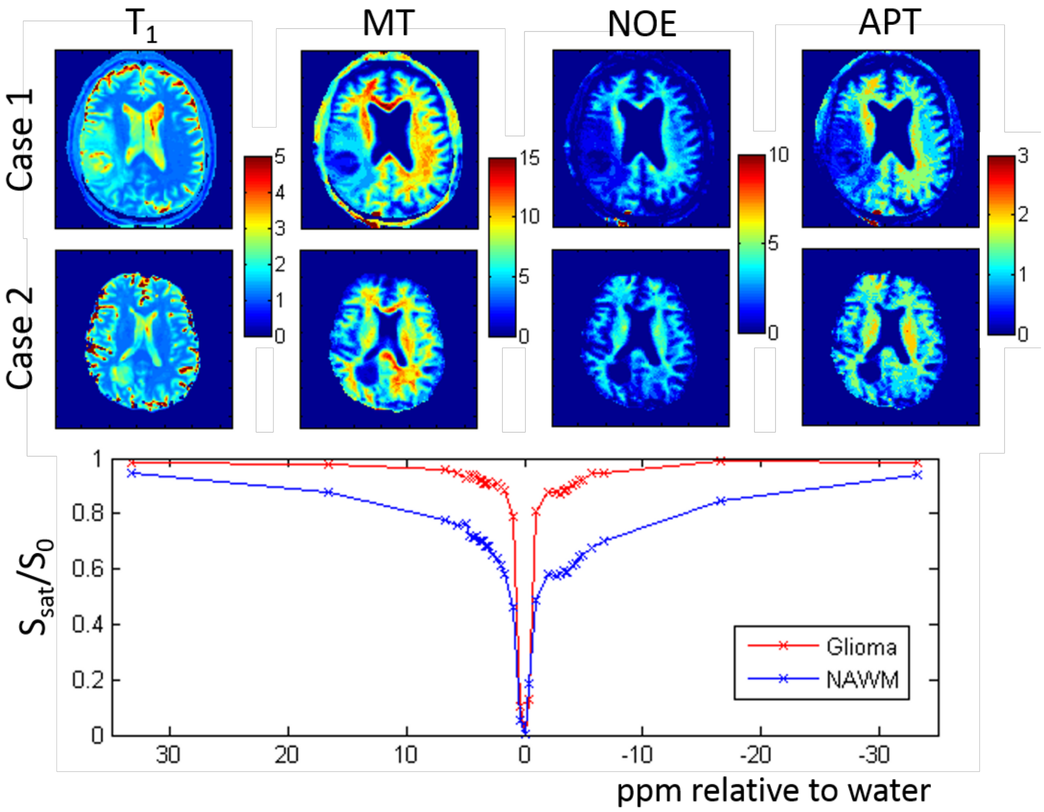

Figure 5.9: Co-registered structural MRI (PSIR/T_1) and 7T CEST in two Glioma cases. First column: T_1 maps in seconds, second column: MT, third column: NOE, fourth column: APT map. The MT, NOE and APT maps are scaled in % proton pool concentration. Spectra are shown for a voxel inside the tumor in case 2, together with spectra from a contralateral NAWM region.

Figure 5.10 shows a comparison between APT maps from the same data as in Figure 5.9, but processed to show APT from B_1 corrected Lorentzian fitting (APT_{LOR}), APT metric using the B_1 and T_1 corrected Lorentzian fitting method (APT_{AREX}) and the APT results from the LUT fit. Note the ring of hyper-intense APT signal (red arrow) disappearing when T_1 correction is implemented.

5.5.3 Discussion

At this stage in the study, there are no available ROIs for the core of the tumour, the enhancing area or edema, so a statistical analysis was not attempted. The main finding of this work so far is the change in APT signal when it is

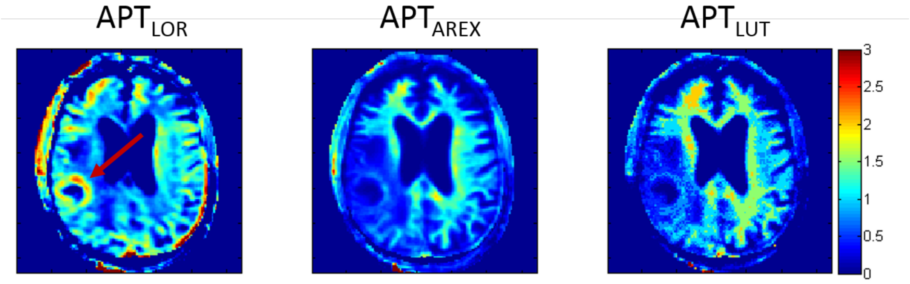

Figure 5.10: Three different APT metrics. From left to right, APT as the B_1 corrected AUC of a fitted Lorentzian function (APT_{LOR}), B_1 and T_1 corrected APT from Lorentzian fitting (APT_{AREX}) and the LUT APT results (APT_{LUT}). The LUT APT results are scaled in proton pool concentration %, whereas the Lorentzian-based APT metrics are in arbitrary AUC values. From case 1.

correctly separated from MT, NOE and T_1 effects. Even before T_1 correction, both the LUT method (we can fix the search to one specific T_1 value) and REX (AREX without T_1 correction) reduce the APT signal significantly, showing that the new APT contrast is not only a result of T_1 variation. When corrected for T_1 and B_1, the hyper-intense APT signal returns to normal levels, even lower level than contralateral NAWM regions. Nevertheless, APT imaging still provides a unique contrast mechanism that should be exploited further. Case 1 presented here shows a GBM with edema in the surrounding tissue. The edema can be seen in the quantitative MT, NOE and APT maps too as reduced signal. Case 2 shows a GBM with minimal edema but a T_2^* image showed haemorrhage within the tumour, which disrupts the CEST signal. This shows that haemorrhagic regions continue to present a challenge in MT and CEST quantification. Another interesting finding is the consistently high APT signal in the Sagittal Sinus both before and after T_1 correction. This indicates that a high APT signal in enhancing regions of Gliomas could be related to high activity and blood perfusion, and is now being investigated further with CEST experiments in blood.

Figure 5.9 shows the two cases scanned so far, and they are both high grade Gliomas, but show slightly different MT, NOE and APT signal, highlighting the heterogeneity of Gliomas. In the first case, a large region around the tumour shows lower MT, NOE and APT regions, and can also be seen on the T_1 map as hyper-intense, suggesting edema. The second case shows no region of edema, and also shows no contrast at all within the tumour. Investigating the case 2 tumour ROI further has shown very low levels of *z-spectrum* signal (see spectra in Figure 5.9), as well as a narrower water peak (longer water T_2). We attempted fitting the tumour spectra with a new, longer water T_2 database, but even then the proton pool concentrations were close to zero. Signal drift correction was also attempted but did not significantly change the results.

5.5.4 Conclusions

APT imaging of brain tumours has evolved considerably since the very first asymmetry-based work and our original Lorentzian fitting study, into metrics that can quantitatively and reliably measure APT signal that is undiluted by other effects. The work presented in this chapter shows results from two different APT quantification methods that give somewhat different results. The first method lacked B_1 and T_1 correction but was able to provide an APT threshold that distinguishes between LGG and GBM, albeit with very few subjects. The second method was successful in correcting for B_1 and T_1 but is still only in the early stages of the study, with only two subjects available and no information on tissue necrosis, enhancing regions or edema. With more subjects and clear ROIs, the quick LUT-based approach has the potential to help expand our understanding of the individual compartments or proton pools within Gliomas and aid in non-invasive, *in-vivo* tumour grading.

5.6 Relationships between cortical myeloarchitecture and electrophysiological networks

5.6.1 Introduction

The human brain relies upon the dynamic formation and dissolution of a hierarchy of functional networks to support ongoing cognition. However, how functional connectivities underlying such networks are supported by cortical microstructure remains poorly understood. In this work we test a hypothesis that gray matter myelin is related to functional connectivity. Functional connectivity refers to statistical interdependencies between patterns of brain "activity" measured at separate cortical locations[3] and, even in the "resting state", measured spontaneous brain activity defines nonrandom networks that are related to cognitive processes[2]. While the connection between these functional networks and the supporting white matter pathways is reasonably well understood[29], it is likely that the structure–function association extends to gray matter morphology, for which fundamental understanding is lacking.

To study gray matter morphology, we created structural covariance[1,16] matrices, based upon cortical myeloarchitecture, which show how structural properties of individual brain regions covary over subjects. For example, individuals with a high cortical volume in Broca's area typically exhibit high cortical volume in Wernicke's area, reflecting a language network[25]. Similar observations can be made between other associated cortical regions[48]. These structural covariance matrices are then compared to functional connectivity matrices mapped with Magnetoencephalography (MEG).

The rich temporal complexity of MEG signals means that multiple ways to characterize functional connectivity exist[37]. However, one of the most robust methods is amplitude envelope correlation (AEC)[33], which probes temporal relationships between the envelope of oscillations, in a frequency band of interest, at spatially separate brain regions. Given that these measurements represent the principal long-range functional connections in the brain, and given the evidence that electrical activity mediates myelination, we hypothesized that networks of oscillatory envelope correlation, measured between parcellated regions and in multiple frequency bands, would allow prediction of a network of structural covariance representing myeloarchitecture. This study was led by Ben Hunt as part of his PhD and is now a published paper[18]. My contribution includes input in the study design, scanning and (together with Ben Hunt) creating a robust processing pipeline for the MT data.

5.6.2 Methods

Fifty-eight volunteers (39±12 years old, 27 male) took part in the study. Using ultra-high field MRI (7T), and the method described in Chapter 4, we measured magnetization transfer (MT) across the brain. These measurements were parcellated into 64 cortical regions according to the Automated Anatomical Labeling (AAL) atlas and normalized by region volume to give myelin density estimates. Following this, assessment of structural covariance between all possible AAL region pairs allowed derivation of a network matrix showing the degree to which separate (AAL) regions exhibit similarities in their myeloarchitecture. The same individuals also underwent resting-state MEG acquisition. MEG data were parcellated according to the same atlas, and Resting State Networks (RSNs) characterizing functional connectivity, between all possible AAL region pairs, were derived using AEC in five frequency bands. With the aid of a recently developed framework[42], we then characterized the relationship between the structural network, representing myelin density, and functional networks, representing the major pathways of electrophysiological communication.

MT and structural covariance: For MT, the same exact protocol described in Chapter 4 was used, comparing *z-spectra* from three coupled B_1 saturation powers to a LUT containing B_1, T_1 and proton pool concentration information. Separate B_1 and T_1 maps were acquired that restricted the fit to specific values in the LUT, giving B_1 and T_1 corrected proton pool concentration values. The LUT was simulated for three pools (other than water): MT, NOE and APT, but for this study only MT was used. Gray matter masks were computed from a T_1 weighted PSIR image using SPM8, at a high probability value of 0.8. To investigate structural covariation of myelin within the AAL regions, gray-matter-masked MT data were registered to the AAL atlas and a mean MT value was calculated for each region, for each participant. Due to confounding factors such as scanner drift, the modal value for each individual's MT data was regressed from that individual's regional values.

Resting-State MEG connectivity analysis: Three hundred seconds of eyes-open resting-state MEG data were acquired using a 275-channel CTF MEG system operating in third-order synthetic gradiometer configuration (sampling frequency of 1,200 Hz). Three head position indicator coils were placed at fiducial locations on the subject's head and energized to facilitate continuous tracking of head location. Before acquisition, a 3D head digitization procedure was completed. Co-registration between MEG system geometry and individual brain anatomy was achieved by matching the digitized head surface to the equivalent surface extracted from an anatomical MRI. Functional connectivity was calculated between AAL regions. A scalar beamformer was used to obtain a single MEG signal representative of each region. The magnitude of the analytic signal, computed via a Hilbert transform, was used to generate the amplitude envelope of oscillations, for each regional time course in all frequency bands. Pearson correlation was then computed between envelopes for each region pair. In this way we generated a single adjacency matrix for each subject, and frequency band, representing whole-brain connectivity. These matrices were averaged over subjects.

Handedness was also measured using the Edinburgh Handedness Inventory.

5.6.3 Results

Figure 5.11A shows MT proton pool concentration in %, averaged across subjects and plotted for all the AAL regions. The gray areas on the brain maps show regions where scan coverage was insufficient to give accurate MT estimates. High myelination was observed in primary sensory cortices, with statistical tests showing that this spatial variation was significant; for example, significantly (P < 0.001) higher myelination was found in primary motor cortex compared with the dorsolateral prefrontal cortex. A hemispheric division was also noted with significantly (P < 0.01) higher MT in left compared with right sensorimotor cortex. Figure 5.11B maps the variation of correlation between MT and handedness across the cortex.

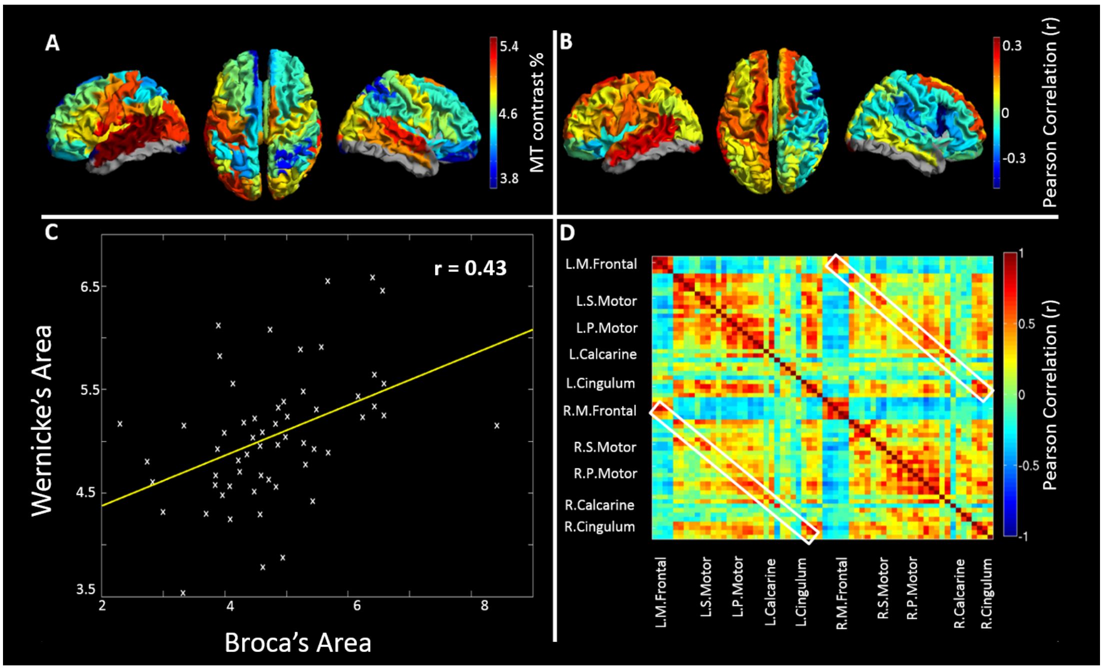

Figure 5.11: In vivo myelination measures and the structural network. (A) Mean MT contrast percentage for all AAL regions. High MT is reflective of high myelination. Note high levels of myelination in primary cortical regions. (B) Correlation between MT and handedness. Positive correlations show regions where myelin is higher in right handers. Negative correlations show regions where myelin is higher in left handers. (C) Example plot showing correlation over subjects between MT measured in the AAL regions capturing Broca's and Wernicke's areas. These correlations are the basis of the structural network. (D) The myelin structural network, represented as a matrix. Each element denotes cross-subject correlation in MT between two brain regions.

A positive correlation denotes regions where right handers have more myelin than left handers; a negative correlation denotes regions where left handers have more myelin than right-handed individuals. Note a significant ($P < 0.05$) split in the polarity of the correlation between hemispheres.

The principle of structural covariance and the structural network are shown in Figure 5.11 C and D, respectively. Figure 5.11C shows correlation between MT in Broca's area (averaged across all subjects) and Wernicke's area, with a significant positive correlation ($P < 0.001$). Figure 5.11C shows the correlation from one pixel on the matrix in Figure 5.11D. Note that structural covariance between adjacent AAL regions is generally denoted by matrix elements close to the leading diagonal, whereas structural covariance between distal regions is represented far from the diagonal. The white boxes show structural covariance between homologous regions.

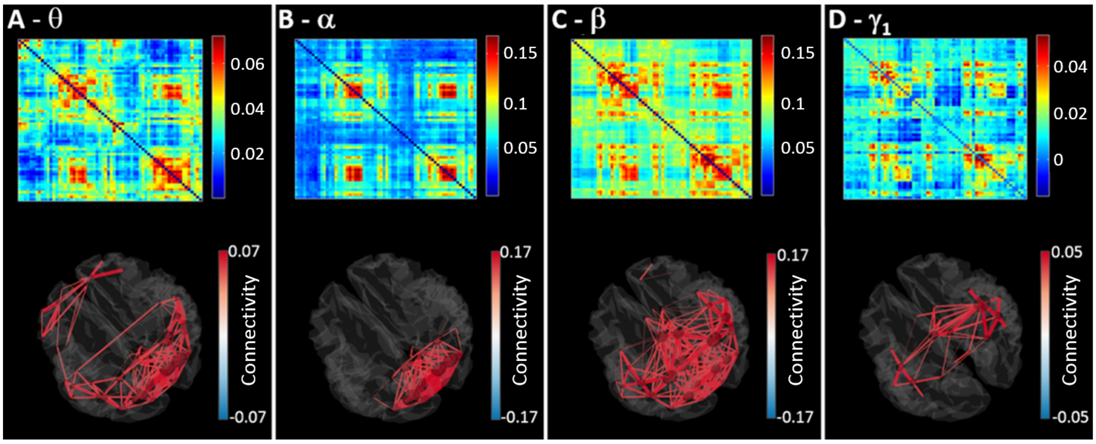

Figure 5.12: MEG functional connectivity matrices. Matrices represent AEC in the (A) theta (4–8 Hz), (B) alpha (8–13 Hz), (C) beta (13–30 Hz), (D) low–gamma (30–70 Hz), and (E) high-gamma (70–120 Hz) bands. All matrices show Pearson correlation between AAL region pairs. The 3D plots shown depict all connections within 5% of the maximum value in each band.

Figure 5.12 shows the MEG functional connectivity matrices for four frequency bands. All networks are represented by a matrix similar to that in Figure 5.11D. The 3D brains display all connections within 5% of the maximum value, showing that network structure differs between frequency bands.

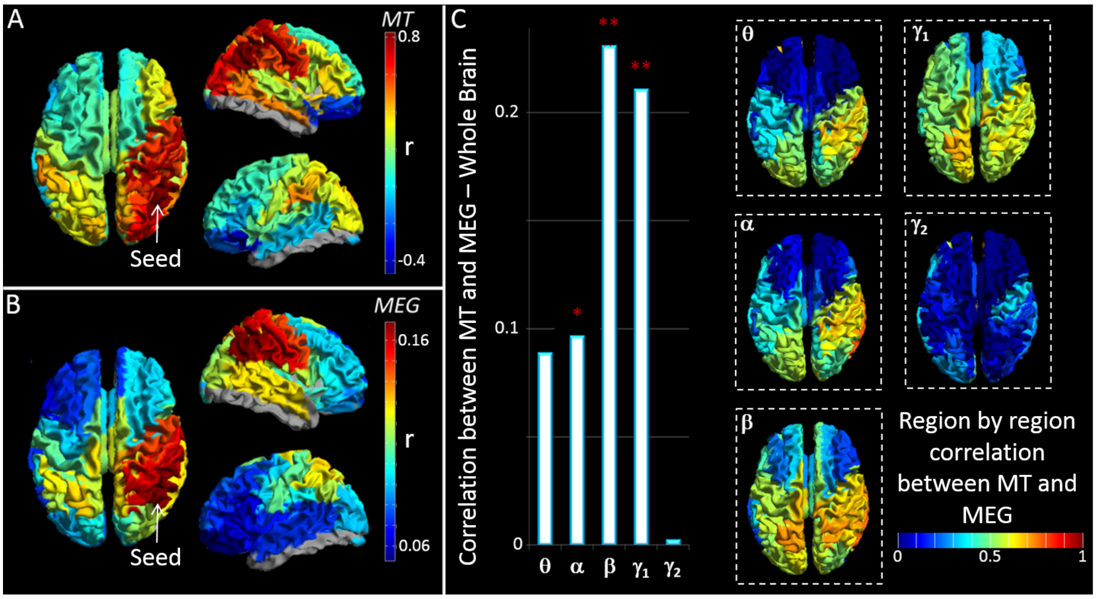

Figure 5.13: The relationship between MEG networks and myelination. (A) Structural covariance between a seed region in right inferior parietal cortex and all other brain regions. (B) Seed-based functional connectivity, calculated using MEG in the beta band between the same seed region in inferior parietal cortex and all other regions. Note the similarity between A and B. (C) The bar chart shows correlation between the structural network (Fig. 5.11D) and the functional networks (Fig. 5.12). Correlation is measured over the whole matrix (i.e., for all possible seed regions) and is shown for all frequency bands. ** indicates a significant relationship; * indicates a trend. The inset images show which seed regions drive the relationship in the bar chart [i.e., red indicates a region whose structural connectivity (MT) profile and functional connectivity profile are highly correlated].

Figure 5.13A shows a "seed-based" structural covariance map (i.e., a single column of the matrix in Figure 5.11D). When a seed region is placed in the right inferior parietal cortex, the surrounding regions show high structural covariance to the seed, and a cross-hemispheric pattern of high structural covariance between homologous regions is also observed. Figure 5.13B shows the equivalent seed-based map calculated using beta band MEG data. A strong similarity between the structural and functional networks can be seen. Figure 5.13C shows the correlation between the full MT structural covariance matrix and the group-averaged functional connectivity matrices for all frequency bands (Figure 5.12).

The resulting r^2 values show that functional networks measured in the beta and low-gamma bands predict significantly the spatial pattern of structural covariance. Neither theta nor high-gamma bands showed a measurable relationship, and the alpha band showed a trend. The inset images show seed regions for which structural covariance is best predicted by functional networks.

5.6.4 Discussion

Although recent years have seen significant progress in mapping the human connectome, the relationship between functional networks and cortical microstructure remains poorly understood. A recent study[12] in animals suggests that electrical activity promotes myelination. We therefore reasoned that, if functional networks represent major pathways of electrophysiological communication, then those pathways should shape myeloarchitecture and a significant relationship between functional connectivity and myelin should be observable. Our results support this, with significant correlation between the structural network and functional networks mediated by neural oscillations in the beta and low-gamma bands.

This strong correlation between structural covariance and functional connectivity was only possible because of the effectiveness and precision of both MT and MEG methods. The new quantitative MT method was able to provide measurements that are unaffected by variation in B_1, water T_1 and cortical thickness, and created matrices of structural covariance that very closely resemble functional connectivity (Figure 5.13).

In this work we used MT as an estimation of myelin content. Although serving as an efficient marker of myelination, it is important to note that there is no one-to-one relation between MT and myelin density, and the relationship may break down further in pathology. Nevertheless, our results are in agreement with others, showing that the highest myelin concentration occurs in sensorimotor, auditory, and visual cortices. This finding supports an argument that myelin acts as a means to increase the speed of processing and inhibit plasticity in these primary sensory areas.

A potential limitation of our methods is that MT was parcellated according to the AAL atlas. This was done to allow derivations of network graphs that can be compared with MEG, but the regional parcellation of the AAL atlas does not take into account known differences in myelin signature throughout the cortex. In future studies, parcellation based on myeloarchitecture would be of high value[13].

5.6.5 Conclusions

In this work we have used the quantitative MT methodology to probe the relationship between gray matter myelination and electrophysiological networks, showing a significant correlation. This further highlights the effectiveness of the MT method, even in gray matter where myelin content is low and MT quantification is inherently more difficult. The relationship found is strongest for networks mediated by beta oscillations but becomes stronger when integrating across frequency bands, suggesting that myeloarchitecture supports connectivity across all bands. Our study sheds light on the way in which cortical microstructure supports functional networks, the latter being mediated by neural oscillations. Further, it paves the way for future investigations of the structure/function relationship and its breakdown in pathology.

5.7 MT vs. NOE in the human brain

5.7.1 Introduction

The origin of the Nuclear Overhauser Enhancement (NOE) signal observed in the *z-spectrum* of the brain is still under debate. The effect is detected upfield from water, in the frequency range of non-exchangeable aliphatic/olefinic protons[21], indicating that the transfer of magnetization is not occurring via proton or chemical exchange; furthermore the lineshape is relatively narrow, suggesting the signal is coming from mobile protons with T_2 of the order of 300μs. These observations indicate that the transfer of magnetization in NOE occurs primarily via dipolar interactions, possibly relayed by a secondary chemical exchange mechanism[21].

Nonetheless, the origin and clinical relevance of this parameter in the brain remains unknown. The aim of this work was to investigate the relationship between MT and NOE (NOE as a single proton pool at -3.5ppm) in the human brain, using the same data that was acquired for the previous sections of this chapter (Sections 5.3 and 5.6). The relationship between MT, NOE and T_1 was also investigated. This section presents an analysis study on data that was acquired in the previous studies mentioned above. The analysis was performed by myself, Olivier Mougin and Penny Gowland.

5.7.2 Methods

Acquisition: This study used the same data acquired in the previous section of this chapter (53 healthy volunteers). *Z-spectra* were acquired at 3 different B_1 saturation powers (B_{1rms} = 0.38μT, 0.75μT, and 1.25μT) together with B_0 and B_1 maps, and PSIR used to produce a T_1 map. All scan parameter details can be found in[11] and Chapter 4. The four multiple sclerosis patients described in Section 5.3 were also included. In the MS study, *z-spectra* were acquired in a similar manner except at only 2 B_1 saturation powers (0.38μT, 0.75μT).

Fitting: For each subject, B_0 corrected *z-spectra* were fitted voxel-wise for the amplitude of 3 pools (MT, NOE at -3.5ppm and APT) to a LUT of Bloch-simulated spectra, correcting for B_1 and T_1 to produce quantitative MT and NOE maps (Figure 5.14).

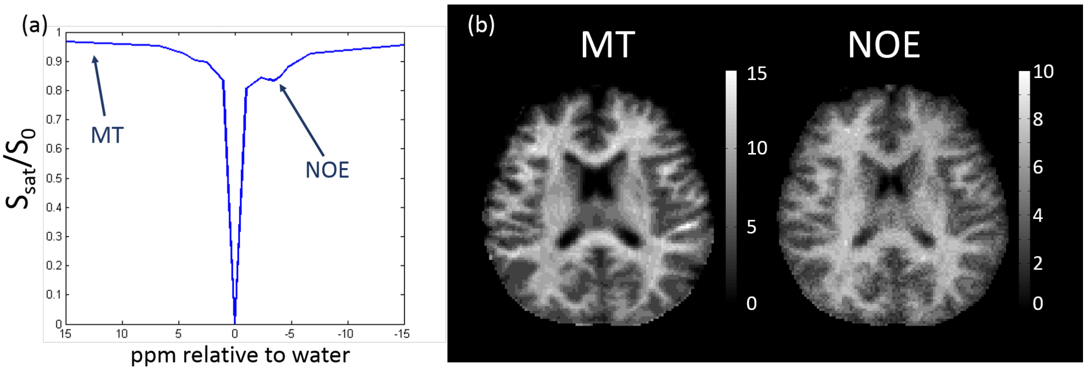

Figure 5.14: (a) Acquired *z-spectrum* showing the NOE peak and MT baseline. (b) Quantitative MT (left) and NOE (right) maps. The scales are in % proton pool concentration. Data from one healthy volunteer (from Section 5.6).

Segmentation: All PSIR images were segmented using the FreeSurfer image analysis suite, which is documented and freely available for download online (http://surfer.nmr.mgh.harvard.edu/), and brain tissue classified using the Desikan-Killiany atlas[8] (35 White Matter (WM) regions, 35 Gray Matter (GM) regions). For the MS patients, lesion masks were created to separate normal appearing GM (NAGM) from normal appearing WM (NAWM) and lesions. Lesion masks were drawn manually whereas WM and GM masks were segmented from a PSIR image using SPM8.

Correlation: NOE signal was correlated (Pearson correlation) against MT for the individual regions (averaged over subjects), and for individual subjects (averaging the regions into whole-head WM and GM). The subjects were also split into three age groups to investigate any age effect. Similar region averaged plots were also made for the MS data. In the correlations presented here, regression of B_1 was also attempted with no significant change to the results, showing that the B_1 correction implemented is effective.

5.7.3 Results

Figure 5.15 correlates NOE and MT averaged over all WM and GM separately for all 53 healthy controls. Each data point on the plot represents the averaged

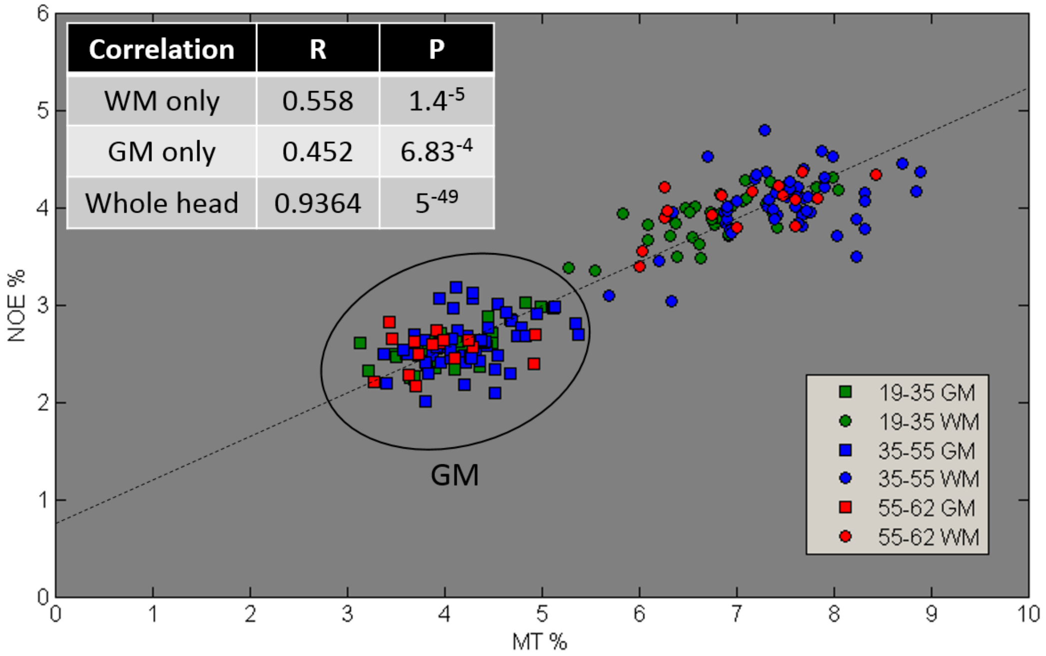

Correlation	R	P
WM only	0.558	1.4^{-5}
GM only	0.452	6.83^{-4}
Whole head	0.9364	5^{-49}

Figure 5.15: NOE vs. MT for each of the 53 healthy controls. The subjects are separated into three different age groups shown in the legend. A least squares line is also shown shown. Each data point on the plot represents the averaged signal from all 35 segmented regions for WM and GM.

signal from all 35 segmented regions for each subject. The graph plots the averaged NOE vs. MT for both WM and GM, showing a total of (53 x 2 = 106) datapoints, separated as circles for WM and squares for GM. A strong correlation between NOE and MT values across subjects can be seen ($R = 0.9364$, $P = 5^{-49}$) when correlating across both WM and GM. A strong positive correlation is also evident when only considering WM or GM values. Three different age groups were separated (different colours in Figure 5.15), but no significant change in correlation is seen with age.

We also investigated the effects of age on MT, to explain the greater variation in MT than NOE in Figure 5.15. The results (shown in Figure 5.16) show that MT is highest in middle age and decreases with old age, both in WM and GM. Figure 5.17 shows a strong correlation between NOE and MT for the subject-averaged values within the 70 segmented regions. Each data point on the graph represents the average signal from all subjects for a specific region, and are separated into WM (blue) and GM (red). NOE vs. MT signal from the Sagittal Sinus (SS) is

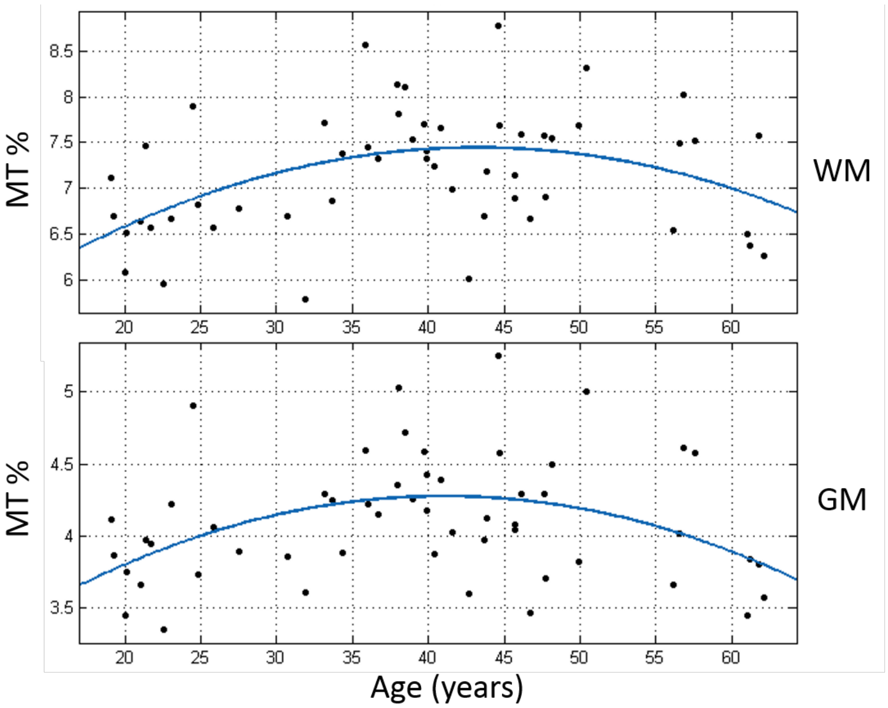

Figure 5.16: MT vs. Age in WM (top) and GM (bottom). Each dot represents one of 53 healthy controls and the blue lines show a second degree polynomial fit to the data.

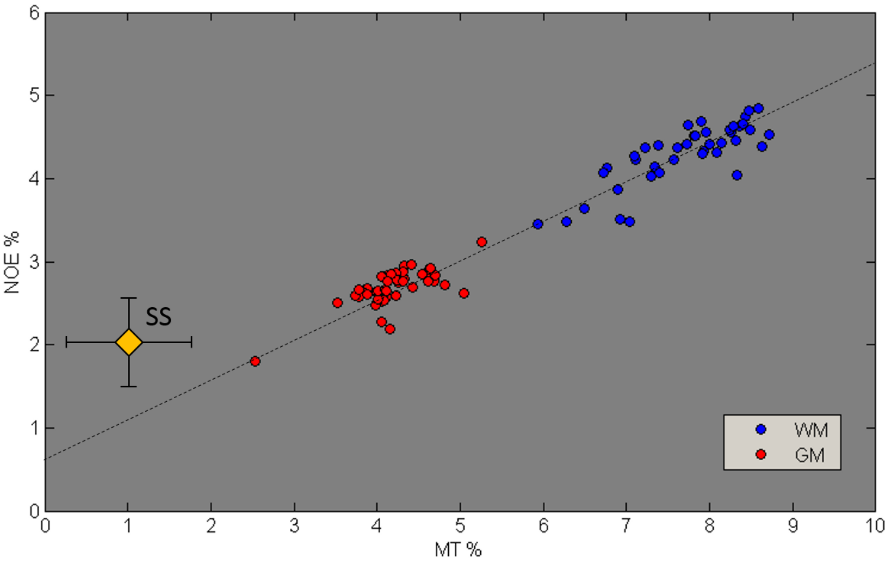

Figure 5.17: NOE vs. MT for each of the 70 regions. Each circle shows the NOE vs. MT for a specific region, averaged across all subjects. The mean and standard deviation signal from the Sagittal Sinus (SS) of 5 subjects is also shown in yellow. The offset and large standard deviation of the SS data are likely to be caused by blood flow and the low number of subjects used in the average, respectively.

also shown in the figure.

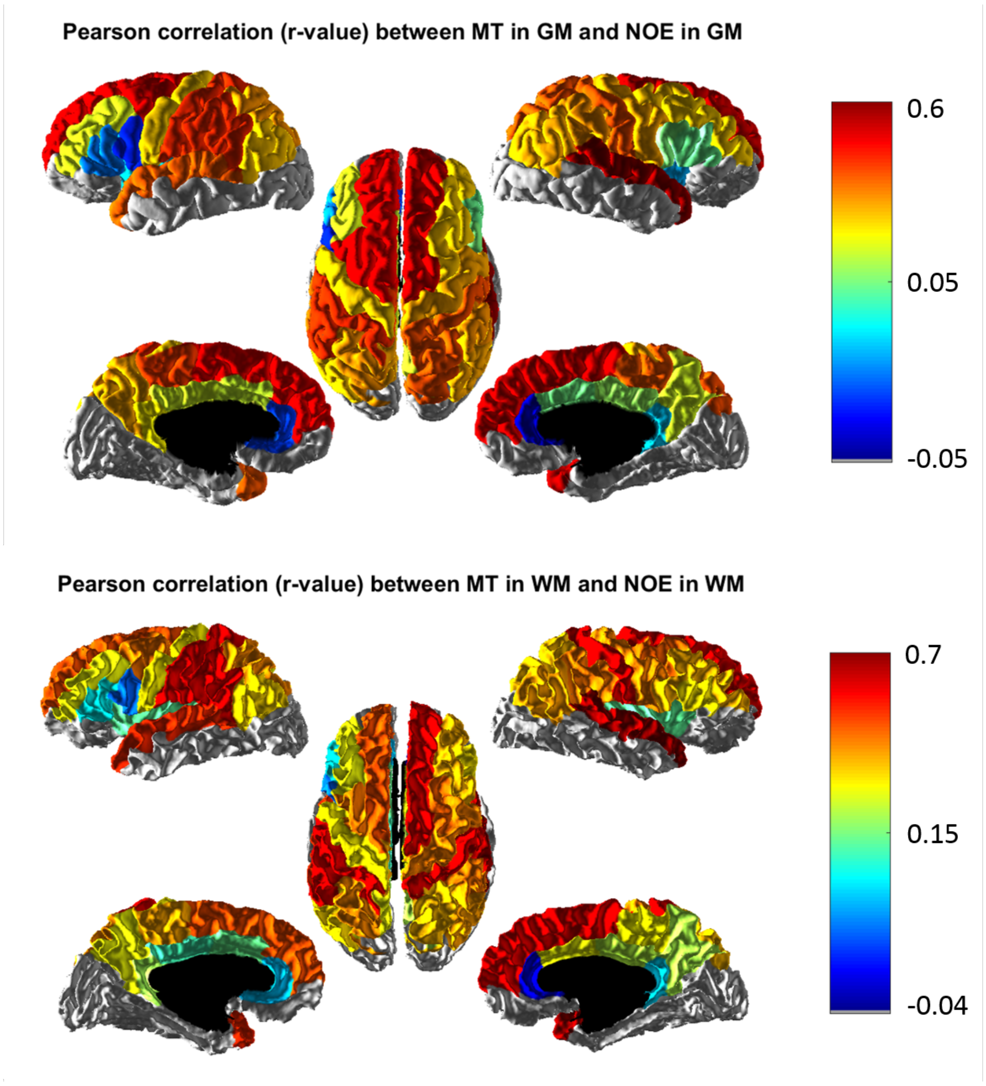

Figure 5.18: Pearson correlation R-values for MT vs NOE in each of the regions, in WM (top) and GM (bottom). These regions correspond to the regions shown in Figure 5.17. The gray areas represent regions for which there were no MT or NOE data (not covered in the scanned FOV), and the black areas are regions that are not included in the Desikan-Killiany atlas.

Figure 5.18 shows the correlation between MT and NOE in each of the 70 regions, plotted on separate WM and GM surface maps. Note the similarity of the WM and GM surface maps. The WM regions in the Desikan-Killiany atlas are sub-cortical regions that do not extend fully towards the ventricles and Corpus Callosum (hence the Corpus Callosum is not shown on the surface maps).

Figure 5.19 shows the same maps as Figure 5.18 but plotting the P value instead of the R value. This shows the correlation is significant in most regions.

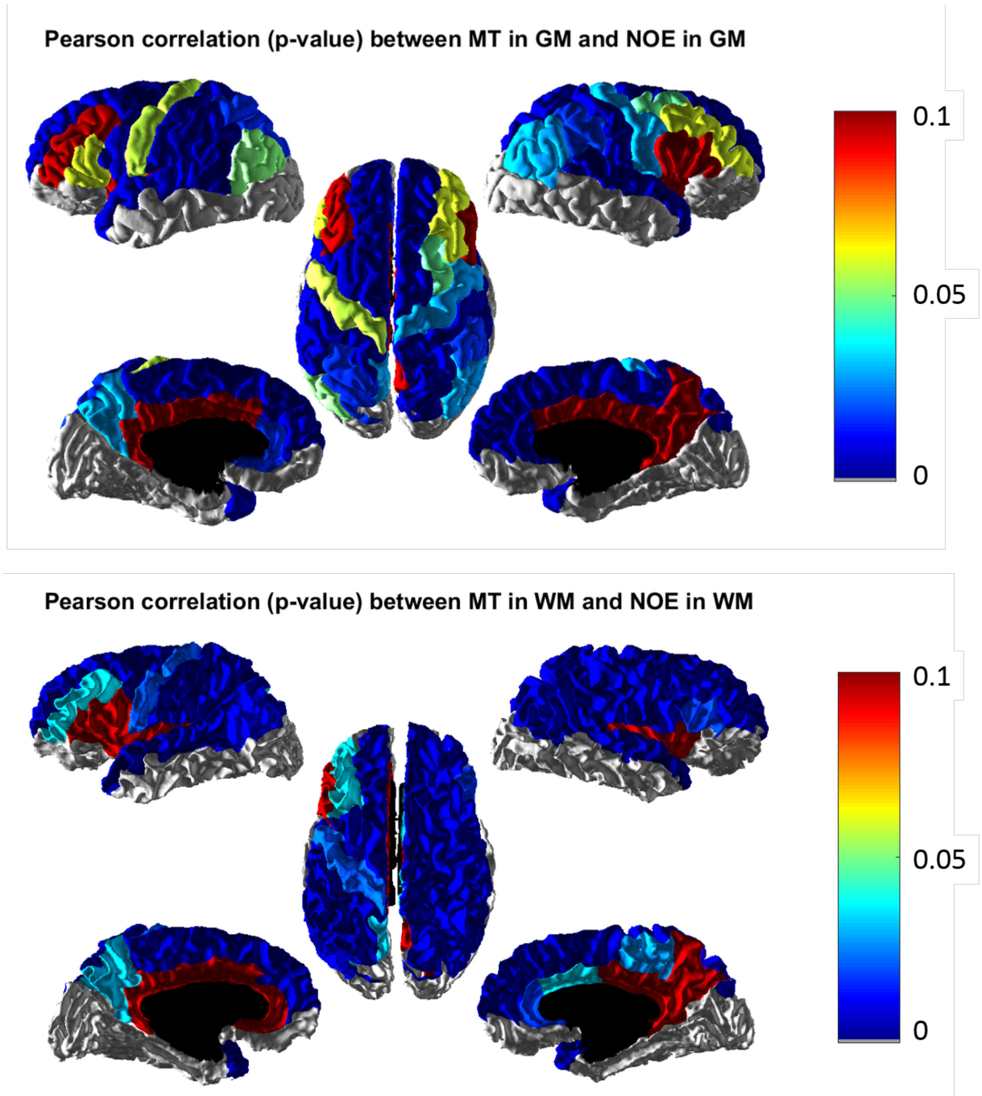

Figure 5.19: Pearson correlation P-values for MT vs NOE in each of the regions, in WM (top) and GM (bottom).

Figure 5.20 shows correlations between MT and T_1, and NOE and T_1. While the quantification method corrects for the effects of T_1 on measuring MT and NOE, longer T_1 indicates less myelination and therefore both MT and NOE values are expected to be lower for long T_1. This is evident in Figure 5.20 where a weak negative correlation is seen in both MT and NOE vs. T_1, which is more significant in NOE and in particular the right hemisphere.

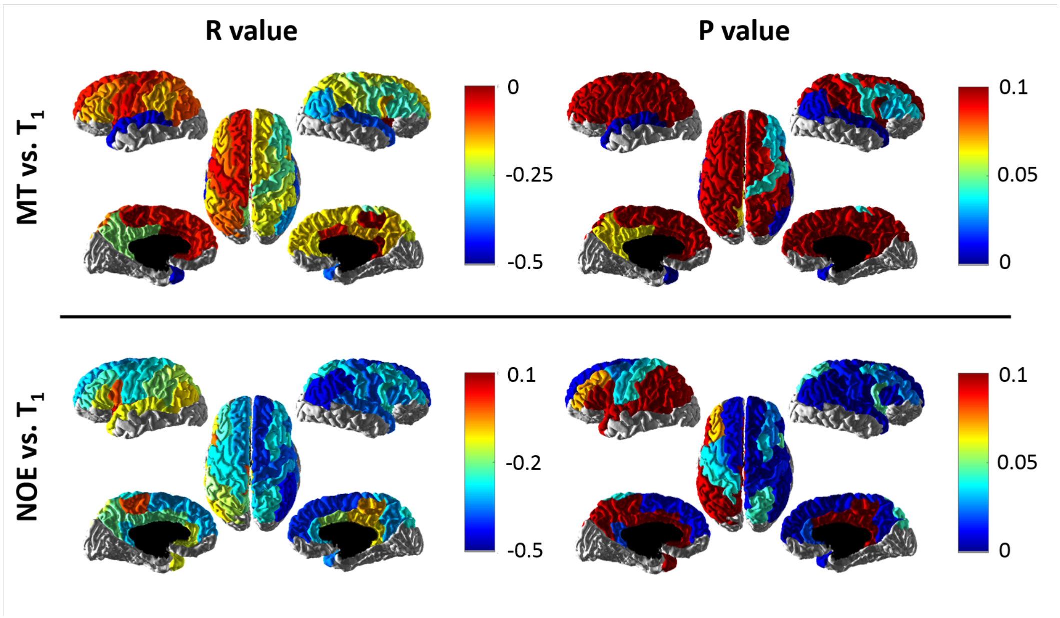

Figure 5.20: Pearson correlation R and P values for MT and NOE vs T_1 in each of the regions. Surface maps are only shown for GM. WM results show a very similar trend.

Figure 5.21 shows the relationship between MT and NOE in MS. Each of the green datapoints in the plot shows the averaged MT vs. NOE of all lesions present in each scan. There are 24 scans in total (4 patients, 6 visits each). Note how the MT vs. NOE relationship remains the same in MS.

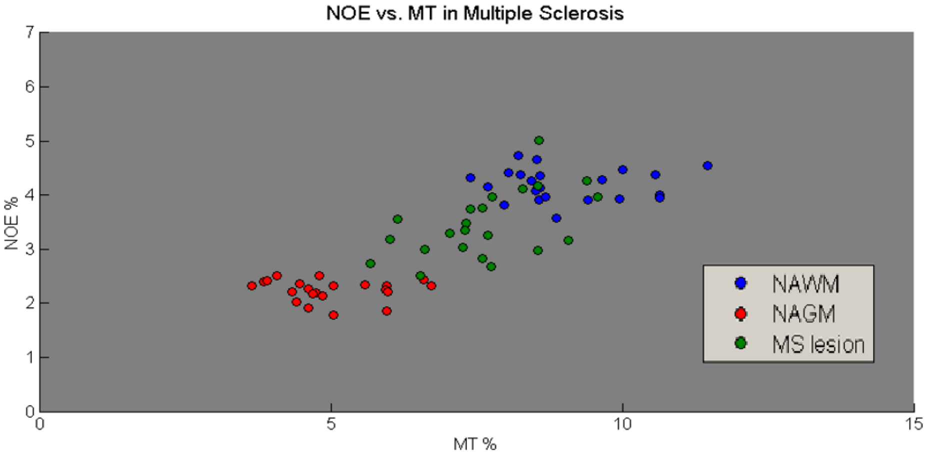

Figure 5.21: NOE vs. MT in multiple sclerosis. The blue circles show averaged whole-head NAWM in 24 separate scans (4 patients, 6 visits each), the red circles show NAGM and the green circles show averaged NOE vs MT from all lesions in each scan.

To further investigate the relationship between MT and NOE in the WM, we also plotted the slope (or gradient) of the correlation on the same surface maps shown in Figure 5.18. The slope is shown for all the healthy controls together, as well as for the three separate age groups (younger than 35, between 35 and 55, over 55). The results are shown in Figure 5.22. The plots of MT vs. NOE for each of the 35 regions are also shown in Figure 5.23.

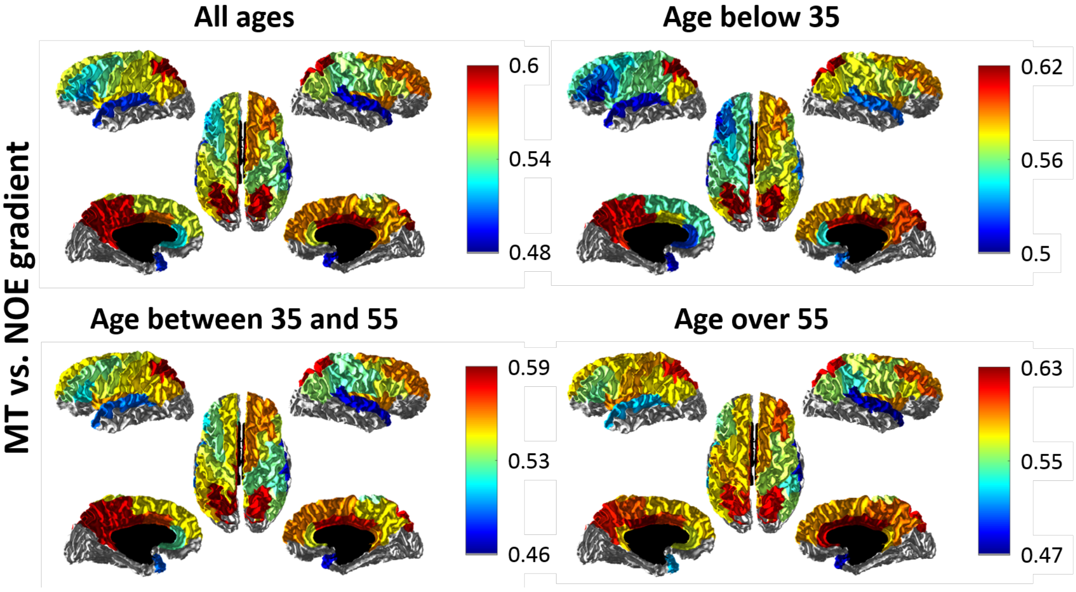

Figure 5.22: MT vs. NOE slope in all subjects (top left), subjects under 35 years old (top right), subjects between 35 and 55 (bottom left) and subjects over 55 (bottom right).

The Desikan-Killiany atlas regions are shown in Table 5.3.

5.7.4 Discussion

We have shown that for the normal brain the *z-spectrum* NOE signal is tightly coupled to the MT signal across GM and WM regions, and across subjects irrespective of age. Although the MS and healthy control data cannot be directly compared due to the difference in acquisition parameters, a similar tight coupling is found in MS, even within lesions. A relationship between MT and age has also been shown, which explains the higher variation in MT than NOE when

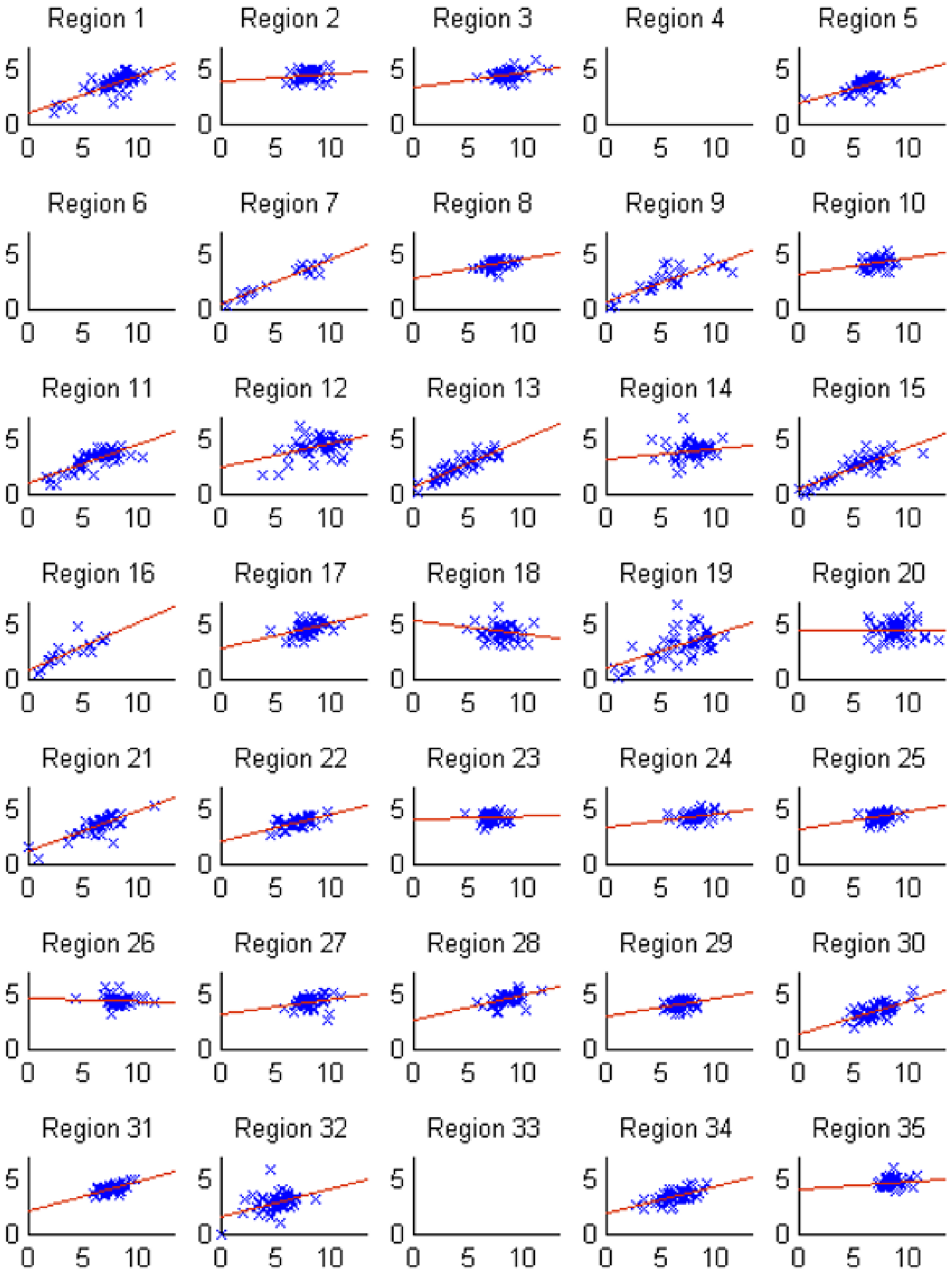

Figure 5.23: MT vs. NOE for all 35 regions of the Desikan-Killiany atlas (left hemisphere only, see Table 5.3 for region names). Each datapoint in the plots represents the averaged MT and NOE of the specific region for each subject. The individual plots are scaled from 0 to 13 on the x-axis (MT) and 0 to 7 on the y-axis (NOE).

Table 5.3: Desikan-Killiany atlas regions

Region 1	bankssts	**Region 19**	parsorbitalis
Region 2	caudalanteriorcingulate	**Region 20**	parstriangularis
Region 3	caudalmiddlefrontal	**Region 21**	pericalcarine
Region 4	corpuscallosum	**Region 22**	postcentral
Region 5	cuneus	**Region 23**	posteriorcingulate
Region 6	entorhinal	**Region 24**	precentral
Region 7	fusiform	**Region 25**	precuneus
Region 8	inferiorparietal	**Region 26**	rostralanteriorcingulate
Region 9	inferiortemporal	**Region 27**	rostralmiddlefrontal
Region 10	isthmuscingulate	**Region 28**	superiorfrontal
Region 11	lateraloccipital	**Region 29**	superiorparietal
Region 12	lateralorbitofrontal	**Region 30**	superiortemporal
Region 13	lingual	**Region 31**	supramarginal
Region 14	medialorbitofrontal	**Region 32**	frontalpole
Region 15	middletemporal	**Region 33**	temporalpole
Region 16	parahippocampal	**Region 34**	transversetemporal
Region 17	paracentral	**Region 35**	insula
Region 18	parsopercularis		

averaging across all regions in the brain (Figure 5.15).

MT has previously been linked to myelination; this result suggests that NOE is also closely related to myelination, which is not surprising since it results from saturation over the fat peak in the myelin proton spectrum[49]. However although NOE is a smaller signal, the sensitivity in the fitted amplitude compares favourably to that for MT (intra-subject standard deviation over repeated visits 0.61% vs 1.55%[11]) since it is less sensitive to B_1. Furthermore it can be quantified at lower saturation powers reducing SAR. This suggested that NOE might provide an alternative marker of myelin at 7T.

Despite the fact that MT and NOE are tightly coupled, the NOE signal shows an offset (non-zero intercept in Figures 5.15 and 5.17). This could be due to a contribution from other tissue compartments including blood which had a relatively higher NOE signal compared to MT (see Figure 5.17). This suggests that blood volume changes may alter the relationship between MT and NOE in some pathology, like Gliomas that show haemorrhage. Previous work has shown that the NOE signal in Bovine Serum Albumin (BSA) is pH dependent and therefore probably exchange relayed[21], although other work did not show pH dependency with NOE[19]. The tight coupling observed *in-vivo* might thus provide a non-invasive and sensitive method of monitor pH which should be investigated in ischaemic regions.

5.7.5 Conclusions

This study shows that the *z-spectrum* NOE signal is tightly coupled to MT in the healthy brain across all age ranges, with similar results in MS lesions. The relationship will likely be affected by blood contributions, and the NOE/MT ratio may also provide a method of monitoring pH *in-vivo*. The strong link between the two separately measured metrics and the offset seen in the NOE signal suggests multiple mechanisms of magnetization transfer, which future studies should probe. If the relationship between MT and NOE can be broken, the magnetization transfer mechanisms can be investigated individually.

5.8 Conclusions

Developing a robust MT, NOE and CEST quantification method (Chapter 4) has enabled the study of how the different metrics behave in the the healthy and diseased brain. Applying the methodology to MS has shown that myelination in lesions can be tracked longitudinally, showing both demyelination and remyelination (partial and full). The aim of the longitudinal MS study was to see if demyelination or remyelination can be predicted from the profile of longitudinal MT or NOE signal, but at the time of writing this thesis no predictions can be made (although processing of the data continues). An important observation from the longitudinal MS study is that MT and NOE show the same demyelination and remyelination results. This apparent coupling of the MT and NOE is what sparked the study of NOE vs. MT in the human brain.

Applying the quantitative methodology in Glioma has shown that the high APT values seen in earlier, not T_1-corrected work, are probably highly T_1-weighted. Figure 5.10 shows how two novel but different quantification techniques lower the apparent hyper-intense APT signal see in GBM. Grading Gliomas based on APT therefore becomes more difficult, if the APT values are low in both low and high grade tumours, but a contrast mechanism that combines APT and T_1 information could still be valuable in diagnosis. The findings also show that both edema and haemorrhage perturb the results in quantitative CEST, but haemorrhage in particular seems to null most MT/CEST effects.

In the healthy brain, having fully quantitative MT data that is corrected for B_1 and T_1 has allowed the construction of cortical myeloarchitecture maps, that strongly relate to electrophysiological connectivity. The findings validate the hypothesis that neural oscillations mediate cortical myeloarchitecture, and paves the way for future investigations of the structure/function relationship and its breakdown in pathology. Additionally, we have shown that with conventional *z-spectrum* acquisition, the measured (and B_1/T_1 corrected) MT and NOE metrics are strongly correlated. This is important in two ways: Firstly the NOE is less sensitive to variations in B_1 and therefore easier to quantify, and could also be linked to myelination. Secondly, if the correlation between MT and NOE can be broken, the origin of both mechanisms can be further understood.

Bibliography

[1] A Alexander-Bloch, J N Giedd, and E Bullmore. Imaging structural covariance between human brain regions. *Nat Rev Neurosci*, 14(5):322–336, 2013.

[2] Christian F Beckmann, Marilena DeLuca, Joseph T Devlin, and Stephen M Smith. Investigations into resting-state connectivity using independent component analysis. *Philosophical Transactions of the Royal Society of London - Series B: Biological Sciences*, 360(1457):1001–1013, 2005.

[3] B Biswal, F Z Yetkin, V M Haughton, and J S Hyde. Functional connectivity in the motor cortex of resting human brain using echo-planar MRI. *Magn Reson Med*, 34(4):537–541, 1995.

[4] J William Brown, Matteo Pardini, Wallace Brownlee, Kryshani Fernando, Rebecca Samson, Claudia Nandini Wheeler-Kingshott, Olga Ciccarelli, David Miller, and Declan Chard. An Abnormal Periventricular Gradient in Magnetisation Transfer Ratio Occurs Early in Multiple Sclerosis (S41.002). *Neurology*, 86(16 Supplement), 2016.

[5] Alastair Compston and Alasdair Coles. Multiple sclerosis, 2008.

[6] Christian Confavreux and Sandra Vukusic. Age at disability milestones in multiple sclerosis. *Brain*, 129(3):595–605, 2006.

[7] G R Davies, D J Tozer, M Cercignani, a Ramani, C M Dalton, a J Thompson, G J Barker, P S Tofts, and D H Miller. Estimation of the macromolecular proton fraction and bound pool T2 in multiple sclerosis. *Multiple sclerosis (Houndmills, Basingstoke, England)*, 10(6):607–13, 2004.

[8] Rahul S. Desikan, Florent Ségonne, Bruce Fischl, Brian T. Quinn, Bradford C. Dickerson, Deborah Blacker, Randy L. Buckner, Anders M. Dale, R. Paul Maguire, Bradley T. Hyman, Marilyn S. Albert, and Ronald J. Killiany. An automated labeling system for subdividing the human cerebral

cortex on MRI scans into gyral based regions of interest. *NeuroImage*, 31 (3):968–980, 2006.

[9] R R Edelman, S S Ahn, D Chien, W Li, A Goldmann, M Mantello, J Kramer, and J Kleefield. Improved time-of-flight MR angiography of the brain with magnetization transfer contrast. *Radiology*, 184(2):395–399, aug 1992.

[10] R Felix, W Schorner, M Laniado, H Niendorf, C Claussen, W Fiegler, and U Speck. Brain Tumors: MR Imaging with Gadolinium-DTPA. *Radiology*, 156(3):681–688, 1985.

[11] Nicolas Geades, Benjamin A E Hunt, Simon M. Shah, Andrew Peters, Olivier E. Mougin, and Penny A. Gowland. Quantitative analysis of the z-spectrum using a numerically simulated look-up table: Application to the healthy human brain at 7T. *Magnetic Resonance in Medicine*, oct 2016.

[12] E M Gibson, D Purger, C W Mount, A K Goldstein, G L Lin, L S Wood, I Inema, S E Miller, G Bieri, J B Zuchero, B A Barres, P J Woo, H Vogel, and M Monje. Neuronal activity promotes oligodendrogenesis and adaptive myelination in the mammalian brain. *Science*, 344(6183):1252304, 2014.

[13] Matthew F Glasser, Timothy S Coalson, Emma C Robinson, Carl D Hacker, John Harwell, Essa Yacoub, Kamil Ugurbil, Jesper Andersson, Christian F Beckmann, Mark Jenkinson, Stephen M Smith, and David C Van Essen. A multi-modal parcellation of human cerebral cortex. *Nature*, 536(7615): 171–178, aug 2016.

[14] Stuart A. Grossman and Julette F. Batara. Current management of glioblastoma multiforme. *Seminars in Oncology*, 31(5):635–644, 2004.

[15] Ileana Hancu, W Thomas Dixon, Mark Woods, Elena Vinogradov, a Dean Sherry, and Robert E Lenkinski. CEST and PARACEST MR contrast agents. *Acta radiologica (Stockholm, Sweden : 1987)*, 51(8):910–23, 2010.

[16] Yong He, Zhang J. Chen, and Alan C. Evans. Small-Word anatomical networks in the human brain revealed by cortical thickness from MRI-based. *Cerebral Cortex*, 17(10):2407–2419, 2007.

[17] Hye Young Heo, Craig K. Jones, Jun Hua, Nirbhay Yadav, Shruti Agarwal, Jinyuan Zhou, Peter C M van Zijl, and Jay J. Pillai. Whole-brain amide proton transfer (APT) and nuclear overhauser enhancement (NOE) imaging in glioma patients using low-power steady-state pulsed chemical exchange saturation transfer (CEST) imaging at 7T. *Journal of Magnetic Resonance Imaging*, 44(1):41–50, 2016.

[18] Benjamin A E Hunt, Prejaas K Tewarie, Olivier E Mougin, Nicolas Geades, Derek K Jones, Krish D Singh, Peter G Morris, Penny A Gowland, and Matthew J Brookes. Relationships between cortical myeloarchitecture and electrophysiological networks. *Proceedings of the National Academy of Sciences of the United States of America*, 113(47):13510–13515, 2016.

[19] Tao Jin, Ping Wang, Xiaopeng Zong, and Seong-Gi Kim. MR imaging of the amide-proton transfer effect and the pH-insensitive nuclear overhauser effect at 9.4 T. *Magnetic Resonance in Medicine*, 69(3):760–770, mar 2013.

[20] Craig K. Jones, Michael J. Schlosser, Peter C M Van Zijl, Martin G. Pomper, Xavier Golay, and Jinyuan Zhou. Amide proton transfer imaging of human brain tumors at 3T. *Magnetic Resonance in Medicine*, 56(3):585–592, 2006.

[21] Craig K. Jones, Alan Huang, Jiadi Xu, Richard A E Edden, Michael Schar, Jun Hua, Nikita Oskolkov, Domenico Zaca, Jinyuan Zhou, Michael T. McMahon, Jay J. Pillai, and Peter C M van Zijl. Nuclear Overhauser enhancement (NOE) imaging in the human brain at 7T. *NeuroImage*, 77: 114–124, 2013.

[22] Vitaliy Khlebnikov, Jeroen C W Siero, Jannie Wijnen, Fredy Visser, Peter R. Luijten, Dennis W J Klomp, and Hans Hoogduin. Is there any difference in Amide and NOE CEST effects between white and gray matter at 7 T? *Journal of Magnetic Resonance*, 272:82–86, 2016.

[23] A. Klistorner, J. Chaganti, R. Garrick, K. Moffat, and C. Yiannikas. Magnetisation transfer ratio in optic neuritis is associated with axonal loss, but not with demyelination. *NeuroImage*, 56(1):21–26, 2011.

[24] Meng Law, Stanley Yang, Hao Wang, James S Babb, Glyn Johnson, Soonmee Cha, Edmond A Knopp, and David Zagzag. Glioma grading: sensitivity, specificity, and predictive values of perfusion MR imaging and proton MR spectroscopic imaging compared with conventional MR imaging. *AJNR American journal of neuroradiology*, 24(10):1989–1998, 2003.

[25] Jason P. Lerch, Keith Worsley, W. Philip Shaw, Deanna K. Greenstein, Rhoshel K. Lenroot, Jay Giedd, and Alan C. Evans. Mapping anatomical correlations across cerebral cortex (MACACC) using cortical thickness from MRI. *NeuroImage*, 31(3):993–1003, 2006.

[26] Ives R. Levesque, Paul S. Giacomini, Sridar Narayanan, Luciana T. Ribeiro, John G. Sled, Doug L. Arnold, and G. Bruce Pike. Quantitative magnetization transfer and myelin water imaging of the evolution of acute multiple sclerosis lesions. *Magnetic Resonance in Medicine*, 63:633–640, 2010.

[27] F. J. Lexa, R. I. Grossman, and A. C. Rosenquist. MR of wallerian degeneration in the feline visual system: Characterization by magnetization transfer rate with histopathologic correlation. *American Journal of Neuroradiology*, 15(2):201–212, 1994.

[28] Dapeng Liu, Jinyuan Zhou, Rong Xue, Zhentao Zuo, Jing An, and Danny J J Wang. Quantitative characterization of nuclear overhauser enhancement and amide proton transfer effects in the human brain at 7 Tesla. *Magnetic Resonance in Medicine*, 70(4):1070–1081, 2013.

[29] Jil Meier, Prejaas Tewarie, Arjan Hillebrand, Linda Douw, Bob W. van Dijk, Steven M. Stufflebeam, and Piet Van Mieghem. A Mapping Between Structural and Functional Brain Networks. *Brain Connectivity*, 31 (0):brain.2015.0408, 2016.

[30] David H Miller, Frederik Barkhof, Joseph A Frank, Geoffrey J M Parker, and Alan J Thompson. Measurement of atrophy in multiple sclerosis: pathological basis, methodological aspects and clinical relevance. *Brain : a journal of neurology*, 125(Pt 8):1676–95, 2002.

[31] O E Mougin, R C Coxon, A Pitiot, and Penny A. Gowland. Magnetization transfer phenomenon in the human brain at 7 T. *NeuroImage*, 49(1):272–81, 2010.

[32] Olivier Mougin, Matthew Clemence, Andrew Peters, Alain Pitiot, and Penny Gowland. High-resolution imaging of magnetisation transfer and nuclear Overhauser effect in the human visual cortex at 7 T. *NMR in Biomedicine*, 26(11):1508–1517, 2013.

[33] George C O'Neill, Eleanor L Barratt, Benjamin a E Hunt, Prejaas K Tewarie, and Matthew J Brookes. Measuring electrophysiological connectivity by power envelope correlation: a technical review on MEG methods. *Physics in Medicine and Biology*, 60(21):R271–R295, 2015.

[34] Quinn T Ostrom, Haley Gittleman, Peter Liao, Chaturia Rouse, Yanwen Chen, Jacqueline Dowling, Yingli Wolinsky, Carol Kruchko, and Jill Barnholtz-Sloan. CBTRUS Statistical Report: Primary Brain and Central Nervous System Tumors Diagnosed in the United States in 2007-2011. *Neuro-oncology*, 16 Suppl 4(suppl_4):iv1–iv63, 2014.

[35] Rachel Scheidegger, Elena Vinogradov, and David C. Alsop. Amide proton transfer imaging with improved robustness to magnetic field inhomogeneity and magnetization transfer asymmetry using saturation with frequency alternating RF irradiation. *Magnetic Resonance in Medicine*, 66(5):1275–1285, 2011.

[36] Klaus Schmierer, Francesco Scaravilli, Daniel R. Altmann, Gareth J. Barker, and David H. Miller. Magnetization transfer ratio and myelin in postmortem multiple sclerosis brain. *Annals of Neurology*, 56(3):407–415, 2004.

[37] Marieke L. Scholvinck, David A. Leopold, Matthew J. Brookes, and Patrick H. Khader. The contribution of electrophysiology to functional connectivity mapping. *NeuroImage*, 80:297–306, 2013.

[38] JN Scott, PMA Brasher, RJ Sevick, NB Rewcastle, and PA Forsyth. How often are nonenhancing supratentorial gliomas malignant? A population study. *Neurology*, 59(6):947–949, 2002.

[39] A Dean Sherry and Mark Woods. Chemical Exchange Saturation Transfer Contrast Agents for Magnetic Resonance Imaging. *Annual Review of Biomedical Engineering*, 10(1):391–411, 2008.

[40] Phillip Zhe Sun, Jinyuan Zhou, Weiyun Sun, Judy Huang, and Peter C M van Zijl. Detection of the ischemic penumbra using pH-weighted MRI. *Journal of cerebral blood flow and metabolism : official journal of the International Society of Cerebral Blood Flow and Metabolism*, 27(6):1129–1136, 2007.

[41] Enzo Terreno, Daniela Delli Castelli, and Silvio Aime. Encoding the frequency dependence in MRI contrast media: The emerging class of CEST agents, 2010.

[42] P. Tewarie, M. G. Bright, A. Hillebrand, S. E. Robson, L. E. Gascoyne, P. G. Morris, J. Meier, P. Van Mieghem, and M. J. Brookes. Predicting haemodynamic networks using electrophysiology: The role of non-linear and cross-frequency interactions. *NeuroImage*, 130:273–292, 2016.

[43] The University of Nottingham. NeuRoi image analysis software. https://www.nottingham.ac.uk/research/groups/clinicalneurology/neuroi.aspx Accessed 16/02/2016, 2016.

[44] Osamu Togao, Takashi Yoshiura, Jochen Keupp, Akio Hiwatashi, Koji Yamashita, Kazufumi Kikuchi, Yuriko Suzuki, Satoshi O. Suzuki, Toru Iwaki, Nobuhiro Hata, Masahiro Mizoguchi, Koji Yoshimoto, Koji Sagiyama, Masaya Takahashi, and Hiroshi Honda. Amide proton transfer imaging of

adult diffuse gliomas: Correlation with histopathological grades. *Neuro-Oncology*, 16(3):441–448, 2014.

[45] Peter C M Van Zijl, Jinyuan Zhou, Noriko Mori, Jean Francois Payen, David Wilson, and Susumu Mori. Mechanism of magnetization transfer during on-resonance water saturation. A new approach to detect mobile proteins, peptides, and lipids. *Magnetic Resonance in Medicine*, 49(3):440–449, 2003.

[46] K M Ward, A H Aletras, and R S Balaban. A new class of contrast agents for MRI based on proton chemical exchange dependent saturation transfer (CEST). *Journal of magnetic resonance (San Diego, Calif. : 1997)*, 143(1): 79–87, 2000.

[47] Zhibo Wen, Shuguang Hu, Fanheng Huang, Xianlong Wang, Linglang Guo, Xianyue Quan, Silun Wang, and Jinyuan Zhou. MR imaging of high-grade brain tumors using endogenous protein and peptide-based contrast. *NeuroImage*, 51(2):616–622, 2010.

[48] Leonard E. White, Timothy J. Andrews, Christine Hulette, Ann Richards, Marybeth Groelle, Joseph Paydarfar, and Dale Purves. Structure of the human sensorimotor system. II: Lateral symmetry. *Cerebral Cortex*, 7(1): 31–47, 1997.

[49] M. J. Wilhelm, H. H. Ong, S. L. Wehrli, C. Li, P.-H. Tsai, D. B. Hackney, and F. W. Wehrli. Direct magnetic resonance detection of myelin and prospects for quantitative imaging of myelin density. *Proceedings of the National Academy of Sciences*, 109(15):9605–9610, 2012.

[50] Moritz Zaiss, Junzhong Xu, Steffen Goerke, Imad S. Khan, Robert J. Singer, John C. Gore, Daniel F. Gochberg, and Peter Bachert. Inverse Z-spectrum analysis for spillover-, MT-, and T1-corrected steady-state pulsed CEST-MRI - application to pH-weighted MRI of acute stroke. *NMR in Biomedicine*, 27(3):240–252, 2014.

[51] Moritz Zaiss, Johannes Windschuh, Daniel Paech, Jan-Eric Meissner, Sina Burth, Benjamin Schmitt, Philip Kickingereder, Benedikt Wiestler, Wolfgang Wick, Martin Bendszus, Heinz-Peter Schlemmer, Mark E Ladd, Peter Bachert, and Alexander Radbruch. Relaxation-compensated CEST-MRI of the human brain at 7T: Unbiased insight into NOE and amide signal changes in human glioblastoma. *NeuroImage*, 112:180–188, may 2015.

[52] Moritz Zaiss, Johannes Windschuh, Steffen Goerke, Daniel Paech, Jan-Eric Meissner, Sina Burth, Philipp Kickingereder, Wolfgang Wick, Martin Bendszus, Heinz-Peter Schlemmer, Mark E Ladd, Peter Bachert, and Alexander Radbruch. Downfield-NOE-suppressed amide-CEST-MRI at 7 Tesla provides a unique contrast in human glioblastoma. *Magnetic resonance in medicine*, jan 2016.

[53] J Zhou and P Zijl. Chemical exchange saturation transfer imaging and spectroscopy. *Progress in Nuclear Magnetic Resonance Spectroscopy*, 48(2): 109–136, 2006.

[54] J Zhou, E Tryggestad, Z Wen, B Lal, T Zhou, R Grossman, S Wang, K Yan, D X Fu, E Ford, B Tyler, J Blakeley, J Laterra, and P C van Zijl. Differentiation between glioma and radiation necrosis using molecular magnetic resonance imaging of endogenous proteins and peptides. *Nature Medicine*, 17(1):130–134, 2011.

[55] Jinyuan Zhou, Jean-Francois Payen, David A Wilson, Richard J Traystman, and Peter C M van Zijl. Using the amide proton signals of intracellular proteins and peptides to detect pH effects in MRI. *Nature medicine*, 9(8): 1085–90, aug 2003.

[56] Jinyuan Zhou, Jaishri O Blakeley, Jun Hua, Mina Kim, John Laterra, Martin G Pomper, and Peter C M van Zijl. Practical data acquisition method for human brain tumor amide proton transfer (APT) imaging. *Magnetic resonance in medicine : official journal of the Society of Magnetic Resonance in Medicine / Society of Magnetic Resonance in Medicine*, 60:842–849, 2008.

[57] Jinyuan Zhou, He Zhu, Michael Lim, Lindsay Blair, Alfredo Quinones-Hinojosa, Steven A. Messina, Charles G. Eberhart, Martin G. Pomper, John Laterra, Peter B. Barker, Peter C M Van Zijl, and Jaishri O. Blakeley. Three-dimensional amide proton transfer MR imaging of gliomas: Initial experience and comparison with gadolinium enhancement. *Journal of Magnetic Resonance Imaging*, 38(5):1119–1128, 2013.

Conclusion

This thesis presents a new methodology for quantifying MT and CEST proton pool concentrations *in vivo* at 7T, and uses the quantitative information to study macromolecules in healthy and diseased brain. The complex theory of z-spectroscopy is discussed in Chapter 2 and various methods of quantifying effects seen in z-spectroscopy are also introduced. The benefits and limitations of current quantification methods are discussed and the new methodology is proposed, considering also the advantages and drawbacks of ultra-high field (7T).

The MT signal observed in z-spectroscopy is strongly linked to myelin content, but the source of the signal and how to probe and quantify it is under debate. Chapter 3 of this thesis aims to investigate more characteristics of the MT signal, like the lineshape of the effect seen in z-spectroscopy and the spatial, spectral and relaxation characteristics of macromolecular signal in spectroscopic imaging. In z-spectroscopy, the T_2 of the lineshape is seen to vary in the human brain, depending on nerve fibre orientation, but also shows strong sensitivity to B_1 saturation power. In spectroscopic imaging, the macromolecular signal is shown to relax at different rates between white matter and gray matter, but no spatial variation in macromolecular concentration was shown.

Chapter 4 presents the newly developed quantitative MT and CEST method, together with a Monte-Carlo analysis and a repeatability study to validate the robustness and sensitivity of the method. This method is tested in the healthy and diseased brain in various applications described in Chapter 5. Firstly, the new method is used to study the myelin content of Multiple Sclerosis (MS) lesions in a longitudinal study, showing that in cases where lesion recovery is full, myelination returns to normal levels too. This study also showed that the NOE signal seems to mirror the MT signal, but is even more consistent due to the less sensitivity to B_1 saturation power, making it a potentially more powerful myelination metric than MT. The quantification method is also used to study the APT signal in Glioma, and when possible compared to existing APT quantification techniques. This study has proven that APT quantification relies on separating APT from all other effects seen on the z-spectrum, including MT, NOE, other CEST effects, as well as B_1 and T_1, although there is still a lack of a gold standard or ground truth for APT quantification in the human brain. Because of this, investigating on the accuracy of the methodology is impossible, but the precision or repeatability has been demonstrated.

Finally the new method is used to quantify MT and NOE in a large group of healthy volunteers, and the myelination accross the brain is shown to strongly correlate to funcional connectivity, proving a vital relationship between function and structure. The strong correlation was seen between MT and MEG-derived functional connectivity, but the relationship with NOE was not investigated. The final section in Chapter 5 investigates the relationship between MT, NOE and T_1 in the healthy brain, also showing strong correlation between MT and NOE, but not T_1. This proves the methodology is successful in removing both B_1 and T_1 effects from quantitative MT and NOE measures. The results of the work presented in this thesis have sparked interest in CEST experiments in the blood, further investigation of the NOE effect and the relationship between MT and age, which are currently, at the time of writing this thesis, being investigated.

In conclusion, this thesis presents a new methodology for quantification of MT and CEST effects, aiming to investigate its robustness with a number of applications in the healthy and diseased human brain. We have shown good repeatability of quantitative results in the healthy brain, and a relationship between MT and

NOE that is strong in both healthy and diseased brain. The methodology has also been successful in providing a measurable and quantifiable difference of MT in pathology.